Understanding Flow Structure in a Groyne Field

Themba Rutherford Ziqubu

Engineering

University of KwaZulu-Natal

A thesis submitted in fulfilment of the requirements for the degree of

Master of Science

January 11, 2018

Supervisor: Prof D.D. Stretch

As the candidate's Supervisor I agree/do not agree to the submission of this thesis.

---------- ----------

Prof. Derek Stretch Date

DECLARATION

I, Themba Rutherford Ziqubu declare that

1. The research reported in this thesis, except where otherwise indicated, is my original research.

2. This thesis has not been submitted for any degree or examination at any other university.

3. This thesis does not contain other persons' data, pictures, graphs or other information, unless specifically acknowledged as being sourced from other persons.

4. This thesis does not contain other persons' writing, unless specifically acknowledged as being sourced from other researchers. Where other written sources have been quoted, then:
   a) Their words have been re-written but the general information attributed to them has been referenced
   b) Where their exact words have been used, then their writing has been placed in italics and inside quotation marks, and referenced.

5. This thesis does not contain text, graphics or tables copied and pasted from the Internet, unless specifically acknowledged, and the source being detailed in the thesis and in the References sections.

Signed

Acknowledgements

I would like to express my greatest gratitude to the following

My family for the support and love during the period of this study

My amazing partner Phumzile for her never ending belief in me and encouragement

Vulindlela Zikhali for his vast contribution, I really appreciate your friendship and your help

Most importantly Prof Stretch for never losing faith in me and always making me feel welcome, I truly value your mentorship and guidance. Ngiyabonga kakhulu.

ABSTRACT

Groyne structures are widely used all over the world for the purposes of controlling longshore currents and slowing down the rate of sediment transport along coast lines. The limited previous studies in this area have led to unfit designs and installations of these structures. The history of the Durban coastline highlights challenges concerning the use of these structures that engineers have been faced with. The groynes along the Durban coast are not sufficient to stabilize the coastline and they are used in conjunction with a sand nourishment scheme.

This research aims to elucidate the flow field characteristics and patterns around groynes in a groyne field. A parametric study of three impermeable groynes in a groyne field was developed using numerical modelling software. The DHI MIKE 21 Spectral Wave and Hydrodynamic models were used for the study. Various wave and groyne field parameters were varied systematically. The main focus of the study was on the groyne tips as this is an area most prone to scour failure, especially with impermeable groynes. The simulations reveal how the flow patterns within the groyne compartments change with variation in wave parameters. It was found that under certain wave conditions, recirculation patterns develop within the groyne compartments. Storm conditions can have devastating effects on coastlines. Therefore, this study also aimed to understand how these conditions may affect the functioning of a groyne field.

Table of Contents

1. INTRODUCTION 1
   1.1 Motivation 1
   1.2 Study background 2
   1.3 Durban coastline climate 5
   1.4 Research question 7
   1.5 Aim 7
   1.6 Objectives 7
   1.7 Dissertation Outline 8
2. LITERATURE REVIEW 9
   2.1 Introduction 9
   2.2 Types of groynes 9
      2.2.1 Permeable groyne 9
      2.2.2 Impermeable groyne 10
   2.3 Coastal processes 11
      2.3.1 Wave induced current 11
      2.3.2 Coastal erosion 14
      2.3.3 Longshore sediment transport 16
   2.4 Hydrodynamic and morphodynamic driving forces 16
      2.4.1 Breaking waves 16
      2.4.2 Radiation stress 18
   2.5 Residence time 20
   2.6 Previous research on flow patterns and sediment transport within a groyne or groyne field 21
   2.7 Summary 27
3. METHODOLOGY 29
   3.1 Numerical modelling 29
      3.1.1 Introduction 29
      3.1.2 Overview 29
      3.1.3 Mike Mesh Generator 29
      3.1.4 Spectral Wave Model 30
      3.1.5 Hydrodynamic Flow Model 30
   3.2 Durban Beach Profile 30
   3.3 Breaker zone 31

3.4 Simulation Methodology 31
3.4.1 Simulation overview 31
3.4.2 Significant wave heights 32
3.4.3 Mean Water level 32
3.4.4 Incident wave angle 32
3.4.5 Groyne interspacing 32
3.4.6 Storm condition 32
3.5 Model configuration 32
3.5.1 Flexible mesh model parameters 33
3.5.2 Spectral wave model parameters 35
3.5.3 Hydrodynamic model parameters 36
3.5.4 Model discussion 36
3.6 Numerical model compared to field data 37
3.7 Dimensional Analysis 38
3.8 Residence time computation 39
4. RESULTS AND DISCUSSION 40
Outline 40
4.1 Numerical model compared to field data 41
4.2 Peak gradient of radiation stress 45
4.2.1 Significant wave height variation 45
4.2.2 Mean water level variation 46
4.2.3 Incident wave angle variation 47
4.3 Eddy circulation around multiple groynes 48
4.3.1 Significant wave height variation 48
4.3.2 Mean water level variation (MWL) 52
4.3.3 Incident wave angle variation 58
4.3.4 Groyne inter-spacing variations 60
4.4 Storm event 63
4.4.1 Groyne spacing to groyne length during storm event 63
4.4.2 Critical storm event 66
4.5 Synthesis through dimensional Analysis 70
4.6 Water quality implications 79
5. SUMMARY, CONCLUSION AND RECOMMENDATIONS 82
5.1 Summary 82

5.2 Research questions 89
5.3 Recommendations 91
Bibliography 93

LIST OF FIGURES

Figure 1-1: Map overview of the study location in South Africa Durban reproduced from (Olij, 2015) 2
Figure 1-2: Types of groyne systems implemented over the years at Durban beach front in trying to solve coastal erosion (Barnett, 2011) 4
Figure 1-3: Durban beach profile surveyed in July 1995 showing the beach profile on the harbour entrance and along the groyne field. (Schooness, 2000) 5
Figure 1-4: Wave rose for Durban and Richards Bay wave data showing various significant wave heights, wave direction and percentage distribution adapted from (Corbella & Stretch, 2014). 7
Figure 2-1: Resulting longshore current and sediment transport within permeable groyne field adapted from (Trampenau, *et al*., 2004). The presence of permeable groynes reduces the velocity profile as the current passes through the groynes. The sediment is thus retained while the breaker zone moves further offshore therefore limiting coastline erosion. 10
Figure 2-2: Effect of impermeable groyne field on a stretch of coastline. A saw tooth phenomenon whereby the shoreline extend/retreat occurs as a result of accretion upstream and erosion downstream of impermeable groyne field. (Dean & Dalrymple, 2004) 11
Figure 2-3: Impermeable groyne diverts all the longshore current seaward, which may result in rip current formation on the sides of the groyne. Rip current is responsible for sediment lost out at sea (Muir Wood & Fleming, 1981) 12
Figure 2-4: Longshore current velocity in the near-shore zone responsible for sediment movement. The longshore current velocity typically peaks at a breaker line (a region where majority of the waves break) and reduce as the waves dissipate energy toward the shore line. (Reeve, *et al*., 2004) 13
Figure 2-5: The effect of cross shore structures such as a single groyne or groyne field on net longshore transport. Accretion on the up drift side and erosion on the down drift side of a groyne can be expected, particularly with impermeable groynes (Tarnowska, *et al*., 1992). 14
Figure 2-6: Pringle (2015) observed and modelled data for Durban beach profile in the period 1993-2009. The two trends represents significant wave height (top graph) and shore line position (bottom graph). The shoreline position graph consists of observed shoreline position (dash line) and the modelled shoreline position (solid line). (Pringle, 2015). 15
Figure 2-7: Profile showing sinusoidal wave progression and still water level (Reeve, *et al*., 2004) .. 19
Figure 2-8: The momentum flux in a progressive wave (Longuet-Higgins & Stewart, 1964) 20
Figure 2-9: Flow patterns observed by Trampenau, *et al*. for high level and low flow constriction in an impermeable groyne field (adapted from Trampenau, *et al*. 2004) 22

Figure 2-10: Gravity current development in a groyne field with relative low groyne spacing to groyne length ratio, water is bounded between groyne 1 (G1) and groyne 2 (G2) resulting in formation of a gravity current (Trampenau, *et al*., 2004). 23
Figure 2-11: Bay of Plenty semi permeable groyne showing scour at the groyne tip during March 2012. (EMS, 2016)..... 25
Figure 2-12: Average current roses for 19 current meters deployed in the vicinity of Bay of Plenty and wave rose (top right). The zoomed in image show a cross shore dominant current direction as detected by the current meters. It is noted that wave rose and current rose are dissimilar in showing direction. Wave rose depict wave direction from an angle where the waves propagate from, while current rose show current direction to the angle of propagation (adapted from Lucca, 2013) 26
Figure 3-1: Durban beach profile plotted from bathymetry data adapted from (Lucca, 2013) Figure 1.4. 30
Figure 3-2: Breaker width/breaker zone measurement from a spectral wave model 31
Figure 3-3: Durban beach groyne layout bathymetry showing the position of the groynes according to site layout for the purpose of the study. 34
Figure 4-1: Modelled current speed vector plot for Water level = 1.5 m. The results reveal how alongshore current is resisted by the groynes, and as a result rip current and eddy circulation develop between the groynes. The Bay of Plenty groyne (magnified image) experienced the greatest peak rip current toward the mid span high tide and wave conditions. (Model run A2)..... 42
Figure 4-2: Modelled current speed vector plot for Water level = 0.9 m. The results reveal how alongshore current is resisted by the groynes, and as a result rip current and eddy circulation develop between the groynes. The Bay of Plenty groyne (magnified image) experienced the greatest peak rip current toward the midspan high tide and wave conditions. (Model run A1)..... 43
Figure 4-3 (a) (left): Predicted current vector plot and eddy circulation for wave condition (Hs = 1 m; Tp = 14 s; θ = $45^0/135^0$; *MWL* = 0), G_L/B_Z = 2.22 and G_S = 300 m (Model run D9), (b) (centre): Predicted current vector plot and eddy circulation for wave condition (Hs = 2 m; Tp = 14 s; θ = $45^0/135^0$; *MWL* = 0), G_L/B_Z = 1.33 and G_S = 300 m (Model run D12) and (c) (right): Predicted current vector plot and eddy circulation for wave condition (Hs = 3 m; Tp = 14 s; θ = $45^0/135^0$; *MWL* = 0), G_L/B_Z = 0.91 and G_S = 300 m (Model run D14)..... 51
Figure 4-4 (a) (left): Predicted current vector plot and eddy circulation for (Hs = 1 m; Tp = 14 s; θ = $45^0/135^0$; *MWL* = -1), G_L/B_Z = 1.67 and G_S = 300 m (Model run D10), (b) (centre): Predicted current vector plot and eddy circulation for (Hs = 1 m; Tp = 14 s; θ = $45^0/135^0$; MWL= 0), G_L/B_Z = 2.22 and G_S = 300 m (Model run D9) and (c) (right): Predicted current vector plot and eddy circulation for (Hs = 1 m; Tp = 14 s; θ = $45^0/135^0$; MWL = 1), G_L/B_Z = 2.94 and G_S = 300 m (Model run D8)..... 54
Figure 4-5 (a) (left): Predicted current vector plot and eddy circulation for wave condition (Hs = 2m; Tp = 14s; θ = $45^0/135^0$; *MWL* = -1), G_L/B_Z = 0.94 and G_S = 300 m (Model run D10), (b) (centre):

Predicted current vector plot and eddy circulation for wave condition (Hs = 2m; Tp = 14s; θ = $45^0/135^0$; MWL = 0), G_L /B_Z = 1.33 and G_S = 300 m (Model run D12) and (c) (right): Predicted current vector plot and eddy circulation for wave condition (Hs = 2m; Tp = 14s; θ = $45^0/135^0$; MWL = 1), G_L /B_Z = 1.67 and G_S = 300 m (Model run D11) 57

Figure 4-6 (a) (left): Predicted current vector plot and eddy circulation for wave condition (Hs = 1 m; Tp = 14 s; θ = $150^0/30^0$; MWL = 0), G_L /B_Z = 2.67 and G_S = 300 m (Model run D16), (b) (centre): Predicted current vector plot and eddy circulation for wave condition (Hs = 1 m; Tp = 14 s; θ = $135^0/45^0$; MWL = 0), G_L /B_Z = 2.22 and G_S = 300 m (Model run D9) and (c) (right): Predicted current vector plot and eddy circulation for wave condition (Hs = 1 m; Tp = 14 s; θ = $120^0/60^0$; MWL = 0), G_L /B_Z = 2 and G_S = 300 m (Model run D2) 59

Figure 4-7 (a) (left): Predicted current vector plot and eddy circulation for wave condition (Hs = 1m; Tp = 14s; θ = $120^0/60^0$; MWL = 0), G_L /B_Z = 2 and G_S/G_L = 1 (Model run B2), (b) (centre): Predicted current vector plot and eddy circulation for wave condition (Hs = 1m; Tp = 14s; θ = $120^0/60^0$; MWL = 0), G_L /B_Z = 2.22 and G_S/G_L = 1.75 (Model run E2) and (c) (right): Predicted current vector plot and eddy circulation for wave condition (Hs = 1m; Tp = 14s; θ = $120^0/60^0$; MWL = -1), G_L /B_Z = 1.500 and G_S/G_L = 3 (Model run G3). 62

Figure 4-8 (a) (left): Predicted current vector plot and eddy circulation for (Hs = 3.5 m; Tp = 14 s; θ = $120^0/60^0$; MWL = 0), G_L /B_Z = 0.667 and G_S/G_L = 1.25 (Model run Cs12), (b) (centre): Predicted current vector plot and eddy circulation for (Hs = 3.5 m; Tp = 14 s; θ = $120^0/60^0$; MWL = 0), G_L /B_Z = 0.667 and G_S/G_L = 2.00 (Model run Fs22) and (c) (right): Predicted current vector plot and eddy circulation for (Hs = 3.5 m; Tp = 14 s; θ = $120^0/60^0$; MWL = 0), G_L /B_Z = 0.667 and G_S/G_L = 3.00 (Model run Is8) 65

Figure 4-9 (a) (left): Predicted current vector plot and eddy circulation for (Hs = 3.5 m; Tp = 14 s; θ = $135^0/45^0$; MWL = 0), G_L /B_Z = 0.667 and G_S /G_L = 2.00 (Model run Fs25), (b) (centre): Predicted current vector plot and eddy circulation for (Hs = 3.5 m; Tp = 14 s; θ = $135^0/45^0$; MWL = 1), G_L /B_Z = 0.833 and G_S /G_L = 1.60 (Model run Fs24) and (c) (right): Predicted current vector plot and eddy circulation for (Hs = 3.5 m; Tp = 14 s; θ = $135^0/45^0$; MWL = -1), G_L /B_Z = 0.500 and G_S /G_L = 2.67 (Model run Fs26) 68

Figure 4-10 (a) (left): Predicted current speed plot for (Hs = 3.5 m; Tp = 14 s; θ = $120^0/60^0$; MWL = 0), G_L /B_Z = 0.667 and G_S /G_L = 2.00 (Model run Fs25), (b) (centre): Predicted current vector plot for (Hs = 3.5 m; Tp = 14 s; θ = $120^0/60^0$; MWL = 1), G_L /B_Z = 0.833 and G_S /G_L = 1.60 (Model run Fs24) and (c) (right): Predicted current vector plot for (Hs = 3.5 m; Tp = 14 s; θ = $120^0/60^0$; MWL = -1), G_L /B_Z = 0.500 and G_S /G_L = 2.67 (Model run Fs26) 69

Figure 4-11: is a synthesis of the results showing how the flow constriction (G_L/B_Z) affects groyne tip velocity ($|Vtip|/(H_S/T_P)$) for groyne 1. The G_S/G_L values are shown in the figure. 71

Figure 4-12: is a synthesis of the results showing how the flow constriction (G_L/B_Z) affects groyne tip velocity ($|Vtip|/(H_S/T_P)$) for groyne 2. The G_S/G_L values are shown in the figure. 72
Figure 4-13: is a synthesis of the results showing how the flow constriction (G_L/B_Z) affects groyne tip velocity ($|Vtip|/(H_S/T_P)$) for groyne 3. The G_S/G_L values are shown in the figure. 73
Figure 4-14: Flow constriction effect (G_L/B_Z) on the groyne tip velocity angle (β) for upstream groyne 1 74
Figure 4-15: Flow constriction effect (G_L/B_Z) on the groyne tip velocity angle (β) for central groyne 2 75
Figure 4-16: Flow constriction effect (G_L/B_Z) on the groyne tip velocity angle (β) for downstream groyne 3 75
Figure 4-17: Groyne tip velocity components for wave condition Hs = 1 m; Tp = 14 s; θ = $45^0/135^0$; MWL = -1 m; G_L = 150m; B_Z = 90 m; G_L/B_Z = 1.667. The velocity was measured at the groyne tips. 76
Figure 4-18: Graph showing alongshore velocity components for wave condition Hs = 2 m; Tp = 14 s; θ = $45^0/135^0$; MWL = -1; G_L = 150m; B_Z = 160 m; G_L/B_Z = 0.938. Groyne C is the upstream groyne, B central groyne and A downstream groyne. 77
Figure 4-19: Groyne tip u and v velocity components for wave condition (Hs = 3.5 m; Tp = 14 s; θ = $135^0/45^0$; G_L = 150m; MWL = -1 m; G_L/B_Z = 0.5). Groyne A is the upstream groyne, B central groyne and C downstream groyne. 78
Figure 5-1: Schematic flow pattern structure 1 for an impermeable groyne field. The wave direction is depicted on the figure. For simplicity, the red dotted line indicates the breaker line where majority of the waves would break. The groynes in the field experienced rip current on both sides due to the diversion of the alongshore current seaward and the eddy circulation formation on the leeward side. Peak rip current was typically observed to occur on the upstream of the first groyne in the field and the downstream groynes experienced lower velocity. Eddy circulation zones were observed to develop between the groynes. 83
Figure 5-2: Schematic flow pattern structure 2 for an impermeable groyne field. The wave direction is depicted on the figure. For simplicity, the red dotted line indicates the breaker line where majority of the waves would break. Bigger and more circular eddies were observed to form on the leeward side of all the groynes. However, the first groyne (groyne C) in the field typically experienced the biggest eddy circulation compared to the rest of the groynes. 85
Figure 5-3: Schematic flow pattern structure 3 in an impermeable groyne field. The wave direction is depicted on the figure. For simplicity, the red dotted line indicates the breaker line where majority of the waves would break. Bigger and more circular eddies were observed to form on the leeward side of all the groynes. However, the first groyne on the field typically experienced the biggest eddy circulation compared to the rest of the groynes. 86

Figure 5-4: beach contours and scouring bathymetry for Durban groynes adapted from Lucca (2013) Figure 1.4. The bathymetry was developed on MIKE 21 Mesh generator. The highlighted area show Bay of Plenty groyne tip where scouring appear to be worse compared to the other groynes upstream. 87

Figure 5-5: Flow constriction effect (G_L/B_Z) on the groyne tip velocity angle (β) for groynes in a field. Upstream groyne 1 (solid circle), central groyne 2 (cross) and downstream groyne 3 (triangle)..... 88

Figure 5-6: Flow constriction effect (G_L/B_Z) on the groyne tip velocity angle (β) for groynes in a field. Upstream groyne 1 (solid circle), central groyne 2 (cross) and downstream groyne 3 (triangle)..... 89

LIST OF TABLES

Table 1-1: Average Durban wave climate (Corbella & Stretch, 2012b) 6
Table 3-1: A summary of beach and groyne standard features 33
Table 4-1: The effect of varying surface water levels on the breaker width, flow constriction and the current speed for wave condition $Hs = 1.4\ m;\ Tp = 9.05\ s;\ \theta = 116^0;\ G_S = 300\ m$ 41
Table 4-2: The effect of significant wave height variation on breaker zone width for wave condition $Hs = 1\ m;\ Tp = 14\ s;\ \theta = 45^0$; MWL = 0; G_S = 300m. 45
Table 4-3: The effect of water level variation on radiation stress components for wave condition Hs = 1 m; Tp = 14 s; θ = $45^0/135^0$; G_S = 300m 46
Table 4-4: The effect of water level variation on radiation stress components for wave condition Hs = 2 m; Tp = 14 s; θ = $45^0/135^0$ 47
Table 4-5: The effect of incident wave angle variation on radiation stress components for wave condition Hs = 1 m; Tp = 14 s; MWL = 0 m. 47
Table 4-6: The effect of incident wave angle variation on radiation stress components for wave condition Hs = 2 m; Tp = 14 s; MWL = 0 m. 48
Table 4-7: Effects of varying significant wave height on the flow constriction and groyne tip velocity for wave condition Tp = 14 s; θ = $45^0/135^0$; MWL = 0 m; G_S/G_L = 1.5 49
Table 4-8: Effects of varying water level on the geometric parameters and flow constriction for wave condition Hs = 1 m; Tp = 14 s; θ = $45^0/135^0$; G_S= 300 m. 52
Table 4-9: Effect of varying mean water level on the geometric parameters and the flow constriction for wave condition Hs = 2 m; Tp = 14 s; θ = $45^0/135^0$; G_S = 300 m. 55
Table 4-10: The effect of varying incident wave angle on the flow constriction, the groyne tip velocity and direction for wave condition Hs = 1 m; Tp = 14 s; MWL = 0 m; G_S = 300 m. 58
Table 4-11: The effect of varying G_S/G_L ratio on the flow characteristics for wave condition Hs = 1 m; TP = 14 s; θ = $120^0/60^0$; MWL = 0 m. 60
Table 4-12: The effect of groyne spacing to groyne length ratio on the groyne tip velocity magnitude and direction for wave condition Hs = 3.5 m; Tp = 14 s; θ = $120^0/60^0$; MWL = 0 m. 63
Table 4-13: The effect of varying groyne length in contact with active water zone on the flow constriction, groyne tip velocity magnitude and direction for wave condition (Hs = 3.5 m; Tp = 14 s; θ = $135^0/45^0$) 66
Table 4-14: The summary of wave parameters, tip velocity and scaled velocity for single impermeable groyne. The results were adapted from Lucca (2013, Ch. 6.7 pp 99 - 102). 70
Table 4-15: The effect of varying wave conditions on the P-flux and residence time in a groyne field for constant G_S/G_L = 1.5. 79

Table 4-16: The effect of varying G_S /G_L ratio on the P-flux and residence time in a groyne field for constant G_L/B_Z = 2 80
Table 4-17: The effect of storm events on the P-flux and residence time in a groyne field 80
Table 5-1: Durban wave rose data summary for H_S and associated G_L/B_Z 83

LIST OF SYSMBOLS

a	=	Amplitude
D	=	Time mean dissipated power per unit area
η	=	Deviation from mean water level to any point x
H	=	Wave height
$h, h(x)$	=	Water depth
x	=	Distance measured along the horizontal axis
L	=	Wave length
t	=	Time
T, T_P	=	Wave period
T_0	=	Deep water wave period
T_r	=	Residence time
S_{xx}	=	Net force in the direction of propagation
S_{yy}	=	Net force at right angle to the direction of propagation
S_{xy}	=	Shear radiation stress component
u	=	Horizontal component of velocity in the x direction
v	=	Horizontal component of velocity in the y direction
|Vtip|	=	Resultant velocity magnitude for groyne tip u and v velocity components
p	=	Stress or pressure
ρ	=	Density
g	=	Gravity
z	=	Distance on the z axis
H_0, H_0'	=	Deep water wave height
H_b	=	Wave height at breaking
L_b	=	Wave length at breaking
L_0	=	Deepwater wavelength
K_s	=	Shoaling coefficient
K_r	=	Refraction coefficient
C_{g0}	=	Deep water group celerity
C_g	=	Group celerity
c	=	Wave celerity
c_0	=	Deepwater wave celerity
c_f	=	Friction coefficient
θ	=	Incident wave angle
γ	=	Breaker index

ρ	=	density
d_b	=	Depth at breaking
ξ_b, C	=	Surf parameter or Irribaren index
α	=	Beach slope
G_L	=	Groyne length
B_Z	=	Breaker width
Q_0	=	Inflow rate
G_s	=	Groyne spacing
P_x	=	X component of the time mean energy flux per unit length
E	=	Mean wave energy
H_m	=	Maximum breaker height
H_S	=	Significant wave height
k	=	Wave number
H_{rms}	=	Root mean square wave height
u_m	=	Wave orbital velocity
$\tau_{b,y}$	=	Bed shear stress
f_w	=	Wave friction factor
k_N	=	Nikuradse roughness parameter
$V_{\Delta h}$	=	Gravity current
V_{vol}	=	Water volume
$V(x)$	=	Depth average longshore current velocity
β	=	Groyne tip velocity direction
P-flux	=	Flux density in the x-direction
F_Y	=	Driving force

1. INTRODUCTION

Summary: This Chapter introduces the Durban coastal area by giving a brief background of coastal protection, motivation of the study, aims and objectives

---

1.1 Motivation

Durban beaches have suffered from negative impacts caused by human interference with the natural littoral processes. This problem has persisted since the early 1840's when operation of the Durban harbor started. The Durban's shores experience about 500 000 m^3/year of alongshore sediment transport in the littoral zone (Schooness, 2000).

Numerous developments around the harbor and the construction of breakwaters exacerbated the situation, resulting in increased erosion along the beaches. Numerous attempts to stabilize the coastline were implemented including the construction of different types of groynes. Some of these solutions displayed a degree of success while others failed completely (Barnett, 1999). Over time the groyne system developed from impermeable groynes to low level semi-permeable groyne field. Low level groynes alone are not enough to trap the sediments and maintain beaches downstream, therefore nourishments of the beaches with a sand-pumping scheme was necessary to diminish the effects of erosion. Although the groyne field is currently more stable than it was in the past, structural deterioration due to local scouring still persists. Scouring is one of the most critical structural problems and can lead to structural failure of any coastal structure exposed to it.

The three Durban groynes have experienced severe scouring especially around the tips, resulting in structural failure on one of the groynes (Lucca, 2013). In particular, storm conditions have aggravated the scouring problem causing deep holes around the groyne tips. This is a cause for concern as the structural integrity of the groynes may be compromised. There are limited studies that have been conducted on the rip current that develops adjacent to a groyne or groynes (Pattiaratchi, *et al*., 2009). There exist information gap on the understanding the flow patterns and currents that may develop within a groyne field or adjacent to a groyne. An objective of this study is to explore wave driven flow patterns around three groynes in a field, situated on the Durban beach front. A similar study, for a single groyne, has been previously conducted by Lucca, (2013). Figure 1-1 depicts the study area, which is located on the east coast of South Africa in the province of KwaZulu-Natal.

The results of the study will assist with better understanding of flow structure that develops within a groyne field for maintenance, beach nourishment and storm events. This understanding will assist with mitigation major causes of scouring failure that persist in impermeable groynes.

Figure 1-1: Map overview of the study location in South Africa Durban reproduced from **(Olij, 2015)**

1.2 Study background

The instability of Durban's beach morphology has been a cause for concern to local government authorities, environmental conservationists as well as numerous beach-goers for many years (Barnett, 1999).

The littoral drift used to bypass the Port of Natal harbor entrance thus supplying the beaches north of the harbor. This resulted in the formation of sand bars across the harbor. Kwa-Zulu Natal became a British Colony during the 1840's and was identified as 'Natal' in this period, there were expectations from the government that the port would become a gateway trade with the interior. Unfortunately, this could not be realized due to the harbor's difficult access. The sand bar accumulation across the harbor entrance proved to be a danger to shipping. A number of ships were wrecked by the sand bar (Barnett, 1999). The gradual development of the harbor between 1851 and 1926 led to the need for the harbor entrance to be dredged deeper. The purpose of dredging was to prevent the entrance channel from being blocked by littoral transport. Dredging solved the ship access problem but not the disturbance to the natural littoral drift process.

In 1882, the south breakwater was constructed to reduce channel sedimentation (Barnett, 1999). Due to the breakwater extending over the surf zone, sediment was prevented from moving freely across the

harbor entrance. This aggravated the problem as there was a risk of accretion due to breakwater sheltering effect and erosion of beaches down drift due to lack of supply.

The situation became worse as dredging operations increased. Heavy sediment losses from the central beaches north of the harbor were experienced in the period 1903-1926 (Barnett, 1999). Numerous attempts were made to rectify the problem; the solutions included nourishment schemes, sand trap system, construction of different types of groyne systems, etc. Most of these schemes either failed completely or did not fully live up to their expectations for a number of reasons which are discussed in detail by Barnett, (1999).

Figure 1-2 shows different groyne systems that were implemented with their respective sand pumping schemes discussed by Barnett, (1999). The following is a brief summary:

- There is no clear date regarding the installation of the first wooden groynes on the Durban beach, but by 1932 these ineffective structures were in place. Therefore in 1938 a sand pumping scheme was implemented as a solution to beach erosion problem. This solution proved unsuccessful and was discontinued in 1949.
- From 1950 to 1954 a second sand pumping scheme referred to as the Cave Rock Bight Scheme was implemented. Two rubble mound high level Peterson groynes were constructed between 1954 and 1956 in an attempt to reduce erosion. However the resulting sand yield of the construction of the groynes did not live up to expectations. Although some beach areas were retained, severe local erosion occurred in other areas.
- In the late 1970's, the CSIR suggested the implementation of a sand-pumping scheme together with a system of low level groynes. Low level groynes alone are not able to trap the sediments and maintain the beaches, therefore nourishments of the beaches was necessary, thus the sand-pumping scheme. Two low level groynes were constructed between 1983 and 1985 to replace the old Peterson Groynes and a third groyne was built between 1987 and 1989 to further foster the replenishment of Durban's beaches.

Figure 1-2: Types of groyne systems implemented over the years at Durban beach front in trying to solve coastal erosion (Barnett, 2011)

All three areal images of the groynes were taken from the south side facing north of the Durban coastline. The groyne field in Durban coast line dates back to the early 1930's. As shown in Figure 1-2, permeable wooden pile groynes were the first documented groynes constructed (far left image taken in 1932). The complete failure of the sand bypass system between 1938 and 1949 prompted the removal of these groynes and construction of old Peterson groynes in the early 1950's (central image taken in 1979). The groyne system evolved to low level groynes that are present today (far right image taken in 1990). The literature suggests that the evolution of the groynes was due to the great challenge of beach erosion north of the groynes. The groynes alone did not offer complete coastal protection against erosion. It was evident that an effective consistent nourishment scheme is necessary.

1.3 Durban coastline climate

Durban coastline consists of a number of coastal defense structures (e.g. groynes, jetties, breakwaters) due to Durban dynamic wave conditions. Wave conditions in the area dictates for proper coastal protect and beach nourishment. The Durban beach profiles have been measured since 1973 using a theodolite referenced to fixed benchmarks (Corbella & Stretch, 2012c). The Durban Bight is shown in Figure 1-3. The Durban harbor entrance can be seen from the figure on south side and the groyne field is shown centrally on the shoreline.

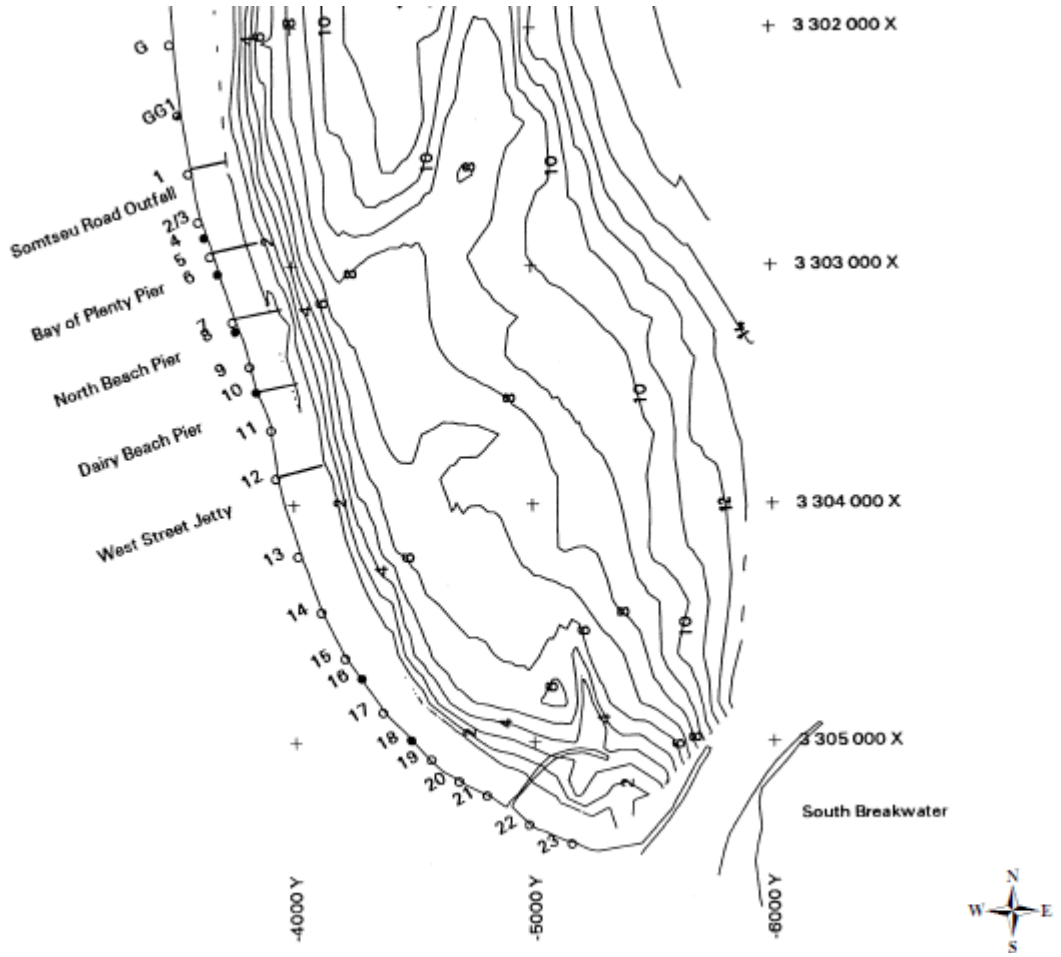

Figure 1-3: Durban beach profile surveyed in July 1995 showing the beach profile on the harbour entrance and along the groyne field. (Schooness, 2000)

Corbella & Stretch, (2012b) recently undertook a study in formalizing Durban coastline wave data for coastal design purposes. The data was last formally reviewed by Rossouw, (1984) and was thus outdated. The Durban wave conditions have been measured from instruments at three different offshore locations. The instruments used have been Wave rider buoys (non-directional and directional) and an Acoustic Doppler Current Profiler (ADCP). The Durban coastline experience different kinds of storm

wave forcing generated off the coast. Cold fronts are more frequent compared to tropical cyclones and cut-off lows. They are typically closer to the coast than the other wave forcing and move from west to east. Corbella & Stretch used 18 years of wave data to derive east coast wave conditions from the Durban and Richards Bay Waveriders. Table 1-1 summarizes the main findings.

Table 1-1: Average Durban wave climate (Corbella & Stretch, 2012b)

Average peak period	10.0 seconds
Significant wave height (H_s)	1.65 m
Average wave direction	130 degree

Over the period of the wave instruments, there have been two notable storm events which had devastating effects on the Durban shore line in 1998 and 2007. The 2007 storm event was the largest recorded wave event and the storm coincided with the highest astronomical tide of that year. The event has been associated with the cut off lows generated further offshore compared to cold fronts. Barnett, (2011) provides photographs of other storm events which occurred in October 1908 and March 1934. These events appeared to result in severe coastal impacts but to the author's knowledge were not formally documented. The wave rose prepared by Corbella & Stretch, (2014) for Durban wave data is shown in Figure 1-4. Corbella & Stretch, (2012c) defined a storm event as an event where by a significant wave height threshold is exceeded. A Durban storm event is considered to commence when the significant wave height exceeds 3.5m and ends when the wave height falls below 3.5m for a period of at least 2 weeks depending on the decay time of the autocorrelation. The significant wave height of 3.5m threshold was used to delineate events that cause significant erosion from the events that do not, based on available records of beach profiles.

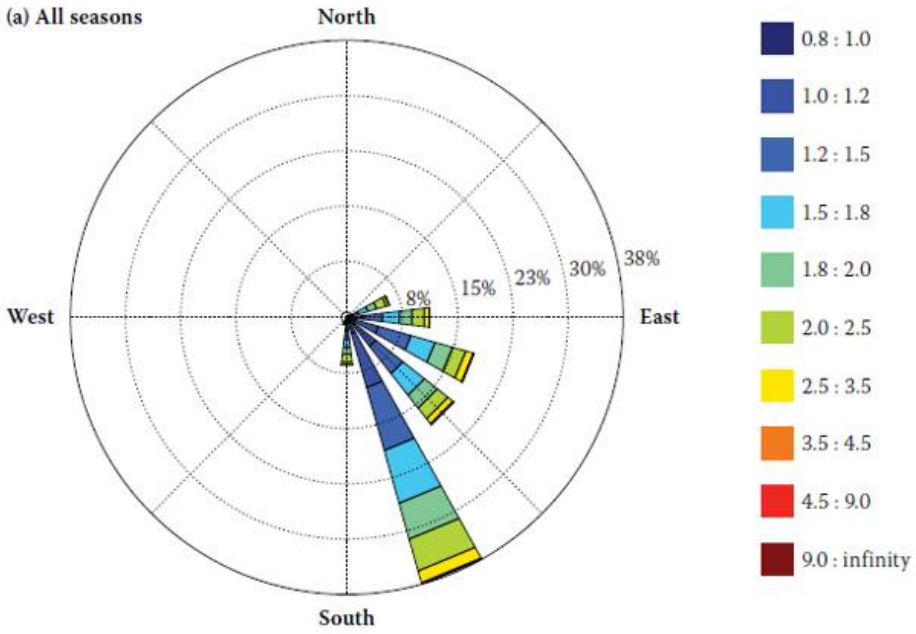

Figure 1-4: Wave rose for Durban and Richards Bay wave data showing various significant wave heights, wave direction and percentage distribution adapted from (Corbella & Stretch, 2014).

1.4 Research question

The following questions were addressed in this study:

- How are the flow patterns around impermeable groynes affected by wave conditions and groyne spacing?
- What are the possible implications on sediment transport, erosion and accretion?

1.5 Aim

The aims of this study were as follows:

- To describe the eddy circulation patterns associated with varying metocean parameters and inter-groyne spacing in a groyne field
- To describe the effect of circulation patterns in a groyne field on sediment accretion and erosion
- To ascertain the metocean conditions in which groyne tip position is critical in terms of scour failure

1.6 Objectives

- Review relevant literature on the properties of groynes and associated flow patterns
- Set up MIKE 21 model consisting of a groyne field
- Investigate eddy circulation patterns associated with varying:
    - Significant wave height

- Incident wave angle
- Water level
- Storm event

- To elucidate the effect of storm conditions on the groyne field using a selected threshold significant wave height
- Investigate suitable groyne inter-spacing from a parametric study using a MIKE 21 numerical model
- Investigate suitable groyne geometry from a parametric study using a MIKE 21 numerical model
- Investigate sediment movement in the vicinity of a groyne structure under various wave forcing conditions

1.7 Dissertation Outline

The dissertation outline is as follows:

Chapter 2 discusses literature on different types of groynes and their advantages with respect to hydrodynamic processes. It further discusses the hydrodynamics behind breaking waves, wave induced current, alongshore current and the effects on the groyne structures. Previous studies on groynes are also discussed.

Chapter 3 discusses the methodology used in setting up the numerical model. The numerical model used and the methods applied are discussed in detail. This includes discussions of the model build up, model calibration and simulations conducted.

Chapter 4 discusses the results from the model simulations. Wave parameters and groyne interspacing are varied to elucidate their respective effect on flow patterns and rip current in a groyne field.

Chapter 5 presents the conclusions drawn from the simulations and findings. Research short comings and recommendations for further studies are also presented.

2. LITERATURE REVIEW

Chapter two discusses literature behind different types of groynes, their application and beach nourishment. The hydrodynamics behind the formation of wave induced current, erosion and wave breaking processes are reviewed

---

2.1 Introduction

Groynes are one of the oldest forms of hydraulic structures (Lee, *et al.*, 2011). Numerous studies have been conducted over the years to establish best function of a groyne or groyne field in a stretch of coast line. However, still there exist substantial uncertainties on their functions. The function of a groyne system is to limit or block sediment transport by inducing accretion within the groyne field. The seabed is therefore raised and the waves are forced to breaker further sea ward. This results in the zone of maximum energy dissipation to be shifting accordingly away from the shoreline (Trampenau, *et al*., 2004).

Literature suggests that permeable groynes offer far better advantages compared to impermeable groynes e.g. Bakker, *et al*. 1984; Tarnowska, *et al*. 1992. A number of field experiments have been conducted on this subject. Some of these studies include field study conducted by Poff *et al.,* (2004) on the impact of permeable wooden groynes on the coastal system, Walker *et al.,* (1991) on sediment transport near groynes especially etc. Groynes generally function best in areas where there is strong longshore sediment transport which requires retention (Dean & Dalrymple, 2004; Zanuttigh, *et al*., 2005). The two types of groynes are briefly summarized in the following section.

2.2 Types of groynes

2.2.1 Permeable groyne

Permeable groynes are typical low-crested structures perpendicular to the shoreline and allow water to penetrate through. The structures are generally used on beaches with small sediment deficit. The function of the groyne is to slightly reduce the littoral drift in the inner surf zone and to create a more regular shoreline (Trampenau, *et al*., 2004).

Permeable groynes are used to provide artificial hydraulic resistance and are meant to reduce the longshore current velocity (see Figure 2-1) and thus reduce the rate of longshore sediment transport (Bakker, *et al*., 1984; Poff, *et al*., 2012). The permeability of a groyne is defined by the degree of resistance to flow passing through it and can also be defined by a ratio of open area to total cross

sectional area. A groyne with high permeability implies low resistance to longshore flow while a groyne with low permeability implies high resistance to longshore flow (Ballard, 1991).

Poff *et al.*, (2004) observed the effects of permeable groynes on tidal and wave induced currents through laboratory experiments. The results showed that with careful design, permeable groynes can have many beneficial qualities for shoreline protection and therefore are generally preferable to impermeable groynes. The major benefits of permeable groynes are their low construction and maintenance costs, induced decrease in longshore sediment transport, induced reduction in both tidal and wave induced currents and the induced reduction in erosion on the leeward side of the groyne (Poff, *et al*., 2012; Ballard, 1991; Trampenau, *et al*., 2004).

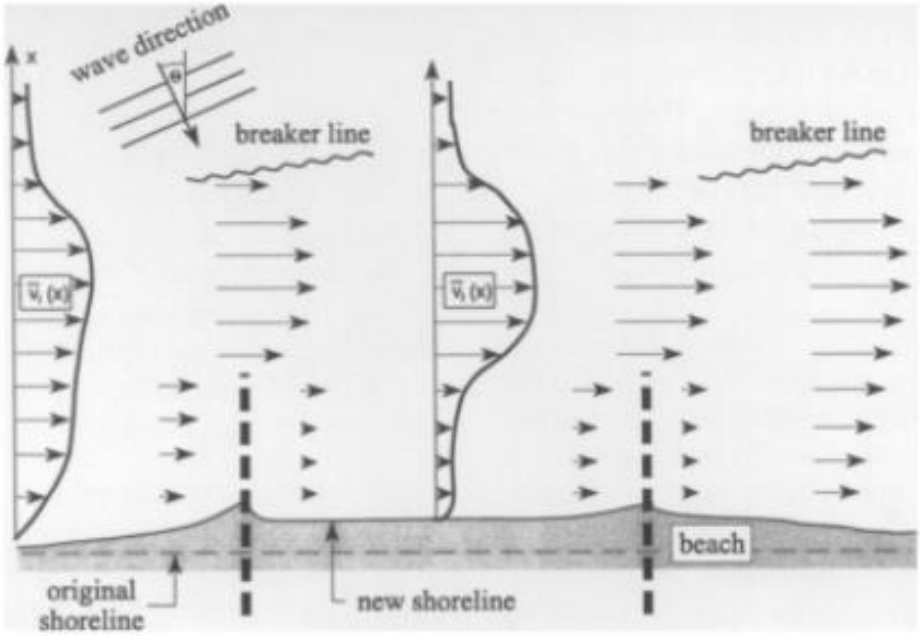

Figure 2-1: Resulting longshore current and sediment transport within permeable groyne field adapted from (Trampenau, *et al*., 2004). The presence of permeable groynes reduces the velocity profile as the current passes through the groynes. The sediment is thus retained while the breaker zone moves further offshore therefore limiting coastline erosion.

2.2.2 Impermeable groyne

Impermeable groyne tend to induce blockages of nearshore current and restricts water penetration through. The longshore sediment transport is thus interrupted over the entire groyne length. This type of groyne is used to keep sediment within compartments between adjacent groynes. There are hydrodynamic, morphodynamic and morphological changes as a result of the sediment blockage. The nearshore zone establishes new equilibrium conditions within the submerged part of the beach profile. The sediment build-up on one side of the groyne results in accretion and the lack of supply downstream results in erosion. This phenomenon is depicted on Figure 2-2. Furthermore the impermeable nature of the groyne can result in alongshore current being directed seaward creating rip current. Deviation of the

longshore current can have detrimental consequences on the groyne structure especially the groyne tip. Rip currents can cause local scour along the groyne and can results in structural failure of the groyne and seaward sediment transport (Trampenau, *et al*., 2004)

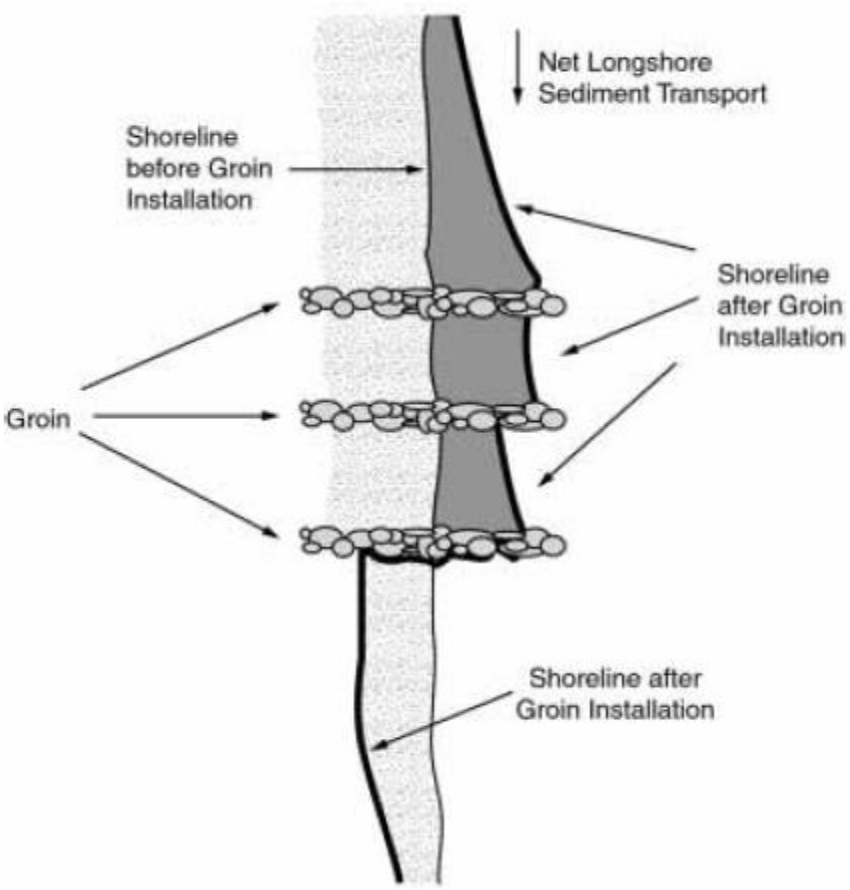

Figure 2-2: Effect of impermeable groyne field on a stretch of coastline. A saw tooth phenomenon whereby the shoreline extend/retreat occurs as a result of accretion upstream and erosion downstream of impermeable groyne field. (Dean & Dalrymple, 2004)

2.3 Coastal processes

2.3.1 Wave induced current

Currents in near shore zones may be generated by tides, sustained winds, river outflows and wave breaking (Muir Wood & Fleming, 1981). The most common near shore currents are generated by waves breaking at an angle to the shore. Wave induced current and surf zone activities are the main driving force for the longshore sediment movement and processes (Castelle, *et al*. 2006; Muir Wood & Fleming, 1981). The longshore current can be intercepted by a structure such as a groyne or a jetty oriented normal to the shore. The current is then deflected off shore causing a rip current and energy dissipation

(refer to Figure 2-3). The new current will begin downstream of the structure and develop again (Muir Wood & Fleming, 1981).

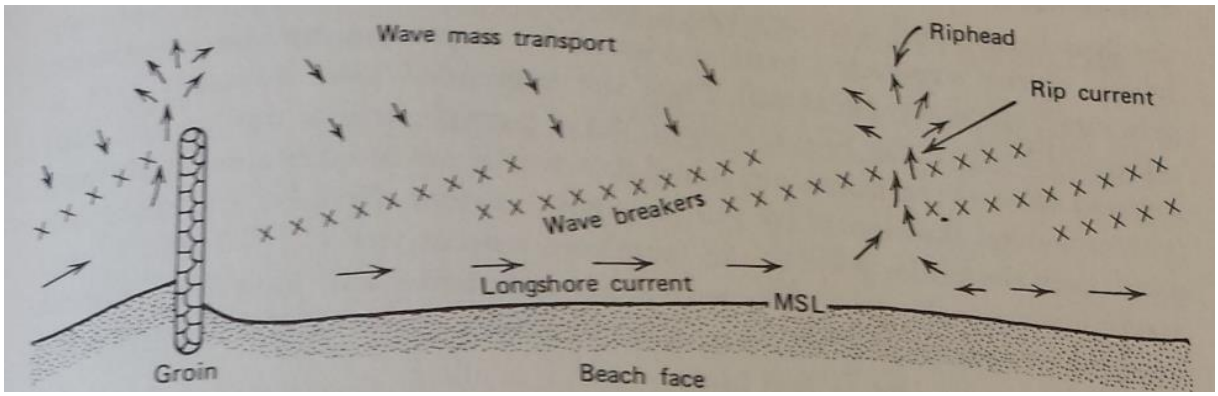

Figure 2-3: Impermeable groyne diverts all the longshore current seaward, which may result in rip current formation on the sides of the groyne. Rip current is responsible for sediment lost out at sea (Muir Wood & Fleming, 1981)

As waves propagate towards the coast, wave heights vary with depth and waves break resulting in wave induced current and wave setup (Jing-xin & Hua, 2010). The wave induced current is thus responsible for longshore current, littoral drift and near shore morphological evolution. In Figure 2-4, typical alongshore velocity is shown. The alongshore current occurs when the momentum is transferred from the wave motion to the mean flow (Bosboom & Stive, 2012). It is this current velocity that groynes in the nearshore zone resist thus slowing down sediment transport. Wave-induced current presents different features such as wave set up or set down, undertow, longshore current, and rip currents. These currents usually superpose each other to form an extremely complex circulation system (Mingxiao, 2011). The development of wave-induced current may drive nearshore mixing and transport processes (Jing-xin & Hua, 2010).

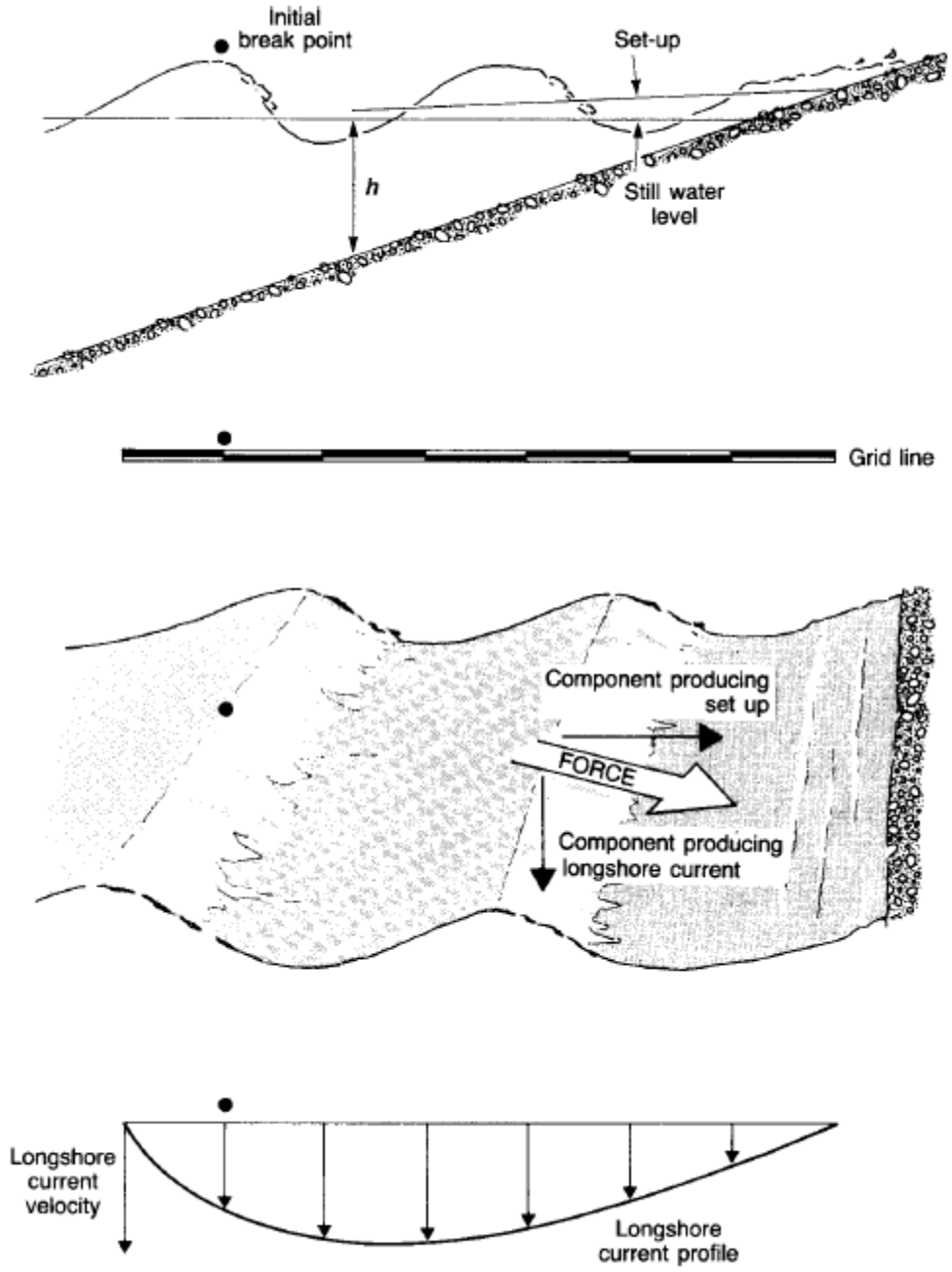

Figure 2-4: Longshore current velocity in the near-shore zone responsible for sediment movement. The longshore current velocity typically peaks at a breaker line (a region where majority of the waves break) and reduce as the waves dissipate energy toward the shore line. (Reeve, *et al*., 2004)

Residual momentum flux (radiation stress) is recognized as the primary driving force for wave-induced current (Muir Wood & Fleming, 1981). The longshore component of the radiation stress is responsible for longshore current in oblique shoaling waves (Longuet-Higgins, 1970). Longshore current speed reaches its peak at a distance shoreward of incipient breaking. The maximum longshore current velocity peaks on the breaker line (Muir Wood & Fleming, 1981). The breaking wave orbital velocity is defined by Muir Wood and Fleming, (1981) and given as

$$u_m = \frac{1}{2}\sqrt{gH_b} \quad (2\text{-}1)$$

where u_m is the wave orbital velocity, H_b is the breaker height and g is the gravitation acceleration constant.

2.3.2 Coastal erosion

Coastal erosion has played a major role in shaping the present coastlines (van Rijn, 2011; Zanuttigh, *et al*., 2005). Coastal erosion occurs when sediment transported to a section of the coast is different to sediment leaving the section. Positive gradient in the longshore transport rate results in erosion while a negative gradient result in accretion (Bosboom & Stive, 2012). Sediments are continuously stirred up by the waves and transported by the longshore current in the surf zone. The impact of long structures such as groynes on the morphodynamic of the adjacent coasts can be very large (Castelle, *et al*., 2006).

Coastal protection structures (i.e. groynes, breakwaters, piers) tend to interrupt the wave-induced longshore current and sediment transport. The immediate and long term effect on the coastal coastline can be severe. Impermeable groynes in particular tend to induce accretion and erosion (see Figure 2-5).

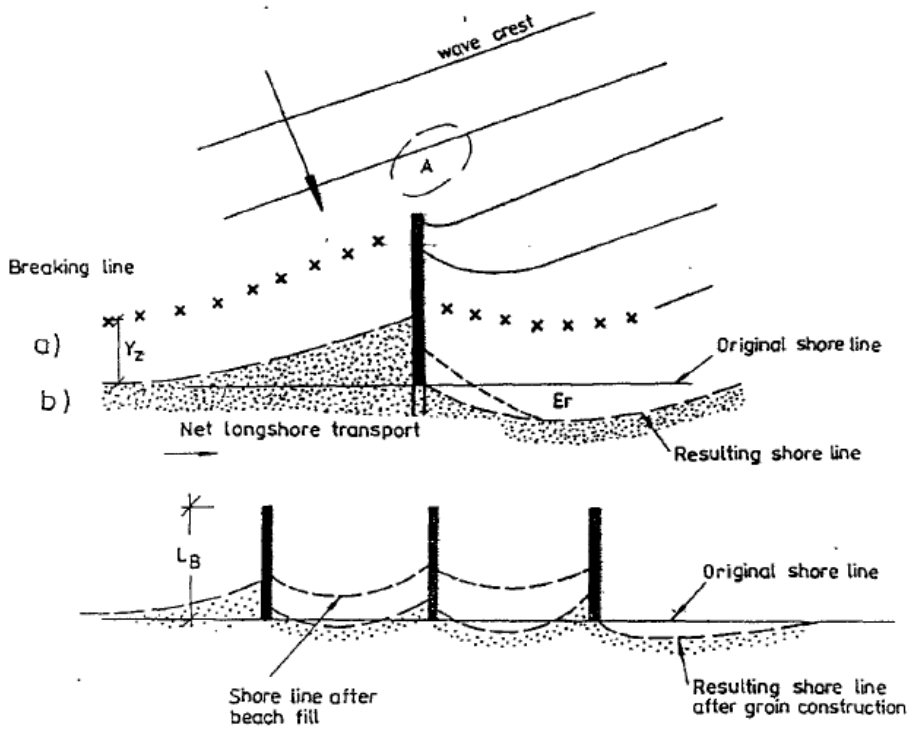

Figure 2-5: The effect of cross shore structures such as a single groyne or groyne field on net longshore transport. Accretion on the up drift side and erosion on the down drift side of a groyne can be expected, particularly with impermeable groynes (Tarnowska, *et al*., 1992).

This problem of sedimentation/erosion can be avoided with an implementation of a nourishment plan (i.e. sand bypass system). The sand bypass system traps sediment on the updrift side of an obstruction

where sediment is collected and makes it easier to transport sediment to the down-drift side (Castelle, *et al*., 2006). Solving coastal challenges requires better understand of coastal vulnerability and the effective coastal retention processes that may be used to mitigate these processes. The design of coastal protection structures such as groynes should find a balance between the need for coastal protection and the need to minimize impacts on the surrounding environment (Hawkins, *et al*., 2007).

Through the use of existing data on the east coast of South Africa (Durban), Pringle (2015) developed a stochastic wave simulation shown on Figure 2-6.

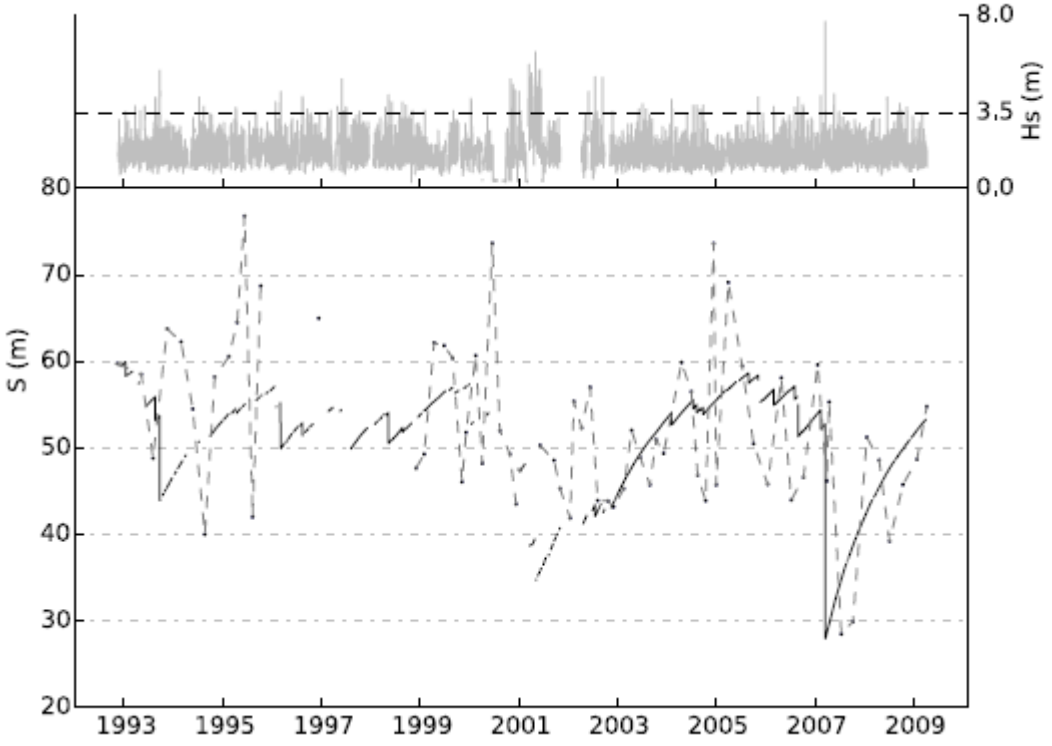

Figure 2-6: Pringle (2015) observed and modelled data for Durban beach profile in the period 1993-2009. The two trends represents significant wave height (top graph) and shore line position (bottom graph). The shoreline position graph consists of observed shoreline position (dash line) and the modelled shoreline position (solid line). (Pringle, 2015).

The three plotted time histories in Figure 2-6 show a consistent relationship between high significant wave height (H_S > 3.5m) and shoreline erosion. It can be observed that for high significant wave height, the observed and modelled shoreline position suggest shoreline retreat. Pringle's findings indicate clear signs of significant beach erosion under storm conditions where the significant wave height is greater than 3.5m (Corbella & Stretch, 2012b). It is clear from these results that storm conditions are detrimental to the stability and sand supply of beaches. It is therefore imperative to explore the effect of storm conditions on the flow structure within coastal structures such as groynes that are intended to help protect beaches.

2.3.3 Longshore sediment transport

Waves breaking at an angle to the shoreline cause wave-induced currents that are responsible for longshore sediment transport occurring in the surf zone (Muir Wood & Fleming, 1981). Coastal sediment transport is divided into two components: cross shore transport which is perpendicular to the coastline and longshore transport or littoral drift which is parallel to the coastline (e.g. Reeve, *et al*., 2004). Ocean waves are the primary cause of sediment transport and morphological changes in the nearshore region. The concept of longshore sediment transport is based on the concept that sediment is disturbed on the sea bed and stirred up by shear stress due to the combination of tidal and/or wave-induced currents (Bakker, *et al*., 1984). Sediments are transported as a combination of bed load and suspended load in the nearshore zone. Suspended sediment transport accounts for most sediment transport, particularly during storm conditions (Walker, *et al*., 1991; Bakker, *et al*., 1984).

Structures such as breakwaters, groynes, etc., built in the nearshore zone can alter local waves, flow patterns, and sediment transport. There are numerous cases (presented in section 2.6) where these structures are built to bring about beneficial changes to the nearshore zone but sometimes bring about adverse effects. Beach nourishment strategies rely on optimal placement of sediment. It is therefore imperative to accurately predict potential changes that the structure may induce within the nearshore zone (Walker, *et al*., 1991).

Literature suggests that groynes shorter than the width of the breaker zone are used to stop a small portion of sand transport while longer groynes tend to reduce the sediment transport to nearly zero. This will unnecessarily maximize lee-side erosion (Castelle, *et al*., 2006). However, the erosion will be time dependent and the shape of the shoreline will eventually adapt.

2.4 Hydrodynamic and morphodynamic driving forces

2.4.1 Breaking waves

Wave breaking is said to be a difficult hydrodynamic problem due to its complexity (Dean & Dalrymple, 2004). Wave breaking is responsible for the dominant physical process in the surf zone whereby the energy of wind waves and swell is dissipated (Battjes & Stive, 1985). A number of studies have been conducted to better understand this phenomenon. When waves go through the transition phase they are refracted and enter the shallow water region, breaking before reaching the shoreline (Reeve, *et al*., 2004). The wave breaking process is depth-induced and occurs when waves propagate into shallow water and the wave height can no longer be supported by the water depth (DHI, 2012b; Chen & Li, 2014; Dean & Dalrymple, 2004; Guza, 1983). The process occurs as a result of a kinematic instability. The process does not only occur in shallow or transitional waters but can also occur in deep water due to excessive energy input mostly from wind (Dean & Dalrymple, 2004).

As the waves start to break, wave energy dissipation occurs. This is described in Guza, (1983) to be a dominant energy dissipation mechanism. Reeve *et al.,* (2004) notes that it is common practice to apply refraction analysis up to the breaker zone because the inherent inaccuracies are small compared to deep water waves. The breaker zone is the nearshore area where the majority of waves break.

Waves break and produce a current that is referred to as wave-induced current. This current is the dominant driving mechanism for sediment and pollutant transport, morphological evolution and flushing within the nearshore zone (Jing-xin & Hua, 2010, Mingxiao, 2011).

There are a number of empirical equations used to determine wave height at a point of breaking. Wave breaking is dependent on two criteria, namely wave steepness and a limit on the wave height to water depth ratio or breaker index (Reeve, *et al*., 2004). The two equations are given as

$$H/L < 1/7 \qquad \text{(wave steepness normally limits the height of deep-water waves)} \qquad (2\text{-}2)$$

$$\gamma = H/h = 0.78 \qquad \text{(breaker index)} \qquad (2\text{-}3)$$

where γ is the breaker index, H is the wave height, L is the wave length and h is the water depth. The breaker index is dependent on the beach slope and breaker type and varies from 0.4 to 1.2. Sabatier, F. (2006) found two indices that can be used to predict wave breaking similarly to that of Reeve, *et al*., (2004). The breaker depth index $\gamma = 0.78$ is the commonly used criteria in engineering practice as the first estimate (Dean & Dalrymple, 2004; Sabatier, 2006).

Breaking waves can be classified into three types namely spilling, plunging and surging waves depending on the Irribaren number or surf similarity parameter (Reeve, *et al*., 2004; Chen & Li, 2015)

$$\xi_b = \frac{tan\alpha}{\sqrt{H_b/L_b}} \qquad (2\text{-}4)$$

where $tan\alpha$ is the beach slope, H_b is the wave height and L_b is the wave length at breaking. It is found that when (a) $\xi_b \leq 0.4$ wave breaking occurs as spilling breakers (b) $0.4 \leq \xi_b \leq 2.0$ wave breaking occurs as plunging breakers (c) $\xi_b \geq 2.0$ wave breaking occurs as surging breakers.

The wave breaker type gives a good indication of the expected wave conditions, beach aggregate types and hydrodynamic forces expected on coastal structures. Due to the randomness of breaking of wind generated waves a number of models recommended in studies such as Battjes, (1972) and Goda, (1975) that are used to predict onshore variation of radiation stress and wave energy are not well founded (Battjes & Stive, 1985). The models did not consider sources and sinks when expressing the local mean wave energy in random breaking waves. Battjes and Janssen (1978) presented an approach where by the local mean rate of energy dissipation can be modelled during the wave breaking process. The variation of the mean wave energy density is required for quantitative predictions of wave-induced sea level variations and currents in the nearshore region. The methods used to predict random breaking

waves have been presented by Battjes, (1972) and Goda, (1975). In the methods the energy dissipation rate due to breaking is not estimated independently, which prompts a need to base the approach on the energy balance. This is a shortcoming.

The energy balance equation for a given incident wave and beach profile where the mean wave energy density (E) varies with the distance to the shoreline is given by

$$\frac{\partial P_x}{\partial x} + D = 0 \qquad (2\text{-}5)$$

$$E = \frac{1}{8}\rho g H_{rms}^2 \qquad (2\text{-}6)$$

where P_x is the x component of the time mean energy flux per unit length approximated as EC_g (with C_g the wave group velocity according to linear wave theory), H_{rms} is the root mean square wave height and D is the time mean dissipated power per unit area (Battjes & Janssen, 1978; Guza, 1983). Wave decay is weak outside the surf zone where D is often neglected completely (Battjes & Janssen, 1978). The maximum breaker height equation is given by

$$H_m \cong 0.88k^{-1}\tanh(\frac{\gamma}{0.88}kh) \quad \text{(deep water)} \qquad (2\text{-}7)$$

$$H_m \cong 0.88h \quad \text{(shallow water)} \qquad (2\text{-}8)$$

where $k = {}^{2\pi}/_{L}$ is the wave number, $H_m$is the maximum breaker height, γ is the breaker index and h is the breaker depth (Battjes & Janssen, 1978).

2.4.2 Radiation stress

Radiation stress is defined as the sum of residual wave momentum flux and hydrodynamic pressure averaged over a wave period at different depths (Huayong, *et al*., 2004; Longuet-Higgins & Stewart, 1964). If a wave train is reflected from an obstacle, its momentum must be reversed. Conservation of momentum requires that there be a force exerted on the obstacle equal to the rate of change of a wave momentum (Longuet-Higgins & Stewart, 1964). Reeve, *et al*. (2004) defined radiation stress as excess flow momentum due to the presence of waves and result of the orbital motion of individual water particles in the waves. The orbital motion of the water particles produce a net force at right angle to the direction of propagation denoted by S_{yy} and net force in the direction of propagation denoted by S_{xx}. The radiation stress is responsible for hydrodynamic processes such as wave induced current and sediment transport in the surf zone. The radiation stress is computed from the linear wave theory equation and is divided into normal and shear components. This is done by integrating dynamic pressure over the total depth under the wave and over the wave period, and subtracting the integral static pressure below the still water depth as depicted in Figure 2-7 and Figure 2-8.

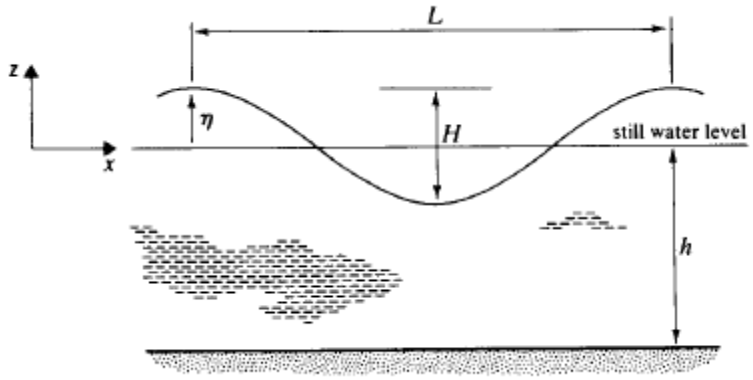

Figure 2-7: Profile showing sinusoidal wave progression and still water level (Reeve, *et al*., 2004)

The linear wave theory is given as

$$\eta = \frac{H}{2} cos 2\pi (\frac{x}{L} - \frac{t}{T}) \quad (2\text{-}9)$$

where η is the deviation from mean water level to any point x, H is the wave height, a is the amplitude, x is the horizontal axis, L is the wave length t is the time and T is the wave period. The normal radiation stress components are given as

$$S_{xx} = \int_{-h}^{\eta} (p + pu^2) dz - \int_{-h}^{0} p dz \quad (2\text{-}10)$$

$$S_{yy} = \int_{-h}^{\eta} (p + pv^2) dz - \int_{-h}^{0} p dz \quad (2\text{-}11)$$

$$p = -\rho g z \quad (2\text{-}12)$$

where S_{xx} is the net force in the direction of propagation, S_{yy} is the net force at right angle to the direction of propagation, S_{xy} is the flow of x momentum across the plane, p is the hydrostatic pressure, z is the distance measured upwards from the mean surface, ρ is the density of the fluid, g is gravity, u is the horizontal component of orbital velocity in the x direction and v is the horizontal component of orbital velocity in the y direction(Longuet-Higgins & Stewart, 1964; Reeve, *et al*., 2004). The shear component of the radiation stress is given as

$$S_{xy} = \int_{-h}^{\eta} \rho u v dz \quad (2\text{-}13)$$

The components of the momentum flux can be seen in Figure 2-8.

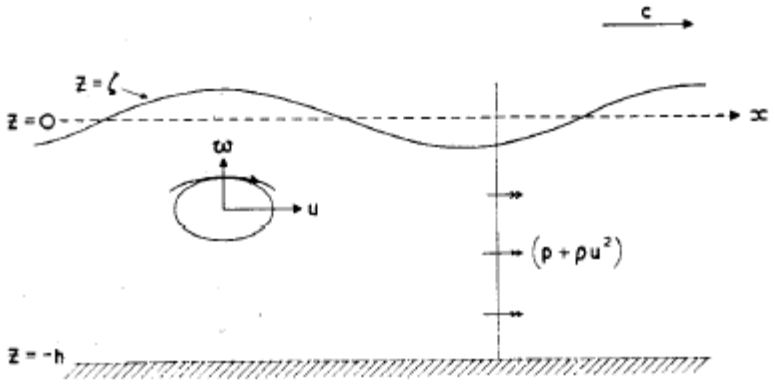

Figure 2-8: The momentum flux in a progressive wave (Longuet-Higgins & Stewart, 1964)

When conducting a numerical simulation, radiation stress is widely applied in a two dimensional, depth-averaged manner. It is more accurate to use a three dimensional application as this closely matches the processes observed in natural waters (Zhang, *et al*., 2009; Bing-chen, *et al*., 2010). The numerical model used in this study only allows for two dimensional modelling.

2.5 Residence time

Numerous studies that have been conducted on groynes, focused mainly on the hydrodynamic and morphological functioning of a groyne. Studies such as Trampenau, *et al*. (2004) and Walker, *et al*. (1991) establish the advantages and disadvantages of both permeable and impermeable groynes and strongly recommend the use of permeable groynes compared to impermeable groynes. Trampenau, *et al*. (2004) and Pattiaratchi, *et al*. (2009) found that impermeable groynes function as a guide wall and are dominated by rip current and eddy circulation zones.

Trampenau, *et al*. (2004) found eddy circulations to be larger for impermeable groynes compared to permeable groynes. Circulation zones result in sediment retained between the groynes and may result in poor water circulation between the groynes. Poor water circulation can have detrimental effect on the pristine nearshore zone environment. Although some of the studies gave a descriptive understanding on alongshore current resistance and sediment retention within the groyne compartments, there were no studies found that looked into the implications on water quality between the groynes. Therefore there exists a gap in exploring residence time in a groyne field.

Residence time has been extensively explored by a number of studies (i.e. Wang, *et al*. 2004; de Brauwere, *et al*. 2011 and Kenov, *et al*. 2012) on rivers, lakes and estuaries to establish water circulation. Residence time is defined as an average time a water parcel exist in a water system or water body until flushed out (Wang, *et al*. 2004; Kenov, *et al*. 2012). It is a convenient parameter that can be used in representing a time scale of physical transport process. Residence time was used successfully by de Brauwere, *et al*. (2011) in estimating a contaminant exposure time period in Belgium Scheldt

Estuary through the use of a numerical model. The river is located in a highly dense area. Literature presents numerous methods that can be used in estimating residence time. One of the methods is the freshwater fraction model which is widely used in estuaries (Kenov, *et al*., 2012). The time can be estimated by dividing two parameters of the freshwater volume (V_{vol}) and the inflow rate (Q) averaged for a given time period. The method takes into account a freshwater fraction used to quantify freshwater from sea water through the use of salinity of the estuary and sea. The water and salt budget method is another method used to estimate residence time. The two methods are similar only differing in one aspect. The freshwater water method uses the inflow rate while the water and salt method uses the outflow rate. The water and salt method outflow parameter is calculated using Knudsen's hydrographic theorem (Wang, et al., 2004). The residence time (T_r) can be expressed as follows:

$$T_r = V_{vol}/Q_0 \quad (2\text{-}14)$$

In this study, V_{vol} is the volume of water in a compartment between two groynes and Q_0 is the total inflow in a groyne compartment. The residence time is defined as an average time a water parcel resides within a groyne compartment until it escapes.

2.6 Previous research on flow patterns and sediment transport within a groyne or groyne field

Groyne structures have been successfully implemented for coastal protection world-wide (Poff *et al*, 2004), however in some cases their success is limited or completely detrimental (Tarnowska, et al., 1992). Studies such as Barnett (1999), Poff, *et al*. (2004) and Tranowska, *et al*. (1992) associate the short comings of groyne implementation to a lack of understanding of the hydrodynamic relationship between groynes and adjacent beaches.

Trampenau, *et al*. (2004) explored the hydraulic function of permeable groynes in a stretch of coastline. The study was conducted using laboratory experiments and field observations along the Baltic Coast, aimed to better understand hydraulic processes of permeable groynes, their advantages compared to impermeable groynes and practical recommendation for design purposes. The laboratory study was conducted in two phases; the first phase was conducted through subjecting a single groyne or groyne field to uniform longshore current while keeping wave conditions constant and the second phase involved progressively subjecting a series of groynes to oblique waves. The field study focused on morphological changes due to presence of permeable groynes. The level of flow constriction ratio was established by Tarnowska (1985) for impermeable groynes (Tarnowska, *et al*., 1992). The ratio best describes the functioning of a groyne and can be represented as $(\frac{G_L}{B_Z})$, where G_L is the groyne length in contact with the active water zone and B_Z is the breaker width measured from the shoreline.

Walker, *et al*. (1991) used the same ratio to explore sediment transport near groyne structures in the nearshore zone. Walker's study focused on morphological changes due to varying groyne permeability and other groyne properties such as the groyne length and spacing using a numerical model. Noticeable differences between the two studies include the following: Walker, *et al*. (1991) used a single groyne while Trampenau, *et al*. (2004) explored a groyne field. Despite differing methodology the two studies complimented each other. Trampenau, *et al*. (2004) states that there are difficulties in effectively utilizing the $\frac{G_L}{B_Z}$ ratio for permeable groynes due to the effect of permeability on the breaker zone. However, Trampenau *et al.* (2004) used the ratio by systematically reducing the groyne length arbitrarily to account for permeability. The $\frac{G_L}{B_Z}$ ratio measures the level of flow constriction around a groyne. The result of the study can be summarized as follows:

- For high flow constriction large circulation eddies develop between groyne compartments with relatively low velocity, and $\frac{G_L}{B_Z} = 1$.
- For low flow constriction elliptical, relatively smaller eddies develop between groynes and downstream with relatively high current velocity on the lee side of the groyne, and $\frac{G_L}{B_Z} = 0.625$.

Trampenau, *et al*. (2004) results summary is depicted on Figure 2-9.

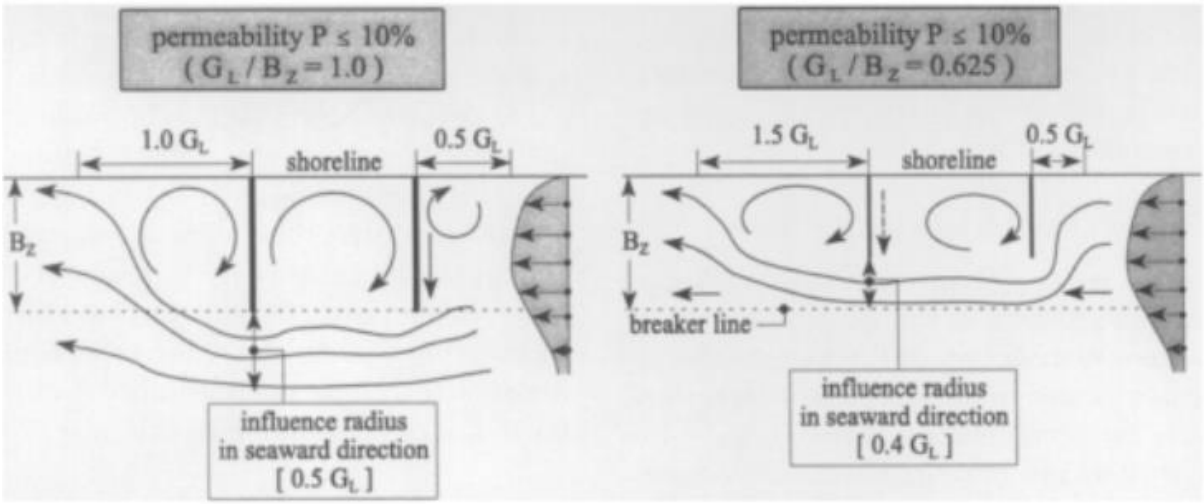

Figure 2-9: Flow patterns observed by Trampenau, *et al*. for high level and low flow constriction in an impermeable groyne field (adapted from Trampenau, *et al*. 2004)

Trampenau, *et al*. (2004) also used the groyne spacing to groyne length ratio in a groyne field to explore the effect on the water level. The ratio can be represented as $(\frac{G_S}{G_L})$, where G_S is the groyne interspacing distance and G_L is the groyne length in contact with the active water zone. Trampenau, *et al*. (2004) study did not explore the combined effect of permeability and groyne spacing to groyne length ratio.

The study found that groyne spacing to groyne length ratio affects the formation of gravity current ($V_{\Delta h}$) between groynes due to differential water levels between groyne compartments (refer to Figure 2-10). This results in large eddies within the impermeable groyne field and an increase in longshore current. For conditions where the groyne spacing to groyne length ratio is small, gravity currents dominate the groyne system. This is of course undesirable due to negative effects on the groynes and the coastline such as large eddies formed between the compartments associated with low current velocity, sediment accretion in a groyne field and poor circulation. These effects can be mitigated by increasing groyne spacing to groyne length ratio or groyne permeability. In an optimal groyne field the gravity currents and the wave induced longshore currents are at equilibrium.

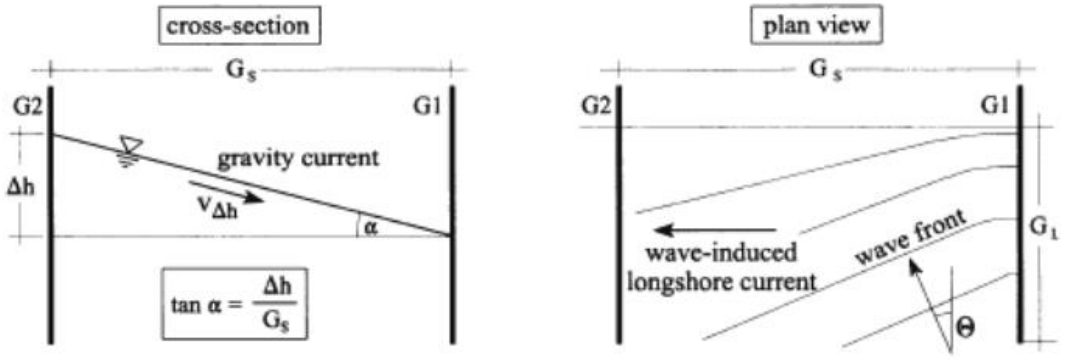

Figure 2-10: Gravity current development in a groyne field with relative low groyne spacing to groyne length ratio, water is bounded between groyne 1 (G1) and groyne 2 (G2) resulting in formation of a gravity current (Trampenau, *et al*., 2004).

The following conclusions can be inferred from the results of Trampenau, *et al*'s (2004). Impermeable groyne experiments:

- large eddies develop within the groyne field for low flow constriction
- A strong rip current develops along the trunk of the groyne
- Strong longshore currents develop at the groyne tip for high flow constriction

Tarnowska, *et al*. (1992) explored the effect of coastal defense measures that have been deployed in the Netherlands. The morphological changes in the near shore zone caused by the presence of groyne was elaborated and associated with the width of the breaker zone (B_Z). Rip currents have been known to develop along cross shore structures such as groynes and to create erosion problems (Pattiaratchi, *et al*. 2009; Tarnowska, *et al*. (1992). The groyne length to breaker width ratio was successfully used in studies such as Walker, *et al*. (1991), Trampenau, *et al*., (2004) and Tarnowska, *et al*., (1992) to identify areas around the groyne more prone to erosion or accretion. Local scour of impermeable groynes with length shorter than the breaker zone width $G_L < B_Z$ were found to develop towards the groyne tips while for impermeable groynes with length greater that the breaker zone width $G_L > B_Z$ was found to erode

toward the groyne midspan. Sediment was often found to travel seaward due to rip current for short groynes. This creates a deficit for downstream beaches.

The advantages of permeable groynes far outweigh their disadvantages, offering better benefits when compared to impermeable groyne (Trampenau, *et al*., 2004; Poff, *et al*., 2004). This was evident when Poff, *et al*., (2004) explored a case study on permeable wood groynes on the southern coastline of Naples beach. The impact of these groynes was evident on the beach according to the testimony of residents who observed the evolution of the beach after their installation. The groynes responded well by stabilizing the coastline within the zone of influence, decreasing longshore current and promoted sediment deposition along the shore line, and attracting fish and other sea life.

Poff, *et al*., (2004) quantified the effectiveness of wooden pile groyne field and provided understanding regarding their properties. The study consisted of series of laboratory experiments and a numerical model. The physical experiment involved the use of wave tank investigation to elucidate dominant hydrodynamic mechanisms and the evolution of the bathymetry due to the presence of permeable groyne field under controlled environment. Drag force coefficient, beach profile response and wave height reduction in the groyne field were investigated. A numerical model was developed to elucidate quantitative data on the groyne field and to serve as a basis of the physical experiment. The results for both experiments shed light on the influence of permeable wood groynes in reducing longshore current and limiting sediment transport across the groyne field.

Pattiaratchi, *et al*., (2009) conducted a study on the western coast of Australia aimed at describing rip currents and flow patterns around a single groyne through the use of Lagrangian and Eulerian techniques. To the author's knowledge they did not investigate sediment movement around the groyne. A numerical model and field experiment were used to compute flow patterns. The numerical model consisted of a single impermeable groyne and Eulerian measurement results were used as input to an idealized numerical model. Wave conditions were systematically varied to explore their effect on the current speed and flow patterns. Current meter and surf zone drifter measurements together with the numerical model re-affirmed the results of Trampenau, *et al*., (2004) regarding eddy circulation and rip current along the groyne. Both studies found that wave conditions dictate the size of the eddy circulation formed on the lee side of the groyne. However, Trampenau, *et al*., did not describe current convergence on the lee side of the groyne but did observe alongshore current divergence at the down drift extent of the lee side eddy circulation. This was explored extensively by Pattiaratchi, *et al*., (2009). The divergence point findings for both studies were similar with respect to stronger eddy circulation causing the divergent point to move further down drift.

Lucca, (2013) conducted a study on one of Durban's groynes at the Bay of Plenty (BOP). The study described flow patterns around a single groyne using field experiments and a numerical model. Lucca's study was motivated by scour around the groynes and associated structural problems (refer to Figure

2-11). In general, locally increased flow speeds at the tip of a groyne can cause scouring that can severely compromise the structural integrity of a groyne (Bakker, *et al*., 1984; Sumer & Fredsoe, 1996; Trampenau, *et al*., 2004). The Lucca's (2013) study involved collecting current and sediment data around the perimeter of the groyne.

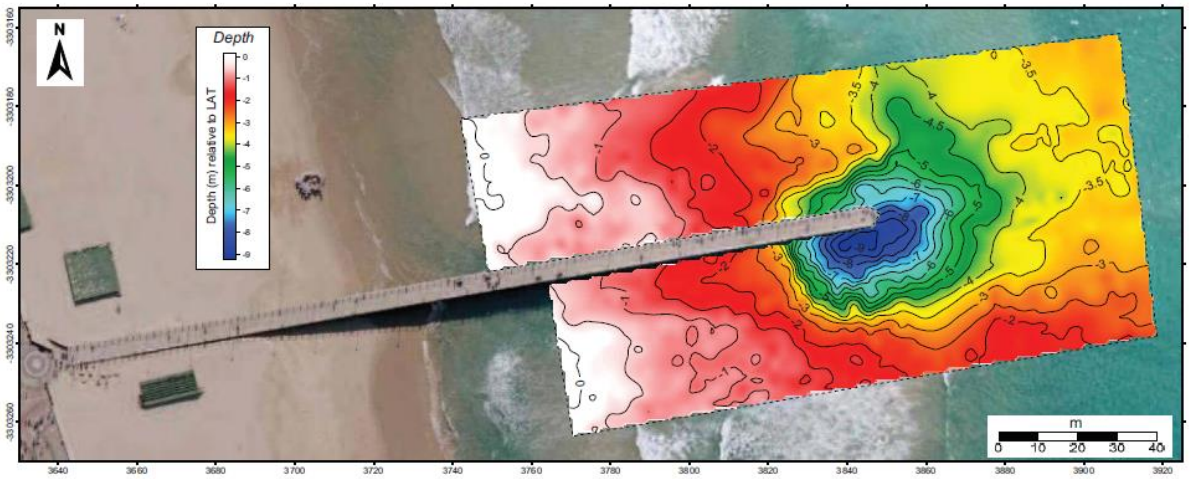

Figure 2-11: Bay of Plenty semi permeable groyne showing scour at the groyne tip during March 2012. **(EMS, 2016)**

Current data was collected for a period of 24 hours using 25 custom made current meters and one ADCP (Acoustic Doppler Current Profiler). Only 19 current meters were able to produce reliable data as 6 current meters were lost or damaged. For more on the methodology and calibration of the results, the reader is directed to Lucca (2013). Wave conditions when the measuring equipment was deployed were below average with a significant wave height of 1.4 m, a wave period of 9.05 seconds and an average incident angle of 116 degrees.

Lucca, (2013) compiled a current rose from the results as depicted on Figure 2-12. The current rose suggests strong peak currents occurring up-drift of the groyne, on the south side. The strongest average current on that day was 0.35m/s alongside the groyne and may be considered a rip current. The alongshore current was observed to be deflected seaward. The current was dominant in the cross shore direction with 52.5 % of the current speeds below 0.2 m/s, occurring mostly on the updrift side. Because the current profile showed a cross shore current as more dominant, Lucca suggested that the semi-impermeable groyne behaved more like an impermeable groyne.

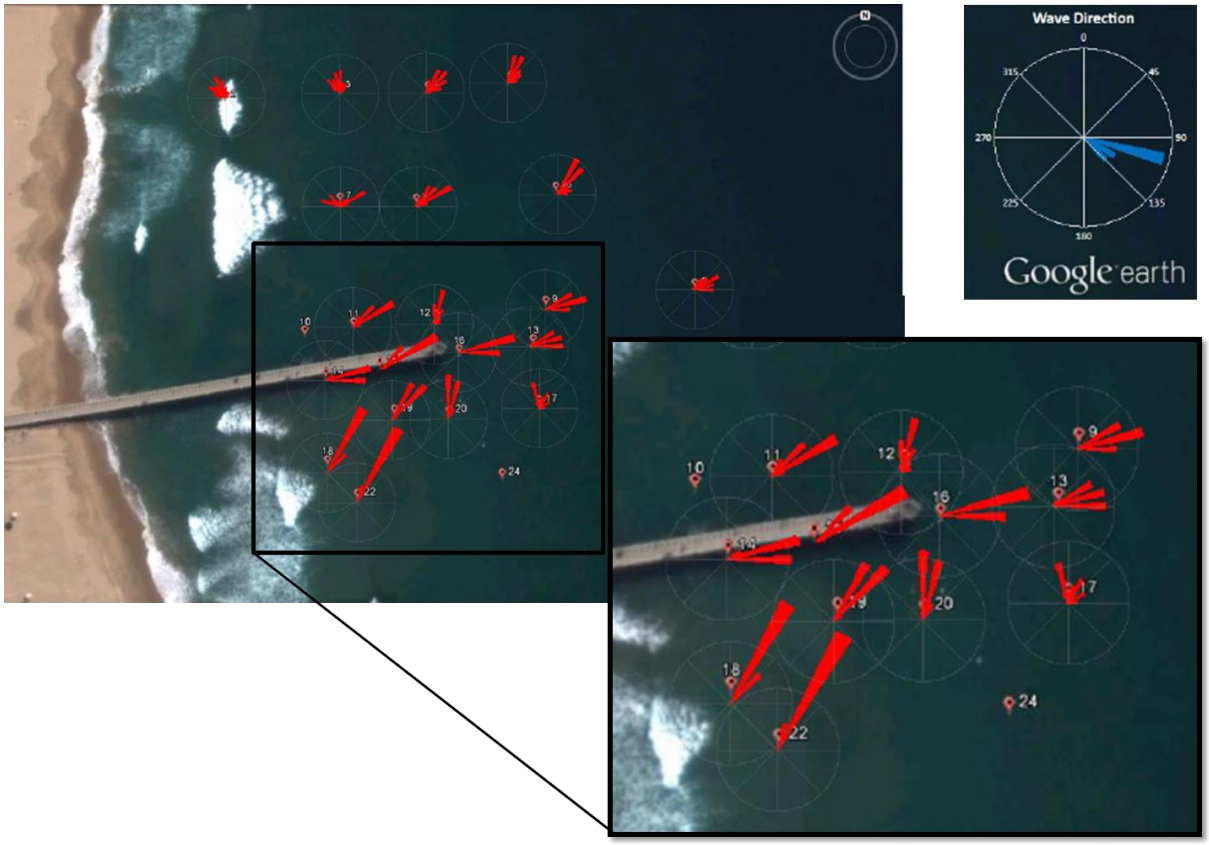

Figure 2-12: Average current roses for 19 current meters deployed in the vicinity of Bay of Plenty and wave rose (top right). The zoomed in image show a cross shore dominant current direction as detected by the current meters. It is noted that wave rose and current rose are dissimilar in showing direction. Wave rose depict wave direction from an angle where the waves propagate from, while current rose show current direction to the angle of propagation (adapted from Lucca, 2013)

Lucca, (2013) further collected 7 sediment samples around the Bay of Plenty groyne: three samples on both side of the groyne and one seaward of the groyne tip. The purpose of collecting the samples was to provide input for a sediment transport model around the groyne. Sieve analysis (as per ASTM D 422) to determine grain sizes and distribution within the vicinity of the groyne was conducted. The assessment considered bed transport due to current, transport due to waves and a combination of the two. Soulsby and Clarke, (2005) method was used to determine shear stress due to waves and currents. The reader is referred to Lucca, (2013) for other methods considered in the study and detail description of the findings. The study found that bed motion around the groyne gets induced when the orbital wave velocity was between 0.2-0.3 m/s.

Ballard's (1991) study showed that an increase in wave activity can results in an increase in erosion and scouring. Lucca and Pattiaratchi's studies showed that an increase in the wave parameters (i.e.

wavelength and significant wave height) results in an increase in current intensity which may result in scouring around a groyne.

Sumer and Fredsoe, (1996) investigated the effect of the near-bed flow patterns and bed shear stress around the vertical breakwater towards the head. The findings showed that scouring process of coastal structures such as piles and breakwaters is mainly due to separation vortices. The study described vortices as major flows that are responsible for local scouring around coastal structures. Permeable groynes typically constructed from concrete or wooden piles can experience similar scouring failure to that of breakwaters.

2.7 Summary

Previous studies on groynes address advantages and disadvantages of both types of groynes; however they do not provide a comprehensive answer regarding how the flow patterns around impermeable groynes are affected by wave conditions and groyne spacing.

- Trampenau, *et al*., (2004) found that impermeable groyne field results in bigger eddy circulation and gravity currents between the groynes. This finding relates to the impact of impermeable groynes on flow patterns and broadened understanding of sediment deposition on the lee side of a groyne (accretion) and the saw-tooth effect on impermeable groynes. However, it did not address water quality as a result of the eddy circulation between the groynes.
- Lucca (2013) and Piattiaratchi, *et al*., (2009) explored how wave driven flow patterns on a single groyne are affected by a change in wave and groyne parameters. Their results elucidated the effect of wave conditions on a single groyne, the development of rip currents on both side of a groyne and the effect on sediment movement. However, to the author's knowledge the conditions were never explored on a groyne field and did not explore water quality.

A limited number of studies have explored the effect of groyne spacing on the flow structure in a groyne field and there has been little investigation using modern numerical modelling. Consequently uncertainties regarding proper spacing of groynes in a groyne field still exist. Suitable spacing of groynes in a groyne field depends on a number of factors. However equal spacing between multiple groynes is common (Castelle *et al*., 2006).

- Studies such as Castelle *et al*., (2006) and Zanuttigh *et al*., (2005) generally recommend groyne spacing between 1.5 to 3 times the groyne length.
- Ballard (1991) recommends a variable spacing such that the flow pattern passing around a groyne structure intersects the next groyne before intersecting with the shoreline to limit the effect of erosion and accretion.
- Trampenau *et al*., (2004) suggests a maximum admissible groyne spacing of up to 5 times the groyne length.

The varying conclusions regarding the effect of groyne spacing on flow patterns further suggests a knowledge gap that needs to be addressed. The study described in this dissertation aims to explore this phenomenon and provide conclusive results by using a numerical model.

The addition of groynes in a groyne field can be beneficial, however our understanding of flow patterns needs to be enhanced for better design and placement of groynes. A number of studies recommend permeable groyne due to their successful applications, studies such as Poff *et al*., (2004) are one example of a successful application of permeable groynes suggesting that the addition of groynes can have a beneficial effect.

3. METHODOLOGY

Chapter three discusses the methodology used in setting up and running a MIKE 21 numerical model of the hydrodynamics analyzed in this study. A general description of the model and simulation methodology is discussed. The reasoning behind the key parameters investigated is elaborated on.

3.1 Numerical modelling

3.1.1 Introduction

Numerous methods have been developed in the study of groynes with physical studies widely used until recently (Walker *et al*., 1991). Physical model studies such as laboratory experiments and field studies can be costly. Advancements in numerical modelling have enabled more useful, less time-consuming research on the subject of coastal hydrodynamics. Walker *et al*., (1991) states that one of the earliest studies on groynes using numerical modelling was conducted by Fleming and Hunt, in 1976. Two dimensional numerical modelling of that time was a process of using sub-models in solving each aspect of hydrodynamics and sediment transport. This paved a way for a better and more reliable numerical modelling that exists today.

A basic approach using two dimensional numerical modelling was adopted to address both of the research questions for this study. Numerical modelling was the preferred option compared to physical studies due of its flexibility, cost and accessibility.

3.1.2 Overview

The DHI MIKE 21 software solves the depth averaged Navier Stokes equations and has been widely used and calibrated for hydrodynamics studies (e.g. Pattiaratchi *et al*., 2009; Broker *et al*., 2003; Duan & Nanda, 2006; Zanittigh *et al*., 2005; Johnson *et al*., 2005).

Three modules of MIKE 21 were used in this study: Mike Mesh Generator, MIKE 21 Spectral Wave (SW) and MIKE 21 flow model (HD). A flexible (unstructured) mesh was used with an idealized bathymetry. The true bathymetry of the study area was not available at the time of the study. A constant beach slope was used in computing the bathymetry. The results from the Spectral Wave were used in the HD flow model.

3.1.3 Mike Mesh Generator

Mike Mesh Generator is a tool/module used to generate and handle unstructured meshes in 2D, including the definition and editing of boundaries (DHI, 2012c). A mesh generator generates

bathymetries in a flexible mesh using specified bathymetry data. The bathymetry was specified using an idealized beach slope and three impermeable groynes equal spaced apart.

3.1.4 Spectral Wave Model

The Spectral Wave (MIKE 21 SW) model is a model used to assess wave conditions in offshore and coastal areas. It is applicable for wave condition prediction and analysis on the regional, local and global scale. Its module is based on the wave action balance equation. The module requires a suitable mesh and bathymetry emulating actual conditions for reliable results (DHI, 2012b).

3.1.5 Hydrodynamic Flow Model

The hydrodynamic (MIKE 21 HD) module is based on a flexible mesh approach applicable within coastal, oceanographic and estuarine environments. It is also based on the numerical solutions of two dimensional shallow water equations and the depth-integrated incompressible Reynolds averaged Navier-Stokes equations (DHI, 2012a).

3.2 Durban Beach Profile

Durban beach experiences powerful hydrodynamic wave conditions particularly during storm conditions. This can be attributed to frequent cold fronts and storm surges that persist in the area. The sediment in the area gets stirred up by breaking waves and transported along the shore. In the computation of a flexible mesh, a beach slope of 1/50 was used. The beach slope was deduced from beach slope data gathered from existing bathymetry of the area obtained from Lucca, 2013. The nearshore slope was found to be 1/50 and the seaward slope from the groyne tip was found to be 1/30 (refer to Figure 3-1). The nearshore beach slope was adapted and made constant throughout the bathymetry. This was done because the nearshore was the main area of interest.

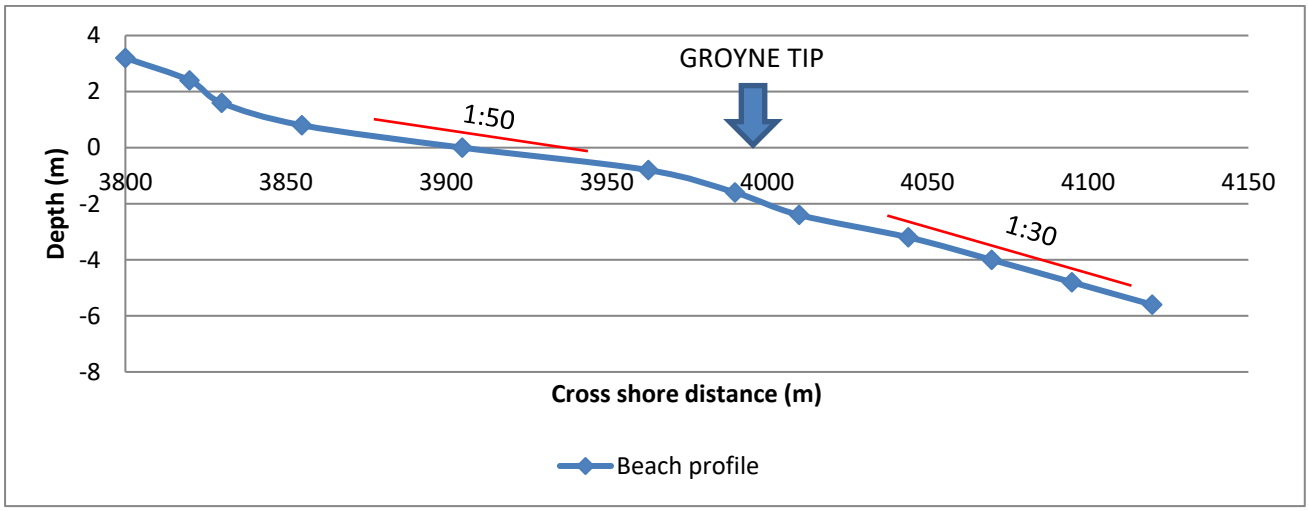

Figure 3-1: Durban beach profile plotted from bathymetry data adapted from (Lucca, 2013) Figure 1.4.

3.3 Breaker zone

The breaker width was used in this study to delineate the region where the majority of waves break. This width was also used to explore the flow constriction within a groyne field. The width of the breaker zone B_z is defined as the distance from a shoreline to the peak gradient in the radiation stress. This means that for a given wave condition the breaker width was constant. The peak gradient in the radiation stress was obtained from the spectral wave model as depicted by Figure 3-2.

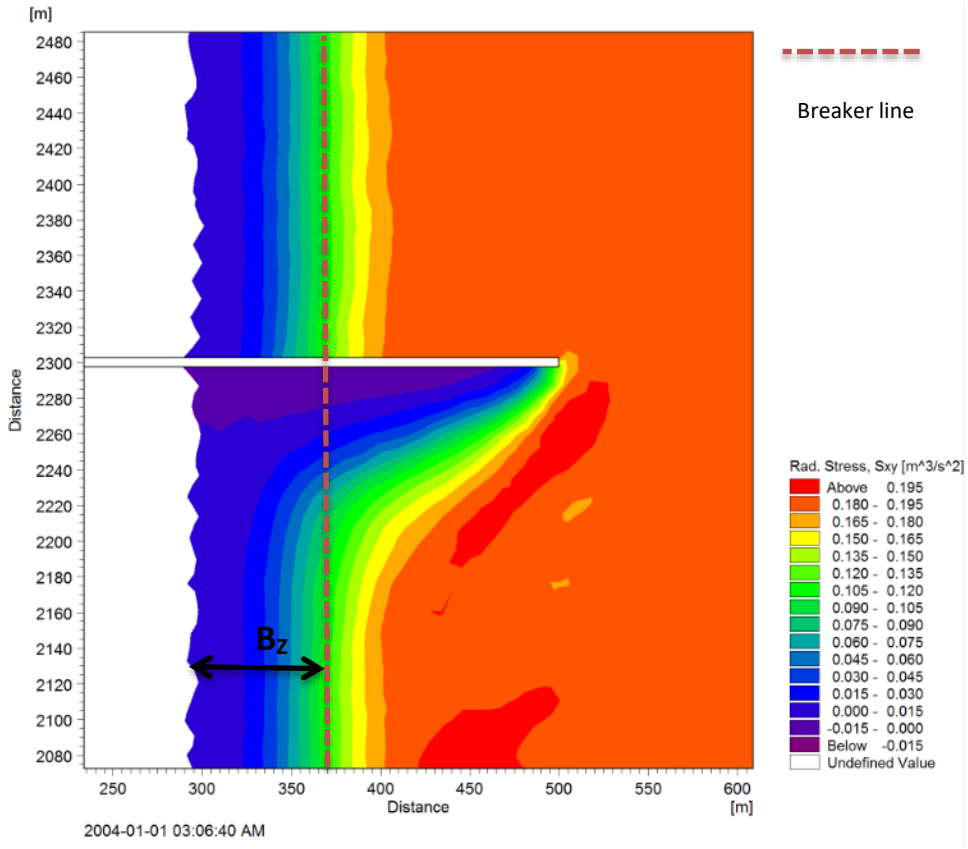

Figure 3-2: Breaker width/breaker zone measurement from a spectral wave model

3.4 Simulation Methodology

3.4.1 Simulation overview

Individual wave parameters were varied alongside water levels in numerical simulations to elucidate the driving parameters for different flow structures within the impermeable groyne field. The Lucca (2013) study showed that variations in prevailing wave conditions impact groyne performance in terms of resulting flow patterns and bed sediment motion.

The following parameters were varied as follows;

- Mean water level
- Significant wave height

- Incident wave angle
- Groyne interspacing and
- Storm conditions

3.4.2 Significant wave heights

Significant wave heights ranged from 1 – 3 m for normal conditions and 3.5 m for storm conditions. The variation affects the breaker zone width and effectively increased or decreased the flow constriction and current intensity within a groyne field. As the significant wave height increases the breaker width increases because larger waves break in deeper water.

3.4.3 Mean Water level

The mean water level was varied in all simulations with the simulation datum kept at 0 m (MIKE 21 default value) for both the spectral wave and hydrodynamic model. The water level was varied from 1 m above to 1 m below the model datum to simulate Durban's spring tide variation. Tide conditions were presented indirectly by varying the domain fixed water level to investigate resulting effects on flow patterns and current speed.

3.4.4 Incident wave angle

The incident wave angle was varied from $30^0/150^0$, $45^0/135^0$ and $60^0/120^0$. The shore line was idealized to be straight which gave the model the flexibility for establishing the flow from south or north direction. The analysis showed that the incident wave angle affects the breaker width and its position, ultimately affecting flow characteristics.

3.4.5 Groyne interspacing

The groyne spacing for this study was varied from 200 to 600 m for spacing of between 0.8 – 4 times the groyne length, respectively. Varying groyne spacing allowed this study to characterize individual and collective groyne performance with respect to flow characteristics.

3.4.6 Storm condition

Corbella & Stretch, (2012b) found that for the coast of Durban the threshold for storm-driven beach erosion is when significant wave heights exceed 3.5 m. Storm conditions were modelled to explore the flow patterns, current speeds and implications on sediment movements. The water level was varied in all storm condition simulations to describe flow characteristics under variable tide conditions.

3.5 Model configuration

The model parameters of a single groyne used in this study were obtained from Lucca (2013). A "spin up" period was allowed for all simulations. The simulations were run for more than 3 hours to establish a quasi-steady state.

3.5.1 Flexible mesh model parameters

The bathymetry was idealized with a constant slope and a straight shore line. Table 3-1 below summarizes groyne and near shore parameters used:

Table 3-1: A summary of beach and groyne standard features

Beach/groyne features	
Nearshore slope	1/50
Groyne length	200 m
Groyne width	5 m
Bathymetry domain	4000 m x 1500 m
Central groyne	2000 m alongshore direction
Top groyne (Bay of Plenty)	Groyne C
Middle groyne (North Beach groyne)	Groyne B
Bottom groyne (Dairy Beach groyne)	Groyne A

The standard mesh parameters are as follows:

- Constant bathymetry beach slope of 1/50. The actual beach slope varies to a steeper slope seaward and away from the groynes (as depicted on Figure 3-1).
- Constant groyne length of 200m and 5m width at zero datum (MWL = 0).
- Bathymetry domain is 4000m x 1500m. 4km alongshore and 1.5km cross-shore direction
- Three groynes in each domain equidistant apart. The middle groyne was placed centrally in the domain in the alongshore direction.
- The land boundary was set up further inland from the swash-zone to allow for an open boundary with run-up and run-down in all simulations. Lucca (2013) found that using a closed boundary instead of an open boundary at the beach affects the rate of wave energy dissipation. The open boundary system experiences more wave energy dissipation than a closed boundary due to bottom friction in the spectral wave model.
- An impermeable boundary was applied around the perimeter of all groynes to make the groynes impermeable.
- The flexible meshes were generated, smoothed, interpolated and refined using the triangulation method as per the MIKE ZERO mesh generator manual.

- Higher mesh resolution was used near the shore to achieve better accuracy there since it was the main area of interest.
- The mesh was subdivided into 7 polygons where the mesh areas varied from (starting at the shore) 100m^2, 200m^2, 400m^2, 900m^2, 1600m^2, 3200m^2 and to 6400m^2 furthest off-shore.
- A total of 7 mesh files were computed consisting of different groyne spacings (200m, 250m, 300m, 350m, 400m, 500m and 600m).
- The flexible meshes were generated, smoothed, interpolated and refined using the triangulation method given in the MIKE ZERO mesh generator manual.

The groyne layout and groyne names used are shown in Figure 3-3, which defines some of the terms used in the results section e.g. Area 1, Area 2, Groyne A, etc.

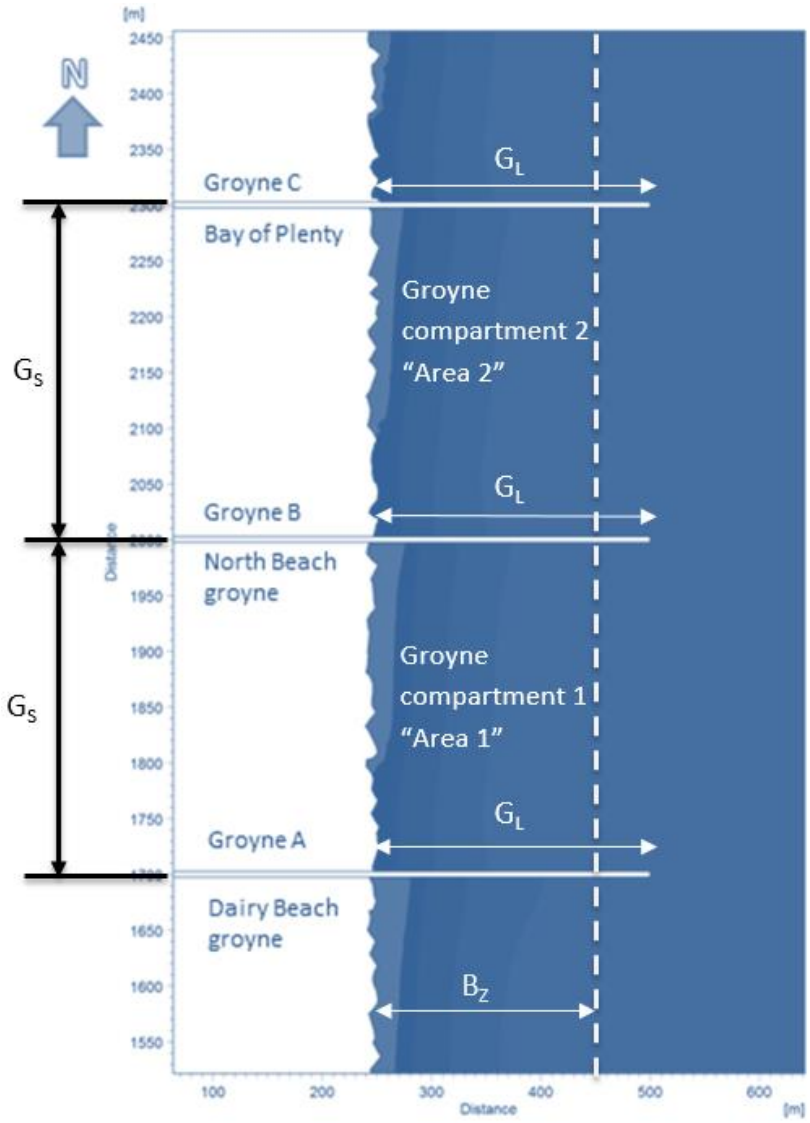

Figure 3-3: Durban beach groyne layout bathymetry showing the position of the groynes according to site layout for the purpose of the study.

3.5.2 Spectral wave model parameters

The Spectral Wave model uses an unstructured/flexible mesh when simulating the growth, decay and transformation of wind generated waves and swells in offshore and coastal areas (DHI, 2012b). Ric *et al*., 1994 states that spectral wave model allows for efficient representation of the generation and dissipation of random short crested waves due to high spatial resolution inputs and numerical techniques. The model inputs are as follows:

- Two different formulations, namely directionally decoupled parametric formulation and fully spectral formulation can be used (DHI, 2012b). The directional decoupled parametric formulation is based on the parameterization of the wave action conservation equation in accordance with Holthuijsen *et al*., (1989), while the fully spectral formulation is based on the wave action conservation equation described in Komen *et al*., (1994) and Young, (1999). The dependent variable in this formulation is the directional-frequency wave action spectrum. The fully spectral formulation was used.
- The model domain consisted of a flexible mesh, minimum depth cut off and datum.
- Boundary conditions were specified such that waves propagated from offshore (an open boundary) and were parameterized by an input significant wave height H_S, wave period T_P, wave incident angle Θ and default directional spreading index of 5. The shore parallel open boundary was specified with wave parameters which allowed for the input of wave parameters. The shore was specified to land boundary and the shore normal boundaries were specified to be lateral boundaries.
- The model applied wave breaking formulas derived by Battjes & Janssen (1978). Studies such as Dean & Dalrymple, (2004) and Sabatier, (2006) recommend a breaker index value of 0.78 as a first estimate but note that the value can vary from 0.4 to 1.2. Ric *et al*., 1994 used a breaker index of 0.73, an average obtained from field experiments done by Battjes and Stive, (1985). Previous model studies of groynes (i.e. Pattiaratchi *et al*., 2009; Lucca, 2013) used 0.8 as the breaker index value while studies such as Dean & Dalrymple, (2004) and Sabatier (2006) recommend using 0.78 as the first estimate for engineering applications. Since the study was a continuation of the Lucca (2013) study, 0.8 was used for this study.
- The model simulates diffraction using a phase decoupling refraction approximation proposed by Holthuijsen *et al*., (2003). The approximation is based on the mild slope equation for refraction and diffraction, and omits phase information. Model standard default values with a smoothing factor of 1 and smoothing steps of 1 were used.
- The model specifies five different options for bottom friction. For this study, the bottom friction used was Nikuradse roughness parameter k_N of 0.04m which was set to be constant in the domain. Bottom friction for a sandy bottom is said to be determined by two parameters which

are a normalized bottom roughness and a parameter that represents the capacity for the waves to induce bottom motion described in detail by Holthuijsen *et al*., (2007).

- Model exclusions: Ice coverage, wind forcing, structures, water level and current conditions were excluded from the simulations because the study focused on the wave driven current.

3.5.3 Hydrodynamic model parameters

The MIKE 21 hydrodynamic flow module is also based on the use of the flexible mash approach with the input of the spectral wave results.

- The bathymetry described in section 3.5.1 was used for this module.
- The datum used for the spectral wave module was applied.
- A simulation period of 1600 time steps at 7 seconds intervals was applied. The time step for the hydrodynamic calculations is synchronized at the time step for the advection/dispersion calculations (DHI, 2012a).
- The simulation time period and accuracy are controlled by specifying one of two numerical schemes: the lower order (faster but less accurate) or the higher order scheme (slower but more accurate). The process is dominated by convection (flow), then higher order space and time discretization should be used. The higher order numerical solver was used for the shallow water equations in this study and the Courant-Friedrich-Levy (CFL) number was kept below 0.8 (default value).
- The flooding and drying option was set to default values which was 0.005m for drying depth, flooding depth 0.05m and wetting depth 0.1m.
- The model's recommended value for the Smagorinsky coefficient (C_S) used was for the eddy viscosity
- Wind forcing was excluded from both Spectral wave and Hydrodynamic simulations as the study focused on waves.
- MIKE 21 Spectral wave output files were used as input to the hydrodynamic module for the radiation stress results (S_{XX}, S_{XY} and S_{YY}).

3.5.4 Model discussion

All simulations were based on an idealized impermeable groyne field with a uniform beach slope. This study explored the effect of multiple groyne fields, acting as a unit and the effect of groyne spacing on flow characteristics.

Several parameters were varied for reasons discussed below:

- Water level was varied in all simulations to ascertain the effect of water variations on the overall groyne field. Fixed water level was changed for all simulation by means of increase or decrease in the water level. This was done to incorporate tide changes as they were not incorporated

directly from the model. It was found that water level variations directly affect the groyne length in active water and offshore breaker width position for a single impermeable groyne. The eddy circulation and current speeds showed significant change with variation in water level which are discussed in detail in the next section.

- Significant wave heights were varied for the same reason as the water levels. Increasing the significant wave heights resulted in an increase in the current speed around a groyne and associated flow patterns presented in section 4. Changing the significant wave height and the water level affected the flow constriction and provided a more complex eddy circulation pattern structure. Results from Lucca, (2013) for a single impermeable groyne, indicated that variation of the significant wave height may increase the current speed causing it to strengthen in the cross-shore direction, with strong rip currents alongside the groyne.
- The wave incident angle was varied three times per simulation. Lucca (2013) found that wave incident angle plays a role in the current characteristics and eddy circulation. The increase in the wave incident angle results in an increase in current speed thus increasing the rip current experienced by the groynes.
- Groyne spacing is an integral part of groyne design. Over estimating or under estimating the spacing may result in groyne structures being ineffective and negatively affect the coastline. The effectiveness of a groyne depends on its ability to retain littoral transport and resist the alongshore current. The groyne spacing for this study range from 0.8 – 4 times the groyne length/span.

3.6 Numerical model compared to field data

Lucca (2013) carried out field measurements of current velocities around the Bay of Plenty groyne. Field measurements were done using a propeller type directional current meters. The results from the current meter were not depth averaged while the model was depth and phase averaged. Lucca's results were averaged over ten minutes.

The data was recorded for 24 hours which included both high and low tide. The following additional geometric parameters were used for the model simulations:

- Bathymetry domain of 4000 m alongshore x 1500 m cross-shore.
- Simplified constant beach slope of 1/50 for modelling purposes. The actual beach slope has a steeper slope seaward of the groyne tips. (As depicted on Figure 3-1).
- Groyne interspacing of 300 m.
- Significant wave height of 1.4 m, wave period of 9.05 seconds and incident wave angle of 116^0.
- Tide condition of 1.5 m CD (chart datum) for high tide and 0.9 m CD for low tide. These corresponded to the actual tide conditions during the field experiments.

3.7 Dimensional Analysis

The results are further represented by the use of non-dimensional scaling and plotted in sections. This is done to universally present the groyne tip velocity and the direction for better appreciation and limitation of local scour on groyne tip. The dimensional analysis was conducted as follows:

- The groyne tip velocity u and the v components obtained from the numerical model results was used to obtain the velocity magnitude (|Vtip|).
- The velocity data was non-dimensionalized by dividing H_S/T_P

The velocity was scaled using H_S/T_P in line with Snell's law. The law as presented by Bosboom &Stive, (2012) in chapter 5.5 reads as follows:

The alongshore component driving force is as a result of the radiation stress S_{xy} as previously noted by Longuet-Higgins & Stewart (1964) and Reeve, *et al*. (2004). The driving force (F_Y) can be expressed as follows:

$$F_Y = -{dS_{xy}}/{dx} = -\frac{\sin\theta}{c}\frac{d}{dx}EC_g\cos\theta \qquad \text{(Snell's law)} \qquad (3\text{-}1)$$

where c is the wave celerity, E is the wave energy, θ is the wave direction and C_g is the wave group celerity.

The alongshore driving force occurs when the waves are breaking and it is a function of the dissipation of wave energy within the surf zone. The driving force is countered by bed shear stress that develop as a result of waves breaking to restore equilibrium. The bed shear stress ($\tau_{b,y}$) can be expressed as follows:

$$\tau_{b,y} = \frac{1}{\pi}\rho c_f\sqrt{gh(x)}\frac{H}{h(x)}V(x) \qquad (3\text{-}2)$$

where ρ is the density, $c_f$is the friction coefficient, H is the wave height, $h(x)$ is the water depth and $V(x)$ is the depth averaged alongshore current velocity. Therefore equating 3-1 and 3-2 gives the depth averaged velocity and can be expressed as follows:

$$V(x) = -\frac{5}{16}\pi\frac{\gamma}{c_f}g\frac{\sin\theta}{c_0}h(x)\frac{dh}{dx} \qquad (3\text{-}3)$$

for constant beach slope $\tan\alpha = -\frac{dh}{dx}$ and $\gamma = H_0/h(x)$. The current velocity is proportional to the depth and peaks at the breaker line. Therefore $h(x) = h_b$

$$V(x) = \frac{5}{16}\pi\frac{H_0}{c_f}g\frac{\sin\theta}{c_0}\frac{h}{h_b}\tan\alpha \qquad (3\text{-}4)$$

where α is the beach angle, $c_0 = \frac{gT_0}{2\pi}$ is the deep water group celerity and T_0 is the deep water wave period. Therefore the equation (3-4) can be simplified and expressed as follows:

$$\frac{V(x)}{H_0/T_0} = \frac{10}{16}\pi^2 \sin\theta \frac{h}{h_b} \tan\alpha \qquad (3\text{-}5)$$

Therefore the deduction that can be made from Snell's law is $V(\max)$ is proportional to H_0, h_b is proportional to H_0, B_Z is proportional to H_0 and Q is proportional to $(V(\max), h_b, B_Z)$.

- The non-dimensional $|Vtip|/(H_S/T_P)$ ratio was plotted against the flow constriction G_L/B_Z to evaluate the relationship that exist between the two ratios.
- The groyne tip velocity direction or angle (β) was obtained using groyne tip velocity components (arctan u/v).
- The velocity direction was then plotted with the flow constriction.

3.8 Residence time computation

The residence time is defined as an average time a water parcel resides within a groyne compartment until it escapes. It was computed using fresh water method described in the literature review and represented by $T_r = V_{vol}/Q_0$ (equation 2-5) where V_{vol} is the volume of water in a compartment between two groynes and Q_0 is the total inflow in a groyne compartment.

The water volume in a groyne compartment was computed by using mean water level due to uneven water surface elevation. The inflow and outflow was measured using MIKE 21 hydrodynamic line measurement alongshore through the groyne tips and the inflow (P-flux) was summed. Using the outflow would have yielded similar results as the system was in equilibrium. The impermeable groynes forced the flow to enter and escape between the two groynes in the field thus allowing for comprehensive measurements. Semi-permeable or permeable groynes would have posed a challenge on gathering such data accurately due to the flow able to pass through the groynes.

4. RESULTS AND DISCUSSION

Chapter Four presents and discusses an analysis of current dynamics within a groyne field. Wave parameters including significant wave height, mean sea level and incident wave angle have been varied. Spatial properties such as groyne spacing have also been varied. Together these results provide a comprehensive description of flow fields associated with possible groyne field configurations and metocean conditions. Finally, recommended design conditions are discussed based on the observations made.

Outline

This section explores how flow structure responds to varying conditions within a groyne field. The section is structured as follows;

Section 4.1 compares field measurements obtained by Lucca (2013) to modelled results using similar wave conditions. Due to the unavailability of the true site bathymetry some aspects (i.e. uniform beach slope, impermeable groynes, etc.) of the analysis was simplified.

Section 4.2 evaluates the relationship between peak gradients in the radiation stress (the breaker zone B_Z), the flow constriction (G_L/B_Z), groyne spacing, groyne tip velocities and direction. The evaluation is conducted by varying the following wave parameters:

- Significant wave heights (H_S)
- Mean water level (MWL)
- Incident wave angle (θ)

Section 4.4 discusses storm events.

Section 4.5 discusses synthesis through dimensional analysis where by the various parameters (i.e. G_L/B_Z, G_S/G_L, groyne tip velocities and direction) are plotted to generalize the results.

Section 4.6 discusses possible implications on water quality.

Note: The ranges of incident wave angles used throughout the models (excluding section 4.1) are 30^0 or 150^0, 45^0 or 135^0 and 60^0 or 120^0. Waves were generated from the model southern or northern boundary.

4.1 Numerical model compared to field data

Lucca's field results (see section 2.6) were used to compare flow field measurements to modelled results using similar wave parameters. However, there are limitations to this approach: certain model parameters (e.g. the idealized bathymetry with constant beach slope and straight shoreline, assumed impermeable groynes, etc.) are not accurate representations of the field conditions, as discussed in section 3.6. Nevertheless this process was intended as a simplified validation of the numerical model.

4.1.1 Modelled Bay of Plenty

The flow constriction and the groyne spacing to groyne length ratio for this condition are summarized in Table 4-1. The simulation was conducted for similar wave condition to those measured by Lucca (2013), H_S = 1.4 m, T_P = 9.05 s and the incident wave angle was 116°. The water level was varied to simulate the Durban coast line's range of tide levels

Table 4-1: The effect of varying surface water levels on the breaker width, flow constriction and the current speed for wave condition $H_s = 1.4\ m$; $T_p = 9.05\ s$; $\theta = 116^0$; $G_S = 300\ m$

Water level (m)	B_Z (m)	G_L (m)	G_L/B_Z	G_S/G_L	Groyne tip current velocities for BOP groyne (m/s)				
					u velocity	v velocity	|Vtip| (m/s)	(|Vtip|)/(H_S/T_P)	β(^{0})
1.5	90	275	3.056	1.091	0.274	0.084	0.287	1.853	73
0.9	93	245	2.634	1.224	0.295	0.093	0.309	1.999	73

Figure 4-1 shows the flow patterns for 1.5 m water level condition. The flow patterns shows rip current on both sides of the groynes due to the position of the breaker zone closer to the shore. This is consistent with Lucca's (2013) observation. Furthermore, groyne compartments show circulation zones formed due to eddy recirculation. The flow constriction and G_S/G_L was found to be 3.056 and 1.091 respectively. The groyne tip velocity magnitude was 0.287 m/s. The high flow constriction resulted in the current speed highest towards the groyne mid-span.

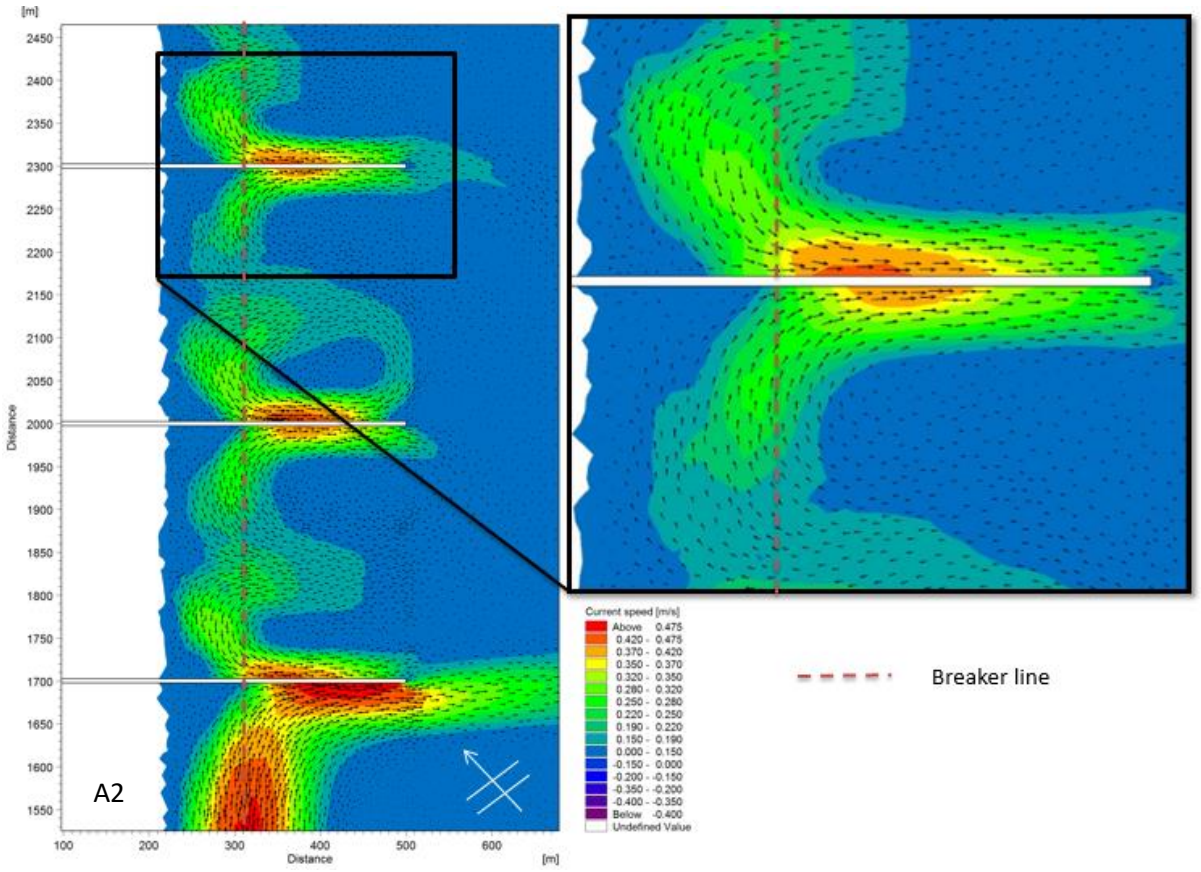

Figure 4-1: Modelled current speed vector plot for Water level = 1.5 m. The results reveal how alongshore current is resisted by the groynes, and as a result rip current and eddy circulation develop between the groynes. The Bay of Plenty groyne (magnified image) experienced the greatest peak rip current toward the mid span high tide and wave conditions. (Model run A2)

The low water level significantly reduced the flow constriction from 3.056 to 2.634. The groyne tip velocity magnitude was 0.309 m/s. A 0.022 m/s increase in the groyne tip velocity magnitude from the previous condition. Eddy circulations were observed on the upstream side of the groynes (similar to the high water level condition), and were observed to recirculate within the groyne compartment (refer to Figure 4-2).

The flow structure remained relatively unchanged for both high and low tide conditions. The peak current speed was observed to occur on groyne A for both water level conditions. The current was deflected cross shore on groyne A resulting in strong rip current. For low water level condition, the peak current speed occurred closer to the groyne tip.

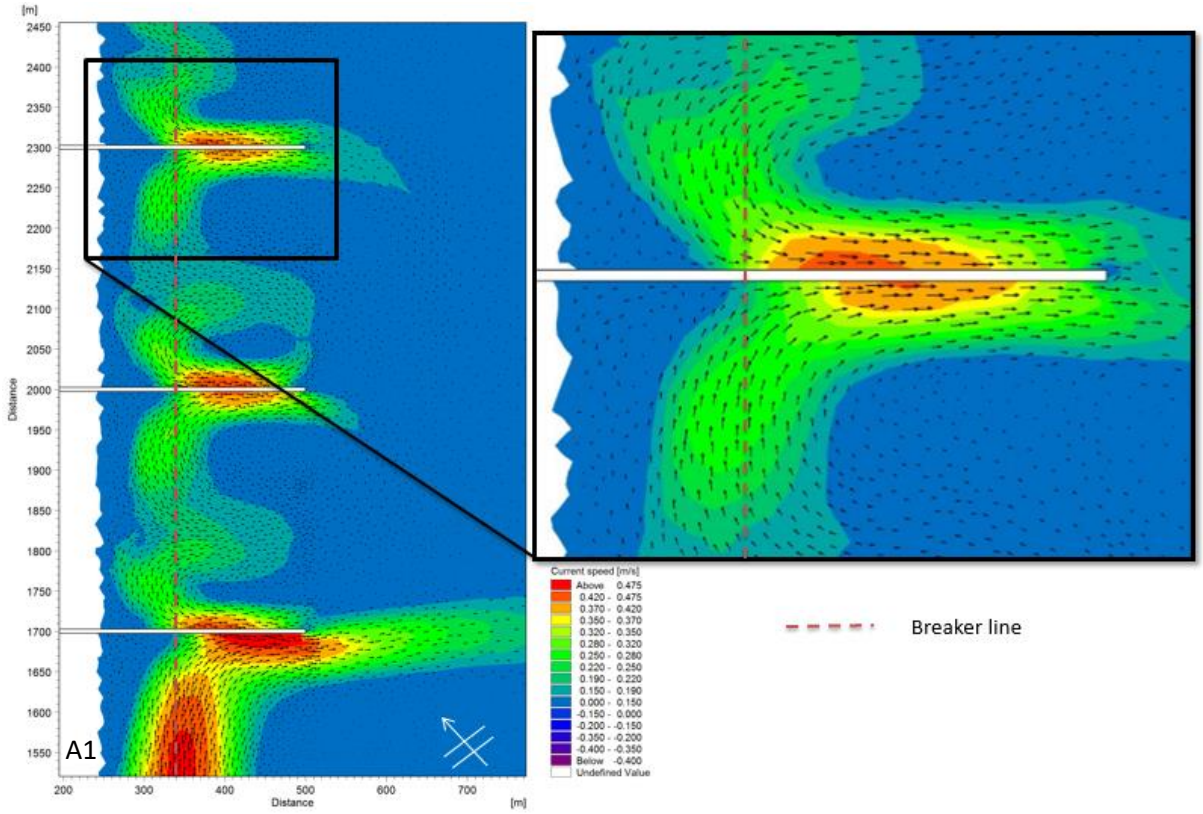

Figure 4-2: Modelled current speed vector plot for Water level = 0.9 m. The results reveal how alongshore current is resisted by the groynes, and as a result rip current and eddy circulation develop between the groynes. The Bay of Plenty groyne (magnified image) experienced the greatest peak rip current toward the midspan high tide and wave conditions. (Model run A1)

4.1.1 Bay of Plenty Model findings summary

Although there are noticeable differences between modelled and field conditions (i.e. groyne impermeability, bathymetry idealizations, etc.), this study's modelled Bay of Plenty flow structure was observed to be consistent with Lucca's field measurements (see Figure 2-12). Both show a predominantly cross shore current on both sides of BOP groyne. Pattiaratchi *et al*., (2009) found similar flow patterns to develop for impermeable groyne using Lagrangian measurement methods and their field observations were consistent with those of Trampenau *et al*., (2004), who found that rip current formation is common for impermeable groyne structures.

Lucca, (2013) observed relatively stronger current speeds during high tide compared to low tide conditions. His field measurements showed strongest current speeds of 0.475 m/s on the upstream, mid-span groyne section during high tide, and 0.365 m/s during low tide.

The modelled current speeds and the midspan groyne position on the upstream side are consistent with Lucca's field measurements. However, there are inconsistencies regarding the maximum current speed on the two sides of the groyne which occurs on the downdrift side of the groyne in the model

simulations. The inconsistency may be attributed to the sheltering effect of the two groynes upstream in the simulations. The sheltering effect introduced by upstream impermeable groynes can affect rip current formation. Trampenau *et al*., (2004) showed this by varying groyne permeability in his study and found that for low permeability (i.e. $P \leq 10\%$), rip currents associated with leeward side eddy circulations form between the groynes (see Figure 2-9).

The other inconsistency observed was regarding the current speed in front of the groyne tip. Field measurements observed an average rip current speed of 0.475 m/s for high tide conditions whereas the modelled results showed an average speed of 0.220 m/s. The lower model current speeds may be attributed to higher resistance of the modelled impermeable groynes compared to the semi-permeable field groynes, and the fact that the actual BOP groyne is exposed more than the other two upstream groynes due to the sheltering provided by the harbor entrance breakwater.

The average current speed results for low tide conditions were found to be consistent for both sets of results: Field measured average current speed for the reduced water level (water level = 0.9 m) was found to be 0.365 m/s towards the groyne tip, similar to the modelled result of 0.370 m/s (Model Run A1). However, the modelled results still showed the absolute peak current speed to occur on the down drift side of the groyne in contrast to the field results.

4.1.2 Conclusion

This study's groyne field model was idealized as consisting of impermeable groynes, but for low water levels, field measurements were comparable to modelled results. This suggests that the groynes along the Durban coast behave more as impermeable rather than permeable groynes when the water levels are low. Modelled flow structure and peak velocity were consistent with field measurements. However, some inconsistencies were observed. The inconsistencies relate to the occurrence of peak current speeds on the groyne sides and the current speeds in front of the groyne tip. These inconsistencies may be due to (1) the sheltering effects provided by the upstream groynes, (2) the sheltering effects of the Southern breakwater at the harbor entrance, and (3) the permeability difference between the modelled and field groynes.

Trampenau *et al*., (2004) showed that permeable groynes exhibit low resistance to alongshore current, and is therefore expected to experience predominantly alongshore current. The Durban groynes were constructed with reinforced concrete piles and rocks placed between the piles. It is therefore expected that the groynes will be predominantly impermeable at low tide due to the rock infill, but less so at high tide. The flow structure consistency between the two sets of results is evidence that the Durban groynes have low permeability (particularly at low tide), explaining the strong rip currents observed for both sets of results.

4.2 Peak gradient of radiation stress

The results presented in this section include the peak gradient of the radiation stress components used to measure the breaker width from the model results and the flow constriction ratio (G_L /B_Z). The groyne spacing was kept constant at 300m for all simulations in this section. The effect of varied wave parameters was explored to elucidate the effect on the flow patterns presented in section 4.3.

4.2.1 Significant wave height variation

The significant wave height was varied from 1m to 3 m to elucidate the effect on the cross-sectional flow constriction. Significant wave height was kept below 3.5 m as 3.5m was considered to correspond to storm conditions, which are addressed in section 4.4. Table 4-2 summarizes the findings of the effect of significant wave height variation breaker zone width, radiation stress components and flow constriction ratio.

Table 4-2: The effect of significant wave height variation on breaker zone width for wave condition H_s *= 1 m;* T_p *= 14 s;* $\theta = 45^0$; *MWL* = 0; G_S = 300m.

H_S (m)	B_Z (m)	Peak S_{XX} (m^3/s^2)	Peak S_{XY} (m^3/s^2)	Peak S_{YY} (m^3/s^2)	G_L /B_Z	G_S/G_L
1	90	1.120	0.195	0.520	2.222	1.500
2	150	3.500	0.720	1.800	1.333	1.500
3	220	6.500	1.500	3.500	0.909	1.500

An increase in significant wave height from 1 to 2 m (all other wave parameters remaining constant) resulted in the breaker zone width increasing from 90 to 150 m and a reduction in the G_L /B_Z ratio from 2.222 to 1.333. The breaker zone moved offshore and the radiation stress components were seen to increase. Despite the offshore movement of the breaker zone width, waves were observed to break within the groyne length near the groyne tip.

A significant wave height increase from 2 to 3 m (all other parameters remaining constant) resulted in a similar increase in the radiation stress components. The breaker zone width increased from 150 to 220 m and the position moved beyond the extent of the groyne length. The G_L /B_Z ratio decreased from 1.333 to 0.909.

From the above observations it may be concluded that significant wave height considerably affects the flow constriction in the groyne field. An increase in significant wave height results in the breaker zone width increasing and extending beyond the groyne length for a given wave conditions. Having established from the results that the significant wave height affects the breaker zone width and the flow constriction, section 4.3 explores the overall effect on flow patterns.

4.2.2 Mean water level variation

In this section mean water level (MWL) was varied to elucidate the effect of varying groyne length on the flow constriction, and radiation stress components. It was expected for the variation to directly affect the G_L /B_Z ratio as a result of the groyne length change while the breaker zone width remained constant. The breaker zone width remained unchanged due to a fixed wave height and a constant beach slope. The results for varying MWL for the constant wave condition H_s = 1 m; T_p = 14 s; θ = 45^0, are summarized in Table 4-3.

Table 4-3: The effect of water level variation on radiation stress components for wave condition H_s = 1 m; T_p = 14 s; θ = 45^0/135^0; G_S = 300m

MWL (m)	G_L (m)	Peak S_{XX} (m^3/s^2)	Peak S_{XY} (m^3/s^2)	Peak S_{YY} (m^3/s^2)	B_Z (m)	G_L /B_Z	G_S/G_L
1	250	1.120	0.195	0.520	85	2.941	1.200
0	200	1.120	0.195	0.520	90	2.222	1.500
-1	150	1.040	0.195	0.480	90	1.667	2.000

Varying MWL moved the shoreline nearer or further offshore, but had little effect on the magnitude of the radiation stress components and the breaker zone width as expected. Water level variation directly affects the groyne length in the active water zone thus this exercise is exactly similar to varying groyne length in active water zone. A water level increase from MWL = 0 to 1 m resulted in shoreline retreat landwards by 50 m and an increase in the groyne length in contact with the active water zone. The radiation stress components remained constant. Due to the increase in the effective groyne length, the flow constriction increased accordingly.

The shoreline moved seaward by 50 m as the water level decreased from MWL = 0 to -1 m and the effective groyne length decreased from 200 to 150 m. Although the breaker zone moved further offshore, it remained within the groyne length. The flow constriction reduced from 2.222 to 1.667. The decrease in the effective groyne length and breaker zone width remaining relatively constant resulted in the decrease in the flow constriction.

An increased Hs = 2m was applied to evaluate how the radiation stress components would be affected by water level variation. This was done to evaluate if the previous water level variation findings for significant wave height of 1 m would hold true for higher significant wave height. A summary of the findings for wave condition H_s = 2 m; T_p = 14s; θ = 45^0/135^0 is shown in Table 4-4.

Table 4-4: The effect of water level variation on radiation stress components for wave condition H_s = 2 m; T_p = 14 s; θ = $45^0/135^0$

MWL (m)	G_L (m)	Peak S_{XX} (m^3/s^2)	Peak S_{XY} (m^3/s^2)	Peak S_{YY} (m^3/s^2)	B_Z (m)	G_L /B_Z	G_S/G_L
1	250	3.500	0.780	2.250	150	1.667	1.200
0	200	3.500	0.720	1.800	150	1.333	1.500
-1	150	3.250	0.700	1.650	160	0.939	2.000

The breaker zone width increased from 90 m (Hs = 1 m) to 150 m (Hs = 2 m) and extended more towards the groyne tip for MWL = 1 m. Changes in MWL did not result in a breaker zone width increase however the breaker line moved shoreward. The flow constriction therefore increased from 1.333 to 1.667 due to the increase in effective groyne length.

As the water level reduced from MWL = 0m to MWL = -1m the u velocity component peaked on the upstream side of the groyne towards the groyne tip. The effective groyne length was reduced to 150 m which resulted in the reduction of the flow constriction is from 1.333 to 0.939.

Varying MWL had a significant effect on the location of the breaker zone in relation to the groyne length.

4.2.3 Incident wave angle variation

The incident wave angle was varied to elucidate the impact of varying wave angles on breaker zone width and radiation stress components. The incident wave angle was varied from 30^0 to 150^0. Wave parameters such as significant wave height, wave period and water level were kept constant. A summary of the findings is provided in Table 4-5.

Table 4-5: The effect of incident wave angle variation on radiation stress components for wave condition H_s = 1 m; T_p = 14 s; MWL = 0 m.

Θ (degrees)	Peak S_{XX} (m^3/s^2)	Peak S_{XY} (m^3/s^2)	Peak S_{YY} (m^3/s^2)	B_Z (m)	G_L /B_Z	G_S/G_L
$30^0/150^0$	0.840	0.210	0.400	75	2.667	1.500
$45^0/135^0$	1.120	0.195	0.520	90	2.222	1.500
$60^0/120^0$	1.300	0.195	0.600	100	2.000	1.500

The results above show that varying the incident wave angle affects both the radiation stress components and the breaker zone width. The breaker zone width and the radiation stress components increased with the increase in incident wave angle. All radiation stress components increased except for the alongshore component which reduced. The breaker zone width was located towards the mid span of the groynes for all variations of the incident wave angle.

A similar evaluation was conducted for increased significant wave height of 2 m to evaluate if the incident wave angle variation results for significant wave height of 1m would hold true. The wave condition H_s = 2 m; T_p = 14 s; MWL = 0 m was explored for varied incident wave height. A summary of the finding is provided in Table 4-6:

Table 4-6: The effect of incident wave angle variation on radiation stress components for wave condition H_s = 2 m; T_p = 14 s; MWL = 0 m.

Θ (degrees)	**Peak S_{XX} (m^3/s^2)**	**Peak S_{XY} (m^3/s^2)**	**Peak S_{YY} (m^3/s^2)**	**B_Z (m)**	**G_L /B_Z**
$30^0/150^0$	2.600	0.700	0.400	130	1.538
$45^0/135^0$	3.500	0.720	1.800	150	1.333
$60^0/120^0$	4.000	0.650	2.100	155	1.290

Similar to the results described in Table 4-5, the breaker zone width and the radiation stress components increase with an increase in the incident wave angle, indicating that these variables are dependent on the incident wave angle. It is noted that the S_{XY} component of the radiation stress peaks at an incident wave angle of 45°. Lucca (2013) found similar results for the S_{XY} component at an incident wave angle of 45°. The reason for this finding is not clear. The flow constriction correspondingly reduced with the reduction in the incident wave angle.

4.3 Eddy circulation around multiple groynes

Section 4.2 showed how the breaker zone width and radiation stress components were affected by varying wave parameters, thus enabling the understanding on flow patterns, eddy circulations and circulation zone discussed in this section. For the purpose of this study, circulation zone refers to more than one eddy circulation formation between two groynes and eddy recirculation refers to eddy circulation forming upstream of a groyne. The results are then comprehensively used to elucidate eddy circulation formation, groyne tip velocity magnitude and direction for groynes within the groyne field. The dimensionless parameters are then used to explore how wave parameters and groyne geometric parameters affect the groyne functioning.

4.3.1 Significant wave height variation

In this section significant wave height was varied to elucidate how groyne tip velocity magnitude and direction, eddy circulation and recirculation forms and are affected by the variation. Table 4-7 summarizes the results on the flow constriction, groyne tip velocity magnitude and direction for wave condition T_P = 14 s; $\theta = 45^0/135^0$; MWL = 0 m; G_S/G_L = 1.5 (refer to Figure 3-3 for groyne labelling).

Table 4-7: Effects of varying significant wave height on the flow constriction and groyne tip velocity for wave condition T_p = 14 s; θ = $45^0/135^0$; MWL = 0 m; G_S/G_L = 1.5

H_S (m)	G_L (m)	B_Z (m)	$\frac{G_S}{G_L}$	$\frac{G_L}{B_Z}$	Groyne C			Groyne B			Groyne A		
					|Vtip| (m/s)	$\frac{\|Vtip\|}{H_S/T_P}$	β(^{0})	|Vtip| (m/s)	$\frac{\|Vtip\|}{H_S/T_P}$	β(^{0})	|Vtip| (m/s)	$\frac{\|Vtip\|}{H_S/T_P}$	β(^{0})
1	200	90	1.500	2.222	0.205	2.873	82	0.090	1.255	55	0.145	2.035	74
2	200	150	1.500	1.333	0.833	5.829	47	0.399	2.794	32	0.527	3.688	45
3	200	220	1.500	0.909	1.103	6.094	32	0.779	5.456	4	1.060	4.944	26

The flow pattern for the Hs = 1 m wave condition is depicted in Figure 4-3 (a). The breaker zone line depicted in Figure 4-3 (a) indicate that the breaker zone width located within the groyne length. As a results the level of flow constriction was found to be 2.222. The peak cross shore current velocity component of 0.501 m/s was observed toward the midspan of Groyne C (upstream groyne) on the upstream side and reduced to 0.205 m/s towards the groyne tip. The current velocity direction (β) resembles the flow pattern shown. The peak current velocity magnitude reduced to 0.45 m/s for downstream groyne B and A. However still located towards the groyne midspan. The groyne tip velocities were lower for downstream groynes compared to Groyne C (upstream groyne), Groyne B (central groyne) and A (downstream groyne) experiencing 0.09 m/s and 0.415 m/s respectively.

The flow patterns show stronger current speed occurring on the upstream side of the groynes due to high flow constriction suggesting rip current. The hydrodynamic model predicts eddy circulation formation on the lee side of the groynes and eddy circulation zones between the groynes. Eddy circulation zones were observed to develop between the three groynes due to eddy recirculation. Eddy recirculation was found to develop upstream of groyne B and groyne A due to sheltering effect provided by upstream groyne.

The flow structure for wave condition H_S = 2 m; T_P = 14 s; θ = $45^0/135^0$; MWL = 0 m is shown in Figure 4-3 (b). The flow constriction reduced from 2.222 (B_Z = 90 m) to 1.333 (B_Z = 150 m) due to the increase in H_S and breaker line relocated toward the groyne tip as shown in Figure 4-3 (b). The groyne tip velocity magnitude increased from 0.205 m/s to 0.833 m/s and peaked on the groyne tip as a result. Consequently, larger eddy circulation formed on the lee side of Groyne C and smaller eddies formed on downstream groyne A and B. With the increased significant wave height, the eddy recirculation effect appears to have disappeared. The groyne tip velocity was higher for Groyne C compared to downstream groynes, similar to the previous wave condition. The water surface elevation was observed to increase, particularly upstream of all the groynes and lower downstream. It may be concluded that increased significant wave heights results in a greater differential water surface elevation between the groynes which may result in gravity current noted by Trampaneu *et al*., (2004).

The groyne tip velocity suggests higher values for lower levels of flow constriction. The groyne tip current direction is also noted to be more towards 45^0 suggesting predominantly alongshore current direction. Figure 4-3 (b) is in strong alignment with the results. The flow constriction reduced with the increase in significant wave height resulting in overall increase in the groyne tip velocities.

The flow pattern for wave condition H_S = 3 m; T_P = 14 s; $\theta = 45^0/135^0$; MWL = 0 m (refer to Figure 4-3 (c)) is consistent to Trampenau *et al.*'s (2004) findings for low levels of flow constriction, shown in Figure 2-9. The flow structure consists of relatively high velocities on both sides of the groynes and compact, elliptical eddy circulation on the lee side. The breaker line depicted in Figure 4-3 (c) extends past the groyne tip (G_L/B_Z = 0.909) therefore waves break outside the groyne length. The eddy circulation formed on Groyne C was observed to be larger compared to those formed on the leeward side of the groynes A and B.

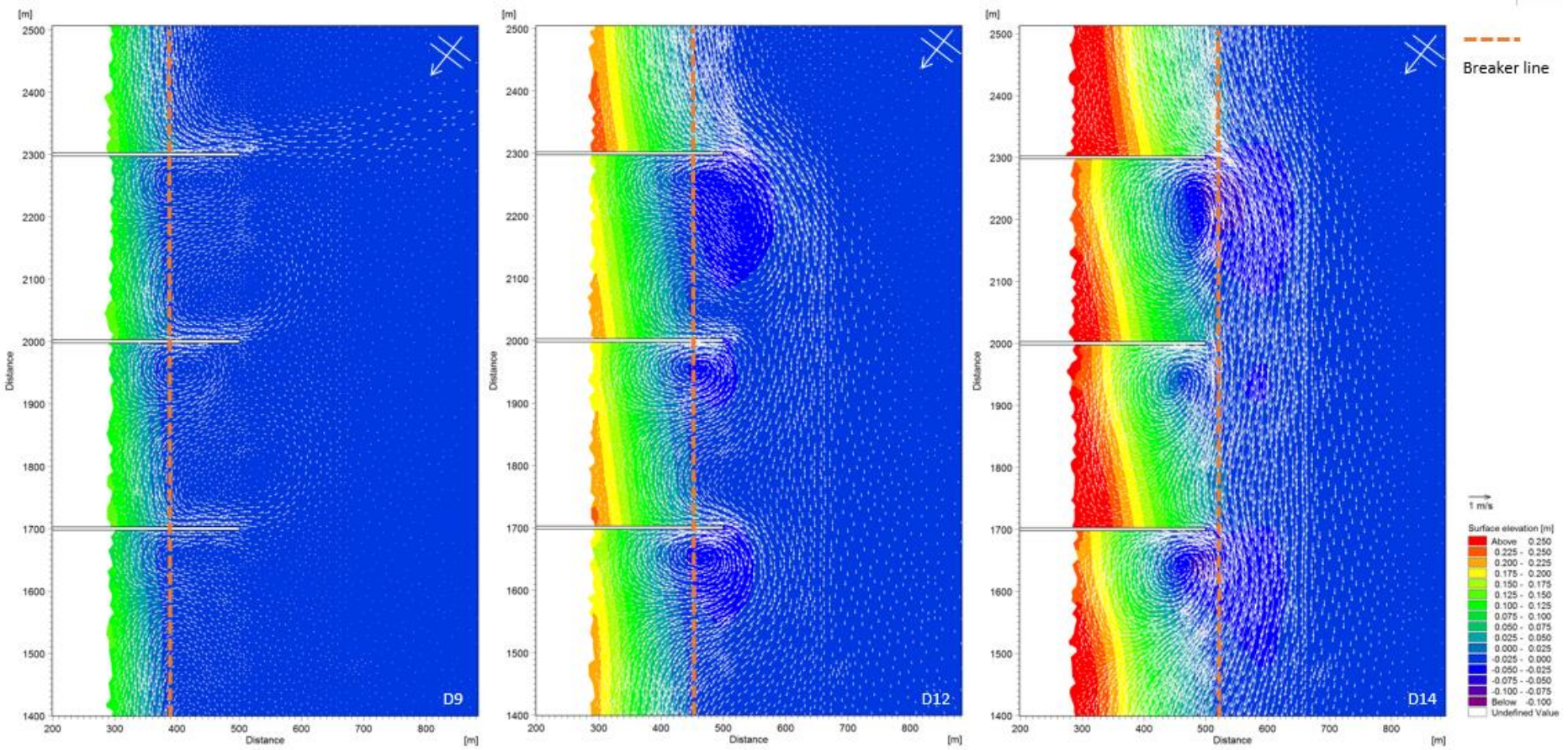

Figure 4-3 (a) (left): Predicted current vector plot and eddy circulation for wave condition (H_s = 1 m; T_p = 14 s; θ = $45^0/135^0$; MWL = 0), G_L /B_Z = 2.22 and G_S = 300 m (Model run D9), **(b) (centre):** Predicted current vector plot and eddy circulation for wave condition (H_s = 2 m; T_p = 14 s; θ = $45^0/135^0$; MWL = 0), G_L /B_Z = 1.33 and G_S = 300 m (Model run D12) and **(c) (right):** Predicted current vector plot and eddy circulation for wave condition (H_s = 3 m; T_p = 14 s; θ = $45^0/135^0$; MWL = 0), G_L /B_Z = 0.91 and G_S = 300 m (Model run D14)

4.3.2 Mean water level variation (MWL)

As previously noted and shown in section 4.2.2, mean water level variation is the method used in this study to vary the groyne span, thus affecting both the non-dimensional ratios G_S/G_L and G_L/B_Z. The breaker zone width is not affected by the variation as the wave condition remained unchanged, however the breaker line location in relation to the groyne length in the active water zone was affected. Mean water level was varied in order to elucidate the formation of eddy circulation, groyne tip velocity magnitude and direction, circulation zones and rip currents in a groyne field arrangement.

Table 4-8 summarizes the findings on varying the groyne length in active water by varying the water level which affects the flow constriction, current groyne tip velocity magnitude, direction and tip velocity ($\frac{|Vtip|}{H_S/T_P}$) for groynes C (upstream groyne), B (central groyne) and A (downstream groyne).

Table 4-8: Effects of varying water level on the geometric parameters and flow constriction for wave condition H_s = 1 m; T_p = 14 s; θ = $45^0/135^0$; G_S= 300 m.

MWL (m)	G_L (m)	B_Z (m)	$\frac{G_S}{G_L}$	$\frac{G_L}{B_Z}$	Groyne C			Groyne B			Groyne A		
					$\lvert Vtip\rvert$ (m/s)	$\frac{\lvert Vtip\rvert}{H_S/T_P}$	$\beta(^0)$	$\lvert Vtip\rvert$ (m/s)	$\frac{\lvert Vtip\rvert}{H_S/T_P}$	$\beta(^0)$	$\lvert Vtip\rvert$ (m/s)	$\frac{\lvert Vtip\rvert}{H_S/T_P}$	$\beta(^0)$
-1	150	90	2.000	1.667	0.334	4.674	66	0.157	2.194	69	0.174	2.440	72
0	200	90	1.500	2.222	0.205	2.873	82	0.090	1.255	55	0.145	2.035	74
1	250	85	1.200	2.941	0.201	2.809	67	0.064	0.898	54	0.047	0.656	53

The breaker line for water level condition MWL = -1 is depicted in Figure 4-4 (a) located more toward the groyne tip compared to the other water level conditions. As a result the flow constriction was found to be lower (G_L/B_Z = 1.667), however the groyne spacing to groyne length ratio was found to be higher (G_S/G_L = 2) compared to the other water level conditions. Low flow constriction resulted in higher groyne tip velocity magnitude due to the breaker zone width location towards the groyne tip. Flow patterns described in Figure 4-4 (a) appear similar to that of Figure 4-4 (b), however the notable differences are the groyne tip velocity magnitude and direction for groyne C, the eddy circulation and recirculation size and shape. The 1 m reduction in water level resulted in 50 m shoreline retreat seaward, ultimately reducing the groyne length in active water zone from 200 m to 150 m. The flow patterns formed in the groyne field reduced in size as eddies became circular and compact due to the increased velocity within the groyne field. The current speed peaked on the upstream side for all groynes. The eddy circulation formed on the lee side of groyne C became smaller in size due to a large leeward current combining with the upstream rip current at the groyne tip.

Figure 4-4 (b) show an eddy circulation on the leeward side of groyne C and a second eddy circulation upstream of groyne B (eddy recirculation) for wave condition H_S = 1 m; T_P = 14 s; θ = $45^0/135^0$; MWL = 0 m. The increase in the G_L/B_Z ratio from 1.667 to 2.222 and reduction in the G_S/G_L from 2 to 1.5 due to the groyne length increase resulted in the reduction in the groyne tip velocity on all the groynes.

The flow pattern depicted in Figure 4-4 (b) show high rip current upstream of Groyne C. This was found to be typical for waves breaking closer to the shoreline as opposed to waves breaking towards the groyne tip. The eddy circulation formed on the lee side of groyne C was strengthened by the recirculation eddy triggering a zone of two eddy circulations between the groynes.

The flow pattern associated with wave condition H_S = 1 m; T_P = 14 s; $\theta = 45^0/135^0$; MWL = 1 m is shown in Figure 4-4 (c). The G_L/B_Z ratio increased from 2.222 to 2.941 and the G_S/G_L ratio reduced from 1.5 to 1.2 as a result of the groyne length increase from 200 m to 250 m. Here the eddy circulation and recirculation size increased compared to that of Figure 4-4 (a) and Figure 4-4 (b). The breaker line shown in Figure 4-4 (c) moved shoreward. The eddy circulation therefore became elliptical in shape and bigger in size. The recirculation eddy formed upstream of groyne A and B appeared to form an additional eddy within the recirculation zone, thereby presenting three potential eddies between the two groynes. The groyne tip velocity magnitude reduced for the downstream groyne A and B as a result of the eddy size an observation that reinforces the findings by Trampenau *et al.,* (2004) who found that bigger eddy circulations experience lower velocities than compact eddies.

These results show that the flow structure did not significantly change as a result of water level variations. However the current speed within circulation zones increases for compact eddies and reduces for elliptical eddies. Lower water levels yield higher groyne tip current velocity magnitude compared to the elevated water levels. The results further reinforce the relationship that exists between the flow constriction and the groyne tip velocity.

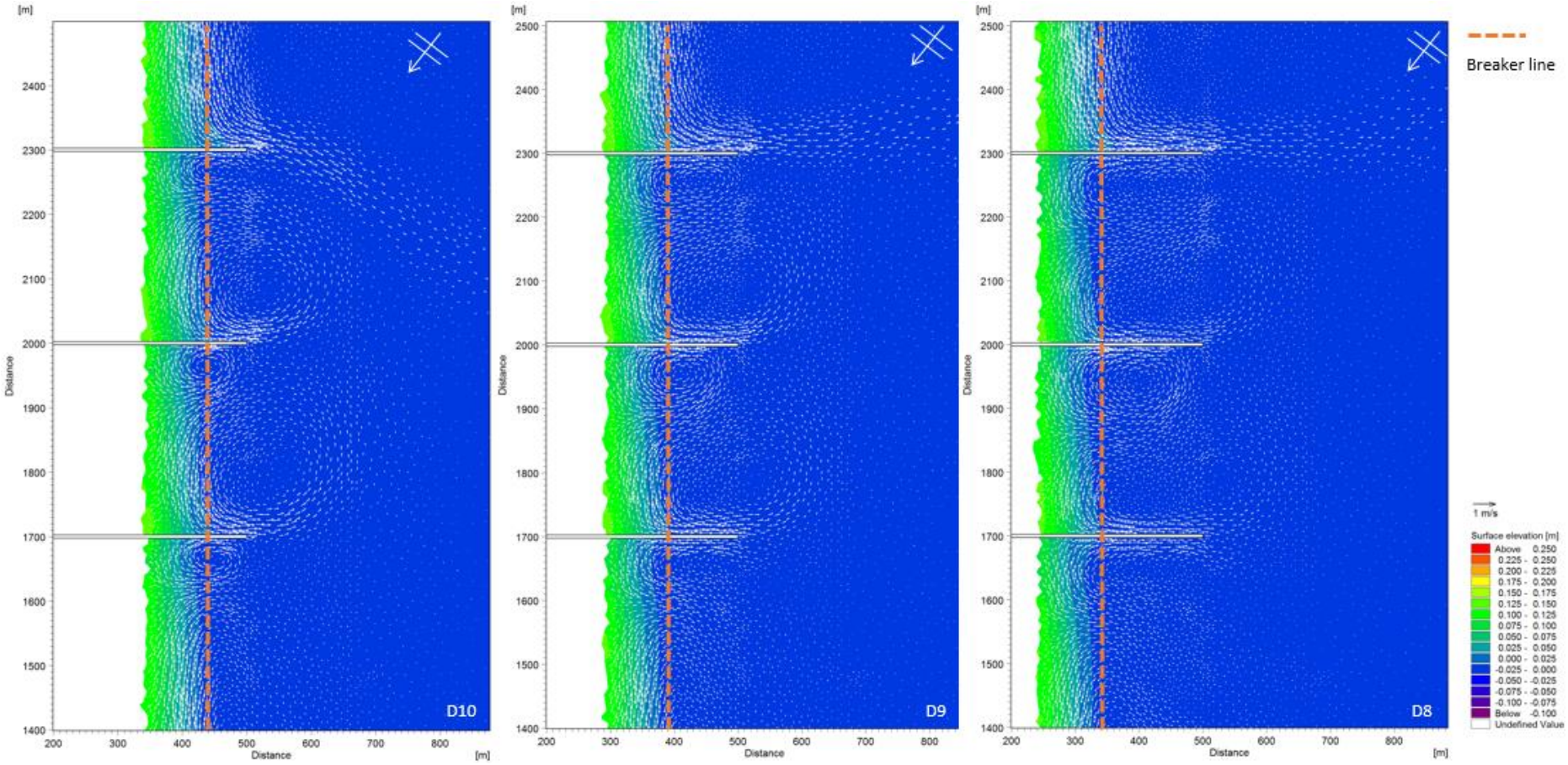

Figure 4-4 (a) (left): Predicted current vector plot and eddy circulation for (H_s = 1 m; T_p = 14 s; θ = $45^0/135^0$; MWL = -1), G_L /B_Z = 1.67 and G_S = 300 m (Model run D10), **(b) (centre)**: Predicted current vector plot and eddy circulation for (H_s = 1 m; T_p = 14 s; θ = $45^0/135^0$; MWL= 0), G_L /B_Z = 2.22 and G_S = 300 m (Model run D9) and **(c) (right)**: Predicted current vector plot and eddy circulation for (H_s = 1 m; T_p = 14 s; θ = $45^0/135^0$; MWL = 1), G_L /B_Z = 2.94 and G_S = 300 m (Model run D8)

From the above observations it may be concluded that water level variation does not affect the breaker zone width but rather relocates the breaker zone relative to the groyne length for the given wave condition. The water level variation/groyne length variation analysis was conducted for a higher significant wave height of 2 m to explore if the findings for significant wave height of 1m would hold true. A summary of the results is presented in Table 4-9.

Table 4-9: Effect of varying mean water level on the geometric parameters and the flow constriction for wave condition H_s = 2 m; T_p = 14 s; θ = 45^0/135^0; G_S = 300 m.

MWL (m)	G_L (m)	B_Z (m)	$\frac{G_S}{G_L}$	$\frac{G_L}{B_Z}$	Groyne C			Groyne B			Groyne A		
					|Vtip| (m/s)	$\frac{\|Vtip\|}{H_S/T_P}$	β(^{0})	|Vtip| (m/s)	$\frac{\|Vtip\|}{H_S/T_P}$	β(^{0})	|Vtip| (m/s)	$\frac{\|Vtip\|}{H_S/T_P}$	β(^{0})
-1	150	150	2.000	0.939	0.933	6.531	31	0.695	4.862	23	0.793	5.554	30
0	200	150	1.500	1.333	0.833	5.829	47	0.399	2.794	32	0.527	3.688	45
1	250	150	1.200	1.667	0.667	4.671	67	0.222	1.557	68	0.331	2.318	66

Due to the increased significant wave height from 1 m (previous results) to 2 m and reduced water level the flow pattern corresponding to wave condition H_s = 2 m; T_P = 14 s; θ = 45^0; MWL = -1 m is shown in Figure 4-5 (a). The flow constriction was found to be 0.939 which is an indication that the breaker zone extends beyond the groyne length. As depicted in the Figure 4-5 (a), the breaker line is located toward the groyne tip which presents high current velocity towards the groyne tip. This is evident on the results as the groyne tip velocity magnitude ranged from 0.793 – 0.933 m/s peaking on the tip of groyne C. The groyne tip velocity direction was found to range from 23^0 to 31^0 for all the groynes suggesting predominantly alongshore current. The flow patterns presented in Figure 4-5 (a) is in agreement. The flow pattern show compact eddies on the lee side of all the groynes.

The flow pattern for MWL = 0 m (refer to Figure 4-5 (b)) shows the eddy formed on groyne C to be irregular in shape compared to the eddy circulations formed on groynes A and B. The increase in the water level from -1 m to 0 m resulted in the increase in the groyne span in the active water zone, thus the breaker line depicted on the figure moved shoreward resulting in the increase in the G_L/B_Z ratio from 0.939 to 1.333. The increase in the flow constriction resulted in the groyne tip velocity magnitude decrease range from 0.399 – 0.833 m/s and the groyne tip velocity angle increase range from 32^0 – 47^0. The water surface elevation upstream of groyne C was observed to be in excess of 0.25 m above the mean water level, while the downdrift side shows low water surface elevation. This high water level is due to low velocity as a result of alongshore current diversion. Trampenau, *et al*. (2004) found that for conditions where the breaker zone width is located towards the groyne tip, small circulation zones can develop up drift of a groyne towards the shoreline, resulting in low localized velocities and elevated water surface. Consequently upstream accretion and downstream erosion of the groynes can be expected for such conditions. The G_S/G_L ratio reduced from 2 to 1.5 and the flow patterns observed for MWL =

0 m and MWL = -1 m appear to be dissimilar. Having varied the groyne length from 150 m to 200 m it can be seen from Figure 4-5 (b) and the results that the groyne tip velocity and flow constriction were affected. This can be attributed to the breaker zone position as result of the change, therefore indicating that geometric property of the groyne such as groyne span affect flow characteristics.

The elevated water level for wave condition H_s = 2 m; T_P = 14 s; $\theta = 45^0$; MWL = 1 m is depicted in Figure 4-5 (c). The groyne length increased from 200 m to 250 m resulting in the flow constriction increase from 1.333 to 1.667. The breaker line depicted in Figure 4-5 (c) show the location of the breaker line more toward the groyne midspan. The groyne tip velocity reduced and the angle increased. The velocity and the angle ranged from 0.222 – 0.667 m/s and 66^0 – 68^0 respectively. The flow structure depicts eddy recirculation between the groynes. The results suggest a tendency of eddy recirculation when the flow constriction is greater than 1.4. The recirculation zones between the groynes can be observed in the figure due to the geometric variation.

The both set of results for H_s = 1 m and 2m showed a strong correlation between the non-dimensional parameters G_S/G_L, G_L/B_Z and $\frac{|Vtip|}{H_S/T_P}$. The clearest relationship exist between the G_L/B_Z and $\frac{|Vtip|}{H_S/T_P}$. A decrease in the flow constriction resulted in an increase in the tip velocity and vice versa. The increase in the flow constriction was mainly due to the groyne length reduction and the wave parameters were kept constant, thus the effect was mainly geometric. The G_S/G_L ratio reduced accordingly with the increase in the groyne length. The reduction in the groyne spacing to length ratio is associated with a reduction in the tip velocity.

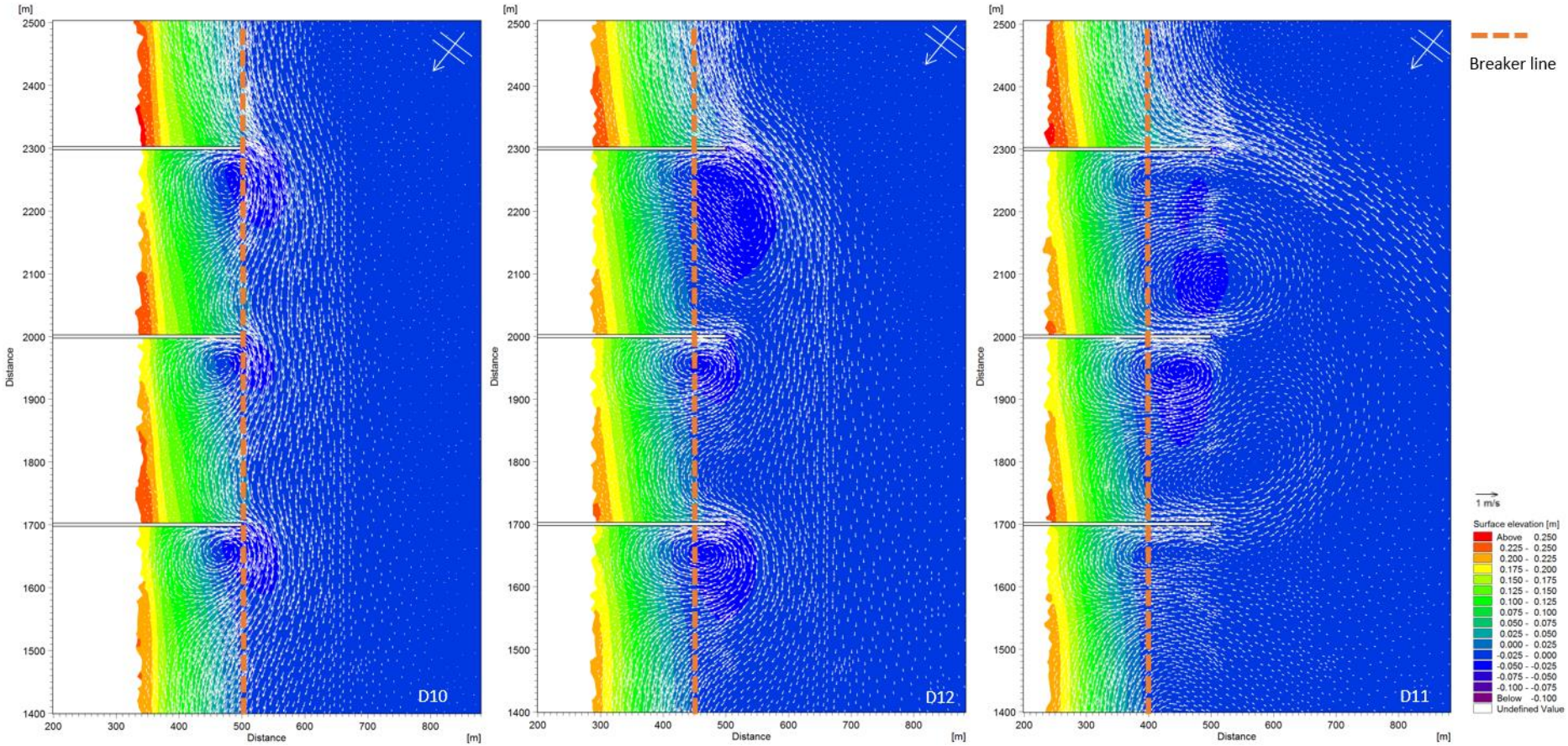

Figure 4-5 (a) (left): Predicted current vector plot and eddy circulation for wave condition (H_s = 2m; T_p = 14s; θ = $45^0/135^0$; *MWL* = -1), G_L /B_Z = 0.94 and G_S = 300 m (Model run D10), **(b) (centre):** Predicted current vector plot and eddy circulation for wave condition (H_s = 2m; T_p = 14s; θ = $45^0/135^0$; *MWL* = 0), G_L /B_Z = 1.33 and G_S = 300 m (Model run D12) and **(c) (right):** Predicted current vector plot and eddy circulation for wave condition (H_s = 2m; T_p = 14s; θ = $45^0/135^0$; *MWL* = 1), G_L /B_Z = 1.67 and G_S = 300 m (Model run D11)

4.3.3 Incident wave angle variation

Section 4.2.3 showed how varying the incident wave angle affects the peak gradient of the radiation stress and the breaker zone width. Studies such as Lucca (2012) found that the incident wave angle has weaker effects on the breaker zone width compared to other wave conditions. The findings of Section 4.2.3 will now be used to explore the impact of varying the incident wave angle on the flow structure and current speed within a groyne field. Three incident wave angles were investigated and the results are summarized in Table 4-10.

Table 4-10: The effect of varying incident wave angle on the flow constriction, the groyne tip velocity and direction for wave condition H_s = 1 m; T_p = 14 s; *MWL* = 0 m; G_S = 300 m.

θ degrees	G_L (m)	B_Z (m)	$\frac{G_S}{G_L}$	$\frac{G_L}{B_Z}$	Groyne C			Groyne B			Groyne A		
					|Vtip| (m/s)	$\frac{\|Vtip\|}{H_S/T_P}$	**β(^{0})**	**|Vtip| (m/s)**	$\frac{\|Vtip\|}{H_S/T_P}$	**β(^{0})**	**|Vtip| (m/s)**	$\frac{\|Vtip\|}{H_S/T_P}$	**β(^{0})**
$150^0/30^0$	200	75	1.500	2.667	0.153	2.139	79	0.162	2.271	23	0.212	2.969	80
$135^0/45^0$	200	90	1.500	2.222	0.145	2.035	55	0.090	1.255	32	0.205	2.873	82
$120^0/60^0$	200	100	1.500	2.000	0.191	2.668	80	0.191	2.672	68	0.274	3.842	78

The results in Table 4-10 show various flow constriction, groyne tip velocities magnitude and direction as a result of incident wave angle variation. The results were expected as the incident wave angle was shown to affect the breaker zone width in section 4.2.3. Wave conditions depicted in Figure 4-6 (a), Figure 4-6 (b) and Figure 4-6 (c) show flow patterns dominated by eddy recirculation between the groynes. Groyne A experienced the highest groyne tip velocity magnitude for all incident wave angle condition as expected. The sheltering effect is evident in the flow patterns and the tip velocity and directions for the different incident wave angle conditions. The results show a typical flow structure consisting of eddy recirculation between the groynes for high flow constriction ($G_L/B_Z > 1.4$). The flow structure appears to be similar for all three incident wave angle conditions.

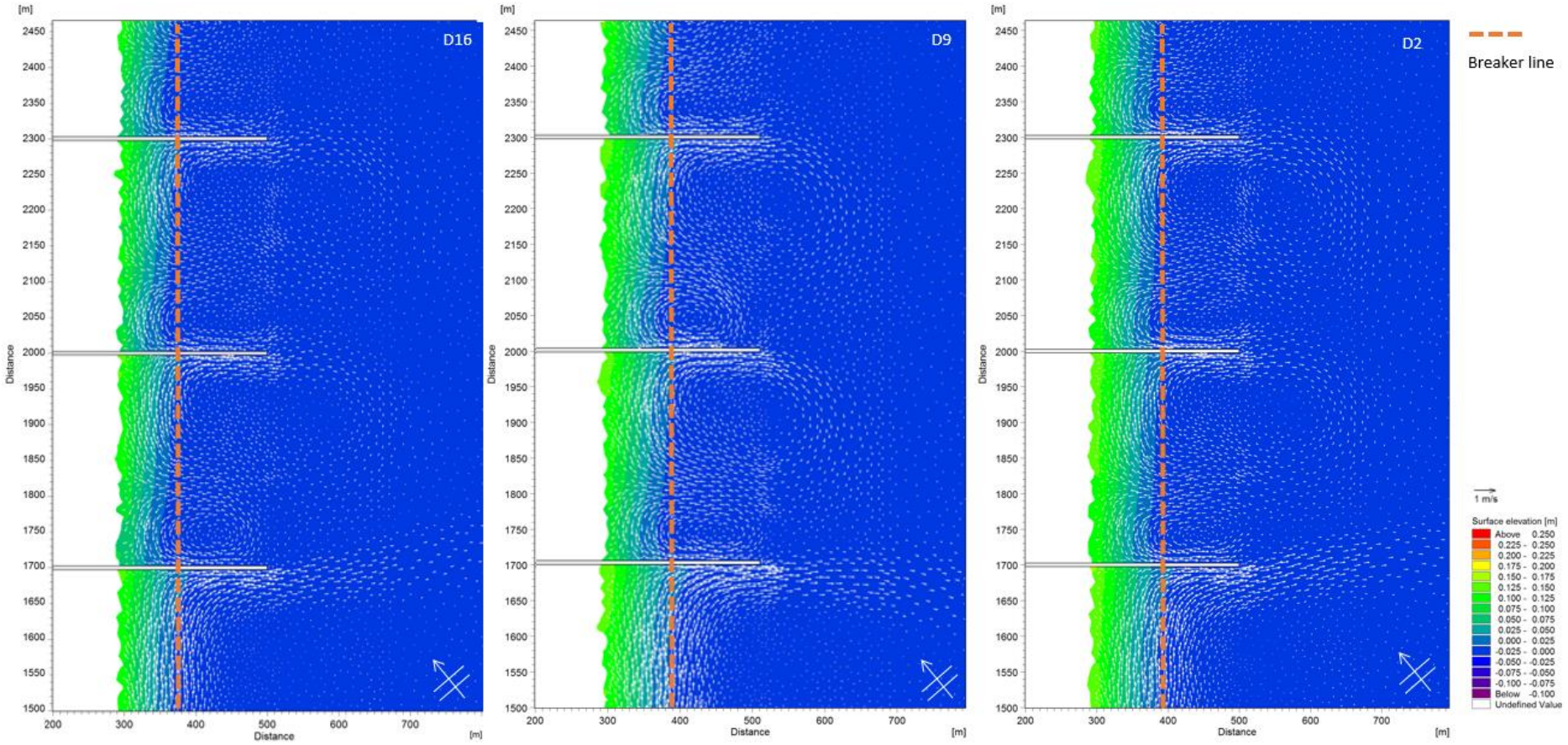

Figure 4-6 (a) (left): Predicted current vector plot and eddy circulation for wave condition (H_s = 1 m; T_p = 14 s; θ = $150^0/30^0$; *MWL* = 0), G_L /B_Z = 2.67 and G_S = 300 m (Model run D16), **(b) (centre):** Predicted current vector plot and eddy circulation for wave condition (H_s = 1 m; T_p = 14 s; θ = $135^0/45^0$; *MWL* = 0), G_L /B_Z = 2.22 and G_S = 300 m (Model run D9) and **(c) (right):** Predicted current vector plot and eddy circulation for wave condition (H_s = 1 m; T_p = 14 s; θ = $120^0/60^0$; *MWL* = 0), G_L /B_Z = 2 and G_S = 300 m (Model run D2)

4.3.4 Groyne inter-spacing variations

Groyne field design studies such as Castelle *et al*., (2006) and Zanuttigh *et al*., (2005) suggest an optimal groyne spacing of 1.5 – 3 times the groyne length. Other studies such as Trampenau *et al*., (2004) suggest that admissible groyne spacing can be up to 5 times the groyne length. This section aims to explore the effects of varying groyne spacing on the groyne tip velocity, direction and flow patterns for groynes summarized in Table 4-11. Groyne A is the upstream groyne, B is the central groyne and C is the downstream groyne. It is important to note that for the results presented below, the wave incident angle of 120^0 is equivalent to 60^0. As a result, the upstream groyne is A while C is the downstream groyne.

Table 4-11: The effect of varying G_S/G_L ratio on the flow characteristics for wave condition H_s = 1 m; T_P = 14 s; θ = $120^0/60^0$; *MWL* = 0 m.

$\frac{G_S}{G_L}$	G_L (m)	B_Z (m)	$\frac{G_L}{B_Z}$	Groyne C			Groyne B			Groyne A		
				|Vtip| (m/s)	$\frac{\|Vtip\|}{H_S/T_P}$	**β(^{0})**	**|Vtip| (m/s)**	$\frac{\|Vtip\|}{H_S/T_P}$	**β(^{0})**	**|Vtip| (m/s)**	$\frac{\|Vtip\|}{H_S/T_P}$	**β(^{0})**
1.000	200	100	2.000	0.066	0.929	12	0.054	0.756	1	0.227	3.182	87
1.750	200	90	2.222	0.109	1.532	59	0.183	2.568	65	0.269	3.762	76
2.000	200	90	2.222	0.215	3.007	73	0.214	2.994	70	0.266	3.728	84
3.000	200	90	1.500	0.377	5.278	81	0.363	5.078	82	0.362	5.062	87

It is important to note that the wave condition was kept unchanged for the results presented in Table 4-11. The parameter varied was the groyne spacing and water level for G_S/G_L = 2. As previously stated in section 4.3.2, varying the G_S/G_L ratio can be achieved by either varying the mean water level which ultimately affects the groyne length in contact with the active water zone, or varying the groyne spacing. Both methods do not affect the breaker zone width.

The closely spaced groyne with G_S/G_L = 1 shown in Figure 4-7 (a) shows flow patterns consisting of recirculation eddies associated with G_L/B_Z greater than 1.4. The eddy circulation zones observed to develop are confined and compact. Groyne A experienced strong cross shore current while the downstream groynes were sheltered. Two eddies formed (lee side eddy and recirculation eddy) within the groyne compartments. The two eddies are approximately the same size and shape. The groyne tip velocity magnitudes ranged from 0.054 – 0.227 m/s peaking on groyne A for G_S/G_L = 1. It is also noted that the velocity for condition G_S/G_L = 1 was low particularly for downstream groynes compared to other groyne spacing conditions G_S/G_L = 1.75, 2 and 3. The groyne tip velocity directions ranged from 1^0 - 87^0. The results for tip velocity direction are in agreement with the flow patterns depicted by Figure 4-7 (a) showing rip currents on Groyne A and eddy circulation zones for downstream groynes.

It is evident from the results that increasing the G_S/G_L ratio from 1 to 1.75 increased the groyne tip velocity magnitudes on all the groynes. The groyne tip velocity magnitude ranged from 0.109 – 0.269

m/s from groyne C to Groyne A, as expected the upstream groyne experienced highest velocity which is consistent with the previous results. The variation in G_S/G_L also resulted in bigger eddy circulation formation between all the groynes as depicted in Figure 4-7 (b). The sheltering effect provided by the first groyne is evident in the tip velocities and the flow patterns. The groyne tip velocity direction ranged from 59^0 - 76^0. This is an indication that the groyne spacing strongly affects the groyne tip velocity direction and magnitudes (both scaled and unscaled).

The $G_S/G_L = 3$ case shown in Figure 4-7 (c) shows a similar flow structure to the previous groyne spacing condition ($G_S/G_L = 1.75$) with larger eddies. For the specified condition, the G_S/G_L was varied by reducing the groyne length in contact with the water zone. The results suggest a strong correlation between the G_S/G_L and both scaled and non-scaled velocities. Results show that an increase in the G_S/G_L results in groyne tip velocities and angle increase. The groyne leeward side eddy for all three groynes appear to be the same size.

The G_S/G_L ratio variations suggest that an increase in the ratio may result in groyne tip velocity increase. The lower the ratio was the less effective the groyne field due to downstream groynes being sheltered, groyne tip velocities reduced in magnitudes and the flow patterns showed that downstream groynes tended to confine the flow within the compartments. The results support Castelle *et al*., (2006) and Zanuttigh *et al*., (2005) groyne spacing recommendations. It is evident from the results that the increase in G_S/G_L resulted in improved circulation within the groynes and increase in groyne tip velocities. $G_S/G_L = 3$ showed high rip currents developing updrift of the groynes and the groyne tip velocities direction were in agreement with this finding. Furthermore, the non-dimensional tip velocities increased for all the groynes for higher G_S/G_L ratio. This suggests that the groynes start behaving more as independent structures for large G_S/G_L ratios with higher risk of groyne tip local scouring. This finding is not consistent with the Trampenau *et al*., (2004) suggestion, however Trampenau *et al*. did note that groyne spacing depends on a number of parameters such as site specific wave conditions, beach slope, etc.

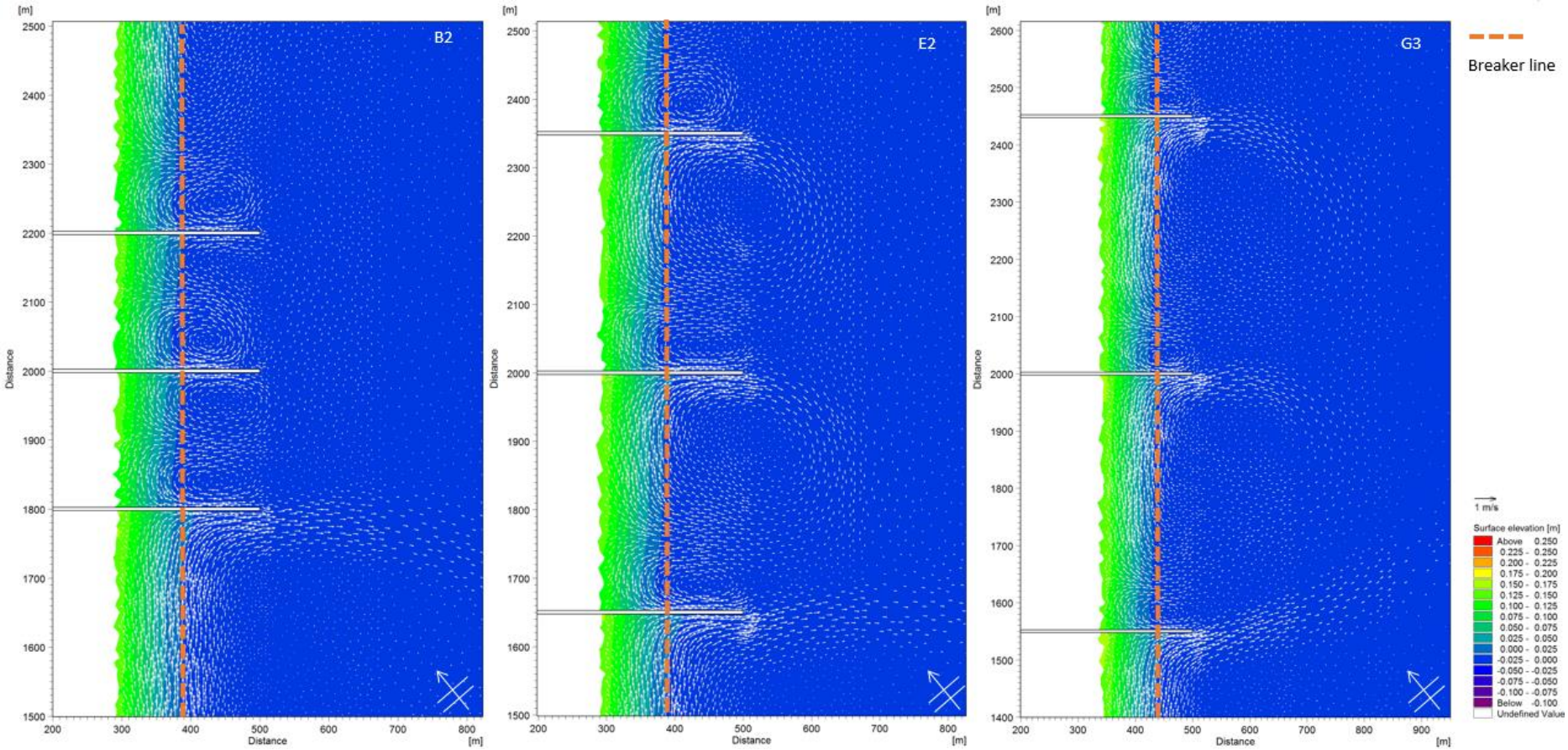

Figure 4-7 (a) (left): Predicted current vector plot and eddy circulation for wave condition (H_s = 1m; T_p = 14s; θ = $120^0/60^0$; MWL = 0), G_L /B_Z = 2 and G_S/G_L = 1 (Model run B2), **(b) (centre):** Predicted current vector plot and eddy circulation for wave condition (H_s = 1m; T_p = 14s; θ = $120^0/60^0$; MWL = 0), G_L /B_Z = 2.22 and G_S/G_L = 1.75 (Model run E2) and **(c) (right):** Predicted current vector plot and eddy circulation for wave condition (H_s = 1m; T_p = 14s; θ = $120^0/60^0$; MWL = -1), G_L /B_Z = 1.500 and G_S/G_L = 3 (Model run G3).

4.4 Storm event

In this section storm event effects on a groyne field are explored. As previously noted in the literature, storm event is referred to an event whereby a significant wave height threshold is exceeded. A Durban storm event is considered to commence when the significant wave height exceeds 3.5m and ends when the wave height falls below 3.5m for a period of at least 2 weeks depending on the decay time of the autocorrelation (Corbella & Stretch, 2012c).

4.4.1 Groyne spacing to groyne length during storm event

Section 4.3.4 showed that groyne spacing is essential in a groyne field. As stated in that section groyne spacing to groyne length ratio from 1 (small spacing) to 3 (large spacing) was recommended by a number of studies. The destructive nature that storm conditions have on coastal environments presents a unique challenge for groyne stability and coastal erosion. The effect of the G_S/G_L during storm event on the groyne tip velocity magnitude and direction is presented in Table 4-12.

Table 4-12: The effect of groyne spacing to groyne length ratio on the groyne tip velocity magnitude and direction for wave condition $\boldsymbol{H_s}$ = 3.5 m; $\boldsymbol{T_p}$ = 14 s; $\boldsymbol{\theta}$ = $120^0/60^0$; *MWL* = 0 m.

$\frac{G_S}{G_L}$	G_L (m)	B_Z (m)	$\frac{G_L}{B_Z}$	Groyne C			Groyne B			Groyne A		
				|Vtip| (m/s)	$\frac{\|Vtip\|}{H_S/T_P}$	**β(^{0})**	**|Vtip| (m/s)**	$\frac{\|Vtip\|}{H_S/T_P}$	**β(^{0})**	**|Vtip| (m/s)**	$\frac{\|Vtip\|}{H_S/T_P}$	**β(^{0})**
1.250	200	300	0.667	1.146	4.582	18	1.018	4.072	8	1.349	5.395	31
2.000	200	300	0.667	1.252	5.009	32	1.010	4.039	20	1.433	5.730	35
3.000	200	300	0.667	1.348	5.391	31	1.329	5.317	33	1.369	5.475	32

Similarly to section 4.3.4, the effect of G_S/G_L ratio on the flow pattern was presented in Figure 4-8.

The results suggest high groyne tip velocity magnitude for all groyne spacing to groyne length conditions due to low levels of flow constriction ratio. This is expected for storm events due to high significant wave height. As can be seen in Figure 4-8, the breaker line for the three flow structures was found to extend far beyond the groyne length.

The flow pattern for G_S/G_L = 1.25 is depicted in Figure 4-8 (a). Due to the close spacing of the groynes, the lee side eddy circulation formed occupied the compartments between all three groynes. Due to these eddy circulations, the water surface was elevated and high groyne tip velocity magnitude developed. Accretion upstream and erosion down drift of the groynes maybe expected for such conditions. Corbella & Stretch, (2012c) established a beach erosion trend for such storm events. Due to high differential water surface elevation between the groynes, gravity currents may develop between the groynes. Trampenau *et al.* (2004) suggested this phenomenon to occur particularly for impermeable groynes. The majority of the flow bypassed the groyne compartments and moved across the groyne tips. This results in high groyne tip velocity as shown in Table 4-12.

The G_S/G_L ratio was increased from 1.25 to 2 and the results are depicted in Figure 4-8 (b). Eddy circulation size on the lee side of the first groyne increased. All eddy circulations were compact and circular, indicating high current speed as suggested by Trampenau *et al.* (2004). The groyne tip velocity magnitude increased accordingly. The eddy circulation formed on Groyne B was observed to be smaller and more circular compared to the first Groyne A and the Groyne C.

The G_S/G_L ratio was increased from 2 to 3 and the resulting flow pattern is depicted in Figure 4-8 (c). The eddy circulations which formed on the leeward side of all groynes appear to be compact and similar in size for all three groynes. The increase in G_S/G_L also affected the water surface elevation between the groynes as previously noted.

It was observed that for closely spaced groynes ($G_S/G_L = 1.25$) the main longshore flow simply bypassed the groyne compartments rendering the groynes ineffective in reducing current velocity. The eddy circulations formed on the leeward side of the groynes and tended to occupy the entire compartment region between the groynes. The higher the G_S/G_L ratio became the less confined the flow structure became. The results suggest that under storm conditions large size eddy circulations form within an impermeable groyne field. Furthermore, the results suggest high groyne tip velocity magnitude develops due to the position of the breaker line and the main longshore flow bypassing the groyne compartments.

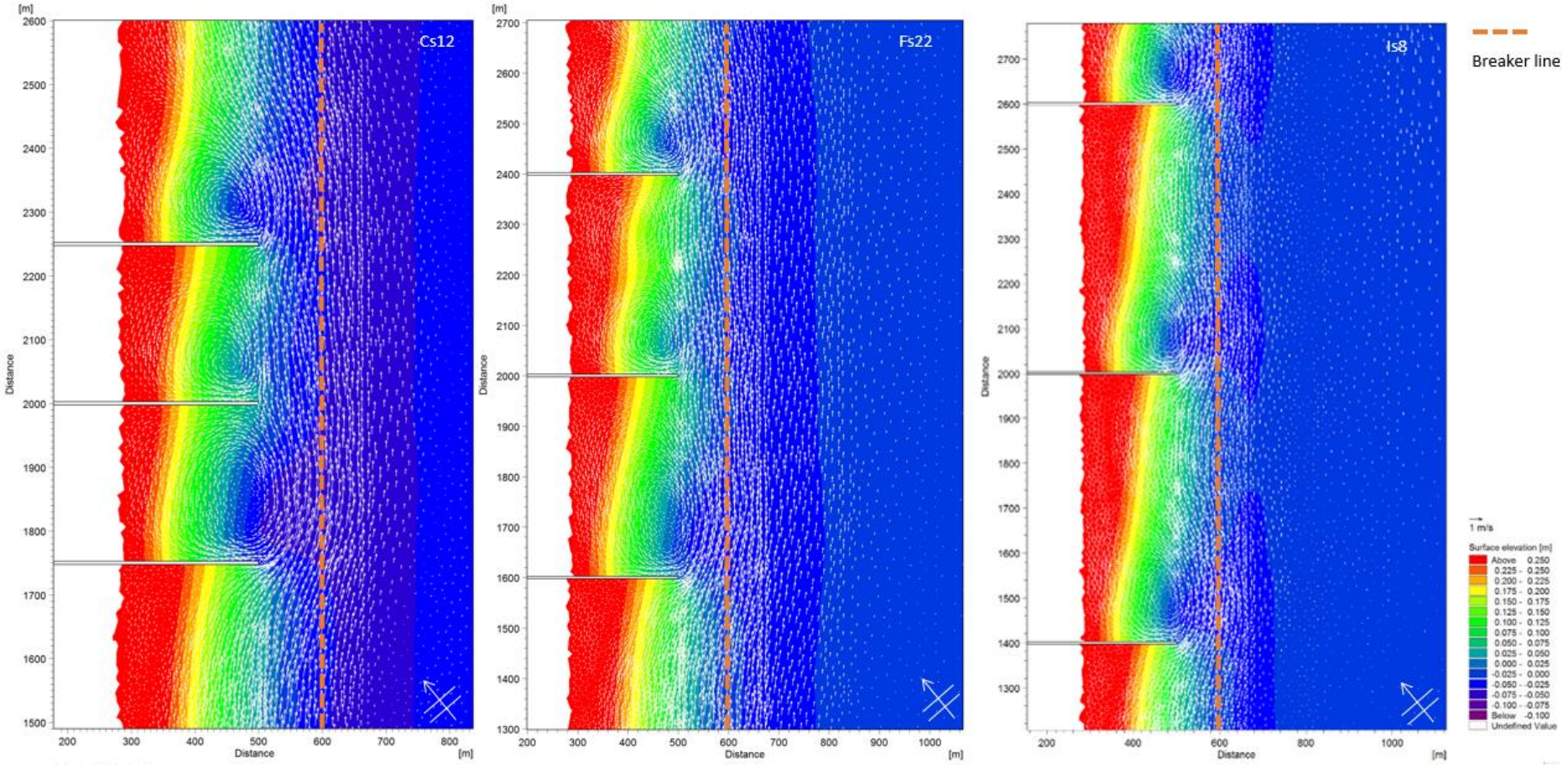

Figure 4-8 (a) (left): Predicted current vector plot and eddy circulation for (H_s = 3.5 m; T_p = 14 s; θ = $120^0/60^0$; *MWL* = 0), G_L /B_Z = 0.667 and G_S/G_L = 1.25 (Model run Cs12)**, (b) (centre):** Predicted current vector plot and eddy circulation for (H_s = 3.5 m; T_p = 14 s; θ = $120^0/60^0$; *MWL* = 0), G_L /B_Z = 0.667 and G_S/G_L = 2.00 (Model run Fs22) and **(c) (right):** Predicted current vector plot and eddy circulation for (H_s = 3.5 m; T_p = 14 s; θ = $120^0/60^0$; *MWL* = 0), G_L /B_Z = 0.667 and G_S/G_L = 3.00 (Model run Is8)

4.4.2 Critical storm event

Previous sections have shown low flow constriction is associated with high groyne tip velocity magnitudes. The resulting flow structure consists of compact eddies within the groyne field suggesting high circulation velocity within an eddy and groyne tip velocity. Having used mean water variation method to vary the geometric parameter (G_S/G_L) in section 4.3.2, a similar method was used in this section. The effect of varying groyne span for wave condition H_s = 3.5 m; T_P = 14 s; θ = $135^0/45^0$; G_s = 400 m on the flow constriction, groyne tip velocity magnitude and direction is presented in Table 4-13. Groyne A is the upstream groyne while Groyne C is the downstream groyne.

Table 4-13: The effect of varying groyne length in contact with active water zone on the flow constriction, groyne tip velocity magnitude and direction for wave condition (H_s = 3.5 m; T_p = 14 s; θ = $135^0/45^0$)

MWL (m)	G_L (m)	B_Z (m)	$\frac{G_S}{G_L}$	$\frac{G_L}{B_Z}$	Groyne C			Groyne B			Groyne A		
					|Vtip| (m/s)	$\frac{\|Vtip\|}{H_S/T_P}$	β(^{0})	|Vtip| (m/s)	$\frac{\|Vtip\|}{H_S/T_P}$	β(^{0})	|Vtip| (m/s)	$\frac{\|Vtip\|}{H_S/T_P}$	β(^{0})
-1	150	300	2.667	0.500	1.428	5.712	18	1.319	5.276	23	1.456	5.823	23
0	200	300	2.000	0.667	1.374	5.498	28	1.364	5.457	32	1.573	6.291	31
1	250	300	1.600	0.833	1.196	4.784	39	1.246	4.985	68	1.575	6.302	38

The flow structure for G_S/G_L = 1.6 condition is depicted in Figure 4-9 (b) and corresponding current speed in Figure 4-10 (b). As depicted in the figures, the breaker line was observed to be beyond the groyne span as a result the G_L/B_Z ratio was found to be 0.833. High groyne tip velocity magnitude was observed and present in the table. The leeward side eddy circulation formed on groyne A was observed to be bigger in size compared to groyne B and C. The bigger eddy size is due to the elevated water level, resulting in increased groyne length and higher flow constriction. The breaker zone was located outside the groyne length. As a result the flow was predominantly alongshore and no recirculation patterns were observed as the G_L/B_Z ratio was lower than 1.4.

The flow structure for groyne span condition (G_S/G_L = 2) is shown in Figure 4-9 (a). The eddy circulations on the leeward side of all three groynes were observed to be compact, however reduced in size compared to G_S/G_L = 1.6 condition. The flow constriction reduced from 0.833 to 0.667, indicating high current speeds within the groyne field. The predicted current speed depicted in Figure 4-10 (a) precisely show where peak current speed occurs at the tip of groyne A.

The groyne spacing to groyne length condition showed the highest current speed conditions as depicted in Figure 4-9 (c). The flow constriction reduced from 0.667 to 0.500, while the groyne spacing to groyne length ratio increased from 2.00 to 2.67 due to the reduced groyne length from 200 m to 150 m. Thus presenting the flow structure depicted in Figure 4-9 (c). The eddy circulations for all three groynes

reduced in size significantly compared to the previous conditions. The reduction in size can attributed to majority of the flow bypassing the groyne compartments.

The results further reinforce those in section 4.3.2 where high levels of flow constriction are associated with high groyne tip velocity magnitudes. The predicted current speed plot depicted in Figure 4-10 (c) showed that higher G_S/G_L ratio present critical condition for groyne tip stability. The flow patterns shown by the figures seem to suggest predominant alongshore current for all the plots.

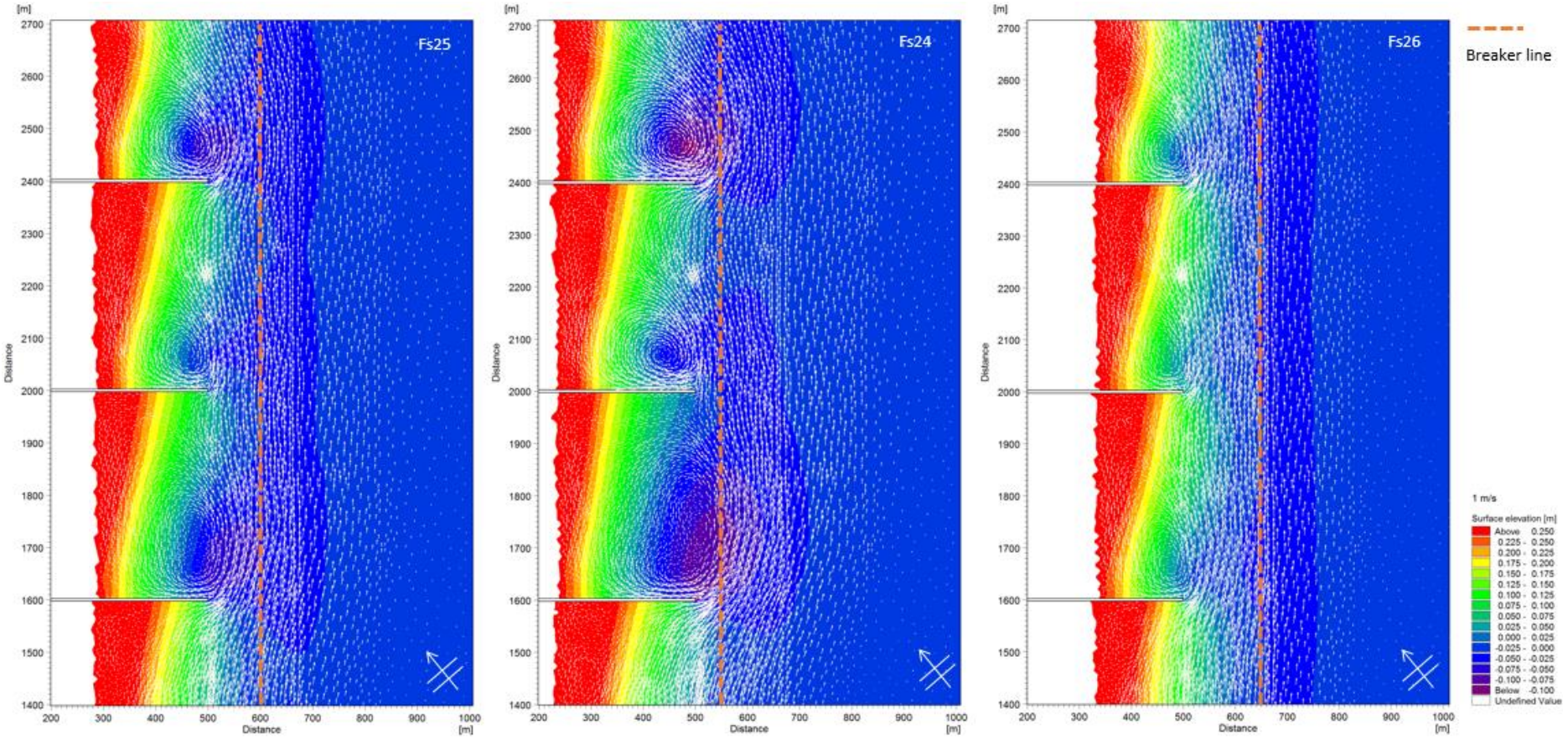

Figure 4-9 (a) (left): Predicted current vector plot and eddy circulation for (H_s = 3.5 m; T_p = 14 s; θ = $135^0/45^0$; *MWL* = 0), G_L /B_Z = 0.667 and G_S /G_L = 2.00 (Model run Fs25)**, (b) (centre):** Predicted current vector plot and eddy circulation for (H_s = 3.5 m; T_p = 14 s; θ = $135^0/45^0$; *MWL* = 1), G_L /B_Z = 0.833 and G_S /G_L = 1.60 (Model run Fs24) **and (c) (right):** Predicted current vector plot and eddy circulation for (H_s = 3.5 m; T_p = 14 s; θ = $135^0/45^0$; *MWL* = -1), G_L /B_Z = 0.500 and G_S /G_L = 2.67 (Model run Fs26)

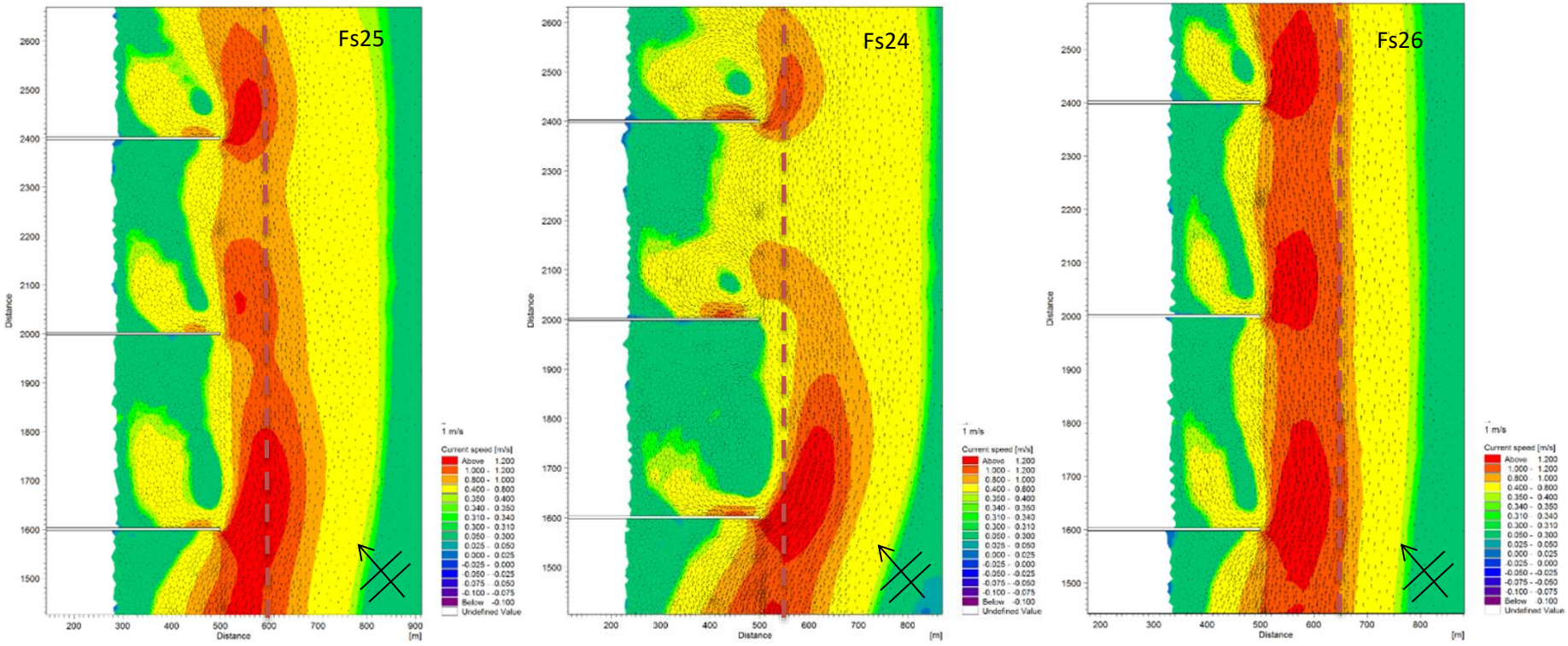

Figure 4-10 (a) (left): Predicted current speed plot for (H_s = 3.5 m; T_p = 14 s; θ = $120^0/60^0$; *MWL* = 0), G_L /B_Z = 0.667 and G_S /G_L = 2.00 (Model run Fs25), **(b) (centre):** Predicted current vector plot for (H_s = 3.5 m; T_p = 14 s; θ = $120^0/60^0$; *MWL* = 1), G_L /B_Z = 0.833 and G_S /G_L = 1.60 (Model run Fs24) and **(c) (right):** Predicted current vector plot for (H_s = 3.5 m; T_p = 14 s; θ = $120^0/60^0$; *MWL* = -1), G_L /B_Z = 0.500 and G_S /G_L = 2.67 (Model run Fs26)

4.5 Synthesis through dimensional Analysis

Dimensional analysis was undertaken to generalize the results from the previous section 4.3 and 4.4. The flow constriction ratio first described by Tarnowska, (1985) was used. The ratio has been used in numerous studies to describe the efficiency of a groyne (i.e. Walker *et al*., 1991; Trampenau *et al*., 2004; Lucca, 2013). The ratio and the groyne tip velocity, non-dimensionalized by the velocity scale Hs/Tp, are explored in this section to synthesize the results and give insight into the overall effects of the groyne field in reducing alongshore current, rip current and groyne tip velocities.

The synthesis through dimensional analysis was conducted and the results for tip velocity and the level of flow constriction were separated into three plots. Figure 4-11 plot is for upstream groyne, Figure 4-12 is for the central groyne and Figure 4-13 is for the downstream groyne. The plots were separated to show a clearer perspective for each groyne in the field. Section 4.3 and 4.4 showed predicted flow patterns for various wave and geometric conditions. The results from those two sections were plotted and presented in this section.

Previous results showed that upstream groyne in a field experiences highest current speed due to alongshore current diversion. The non-dimensional results for the upstream groyne (groyne 1) were plotted together with Lucca's, (2013) results for a single impermeable groyne. As previously noted in the literature, Lucca conducted a study titled "*flow patterns around groynes in the coastal zones"*. This was done to evaluate the effect of the level of flow constriction on the tip velocities. Lucca's results for impermeable groyne were summarized and presented on Table 4-14.

Table 4-14: The summary of wave parameters, tip velocity and scaled velocity for single impermeable groyne. The results were adapted from Lucca (2013, Ch. 6.7 pp 99 - 102).

$\boldsymbol{H_S}$ $(\boldsymbol{m})$	$\boldsymbol{T_P}$ $(\boldsymbol{s})$	$\boldsymbol{G_L}$ $(\boldsymbol{m})$	$\boldsymbol{B_Z}$ $(\boldsymbol{m})$	$\frac{\boldsymbol{G_L}}{\boldsymbol{B_Z}}$	u velocity (tip)	v velocity (tip)	|Vtip|	$\frac{\|Vtip\|}{(H_S/T_P)}$
1	14	200	90	90	0.25	0.05	0.26	3.61
1	14	200	116	116	0.35	0.10	0.36	5.10
2	14	237	157	157	0.69	0.39	0.79	5.55
3	14	237	213	213	0.90	0.88	1.26	5.87
3	14	225	221	221	0.88	0.90	1.26	5.87

The composite plot for the upstream groyne and Lucca's results are presented on Figure 4-11 showing non-dimensional parameters the G_L/B_Z, G_S/G_L and scaled groyne tip velocity magnitude.

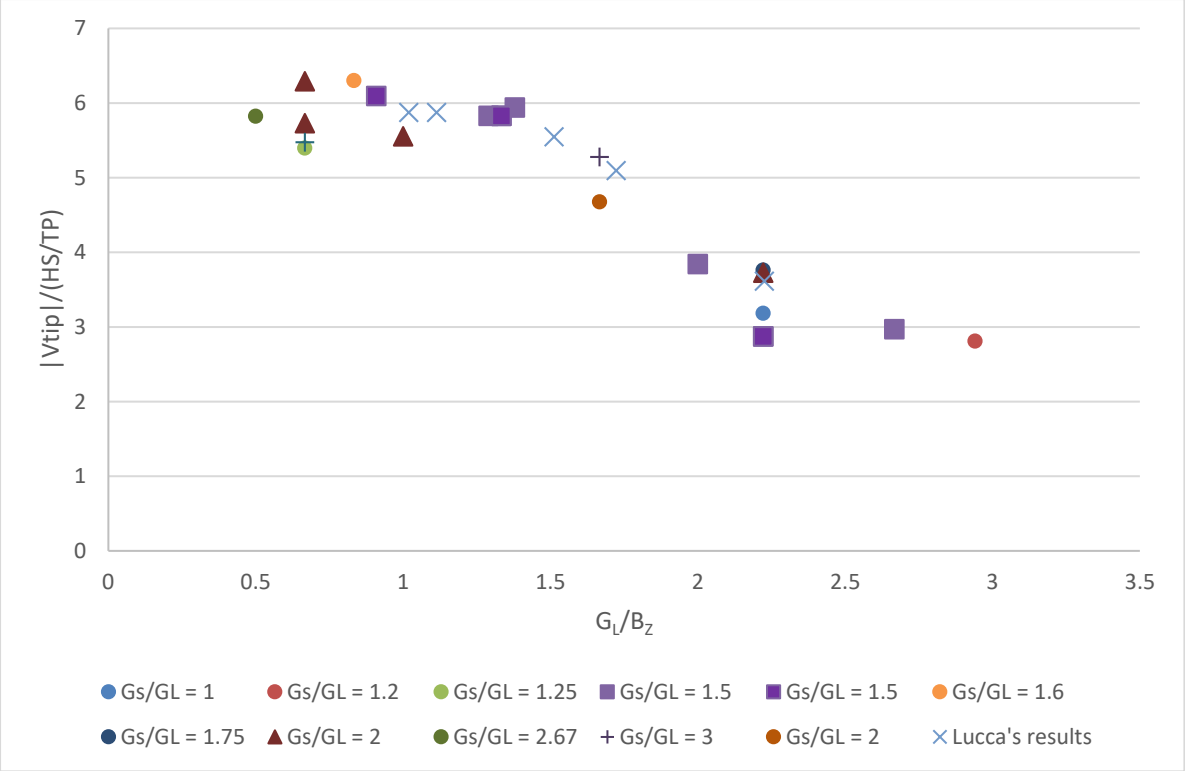

Figure 4-11: is a synthesis of the results showing how the flow constriction (G_L/B_Z) affects groyne tip velocity ($|Vtip|/(H_S/T_P)$) for groyne 1. The G_S/G_L values are shown in the figure.

The non-dimensional relationship explored in Figure 4-11 shows a trend of decreasing groyne tip velocity magnitude with an increase in the flow constriction. The same relationship exists in Lucca's results. The plot shows points resembling a straight line for low G_L/B_Z values. The curve suddenly declines to a steeper slope for G_L/B_Z greater than approximately 1.4. Flow patterns presented in section 4.3 showed a trend of recirculation eddies to form between the groynes for $G_L/B_Z > 1.4$. As previously noted, the recirculation eddies were elliptical in shape, and low velocities occurred within the eddy. This was consistent with Trampenau *et al.*, (2004) study findings of circular eddies associated with low velocities. The decline shown on the curve may be associated with eddy circulation or circulation zones. It is also important to note that circulation zones results in longer flow paths for constricted flow as a results of current peak within the groyne span, which may results in friction losses. The plot also shows G_S/G_L associated with the level of flow constriction and the tip velocity. For the upstream groyne in the field, it was established from previous flow pattern results that the G_S/G_L on the tip velocity was minimal. For very low flow constriction, the tip velocity are expected to approach zero.

Central groyne (groyne 2) results for non-dimensional parameters the G_L/B_Z, G_S/G_L and tip velocity is shown in Figure 4-12 .

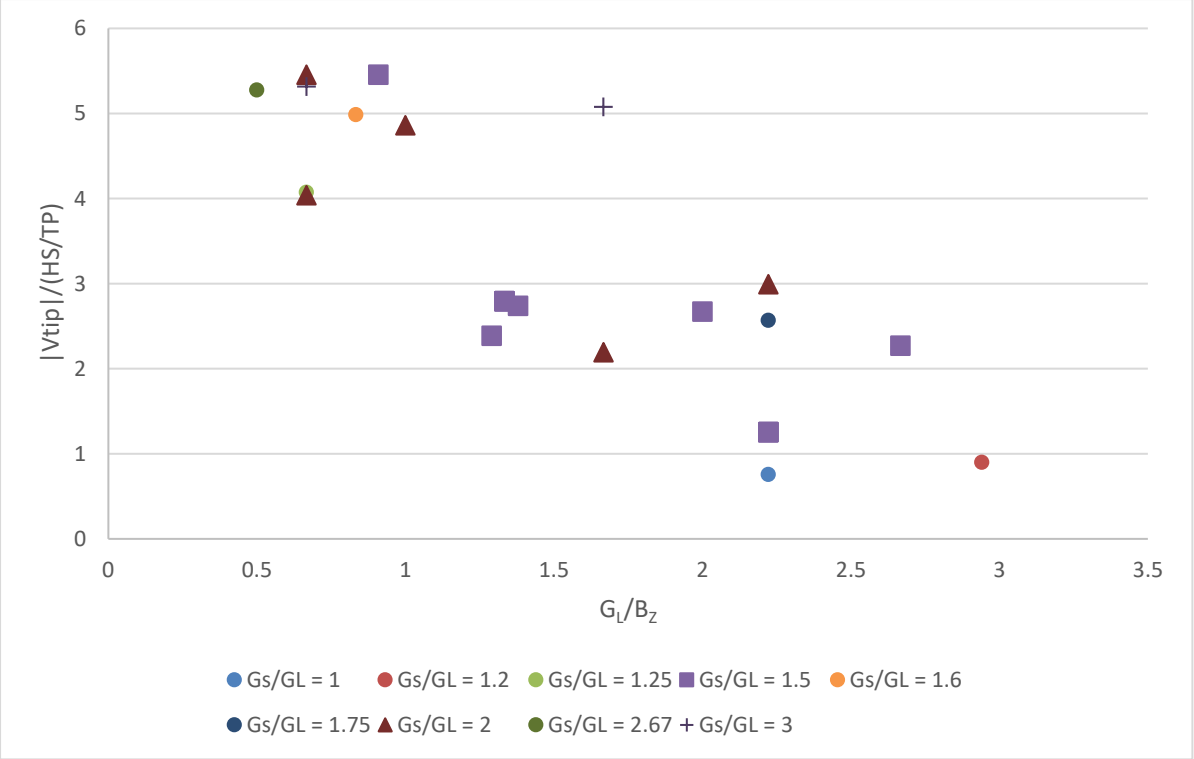

Figure 4-12: is a synthesis of the results showing how the flow constriction (G_L/B_Z) affects groyne tip velocity ($|Vtip|/(H_S/T_P)$) for groyne 2. The G_S/G_L values are shown in the figure.

It is important to note that Lucca's results were only presented together with the upstream groyne 1. The curve for groyne 2 is showing similar observation as for upstream groyne 1. High level of flow constriction results in low tip velocity and vice versa. The graph is expected to approach zero for very low flow constriction. This is due to the alongshore current reducing towards the shoreline and peaking on the breaker line as described by Bosboom & Stive, (2012) (refer to equation 3-5). Similarly to the previous curve for the upstream groyne 1, there is a sudden decline on the curve for G_L/B_Z greater 1 which is less than 1.4 from the previous curve. The decline may be associated with the eddy circulation or circulation zones again for central groyne 2. Previous results did show that the central groyne was typically experience least tip velocity magnitude compared to upstream groyne 1 and downstream groyne 3. The spreading out of the points may be associated with G_S/G_L variation. Previous results in section 4.3.4 shed that a variation of G_S/G_L results in variation of tip velocity for downstream groynes. Low G_S/G_L values are associated with low tip velocity while high values are associated with high tip velocity.

The plot shown in Figure 4-13 depict downstream groyne (groyne 3) results for non-dimensional parameters the G_L/B_Z, G_S/G_L and tip velocity.

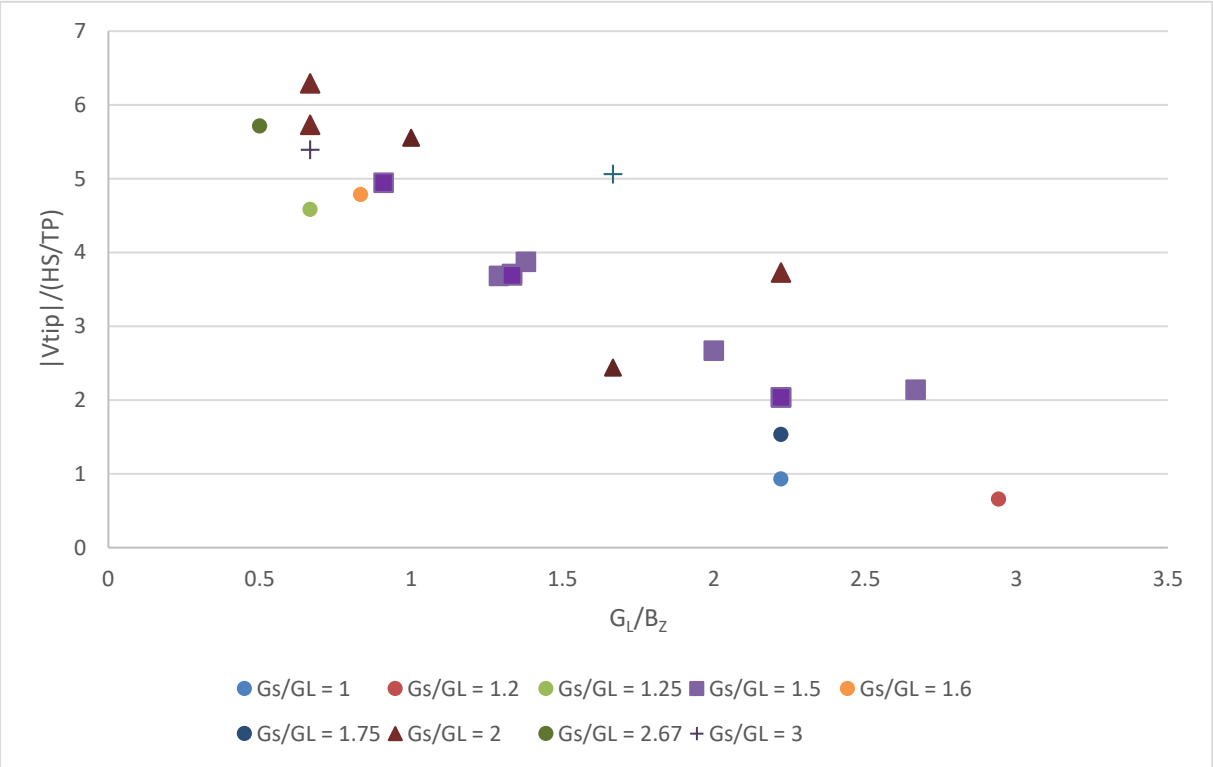

Figure 4-13: is a synthesis of the results showing how the flow constriction (G_L/B_Z) affects groyne tip velocity ($|Vtip|/(H_S/T_P)$) for groyne 3. The G_S/G_L values are shown in the figure.

The curve for downstream groyne 3 shows similar observation as for upstream groynes. The plot shows a consistent decline in the curve. The results suggest that for high flow constriction, the tip velocity approaches zero as well. Overall the relationship further reinforces flow pattern findings in section 4.3 suggesting that high groyne tip velocity is associated with low flow constriction. This is consistent with Trampaneu *et al*'s. (2004) findings for impermeable groynes. The trend further highlights risks of groyne tip local scouring associated with low levels of flow constriction. Previous results in section 4.3 showed that for high flow constriction ($G_L/B_Z > 1$), the current velocity magnitude tends to peak more toward the groyne mid span due to the breaker zone located within the groyne tip. The relationship between the tip velocity and the flow constriction shows a correlation between the two parameters (tip velocity and flow constriction). Therefore high flow constriction may not necessary imply elimination of the risk for local scour within the groyne span but may suggest lower risk of local scour on the groyne tip. It is important to note that the breaker line is where the alongshore current peaks as previously noted by Bosboom & Stive (2012).

The tip velocity direction was plotted with the flow constriction for upstream groyne (groyne 1), central groyne (groyne 2) and downstream groyne (groyne 3). Groyne 1 is shown in Figure 4-14, groyne 2 shown in Figure 4-15 and groyne 3 shown in Figure 4-16.

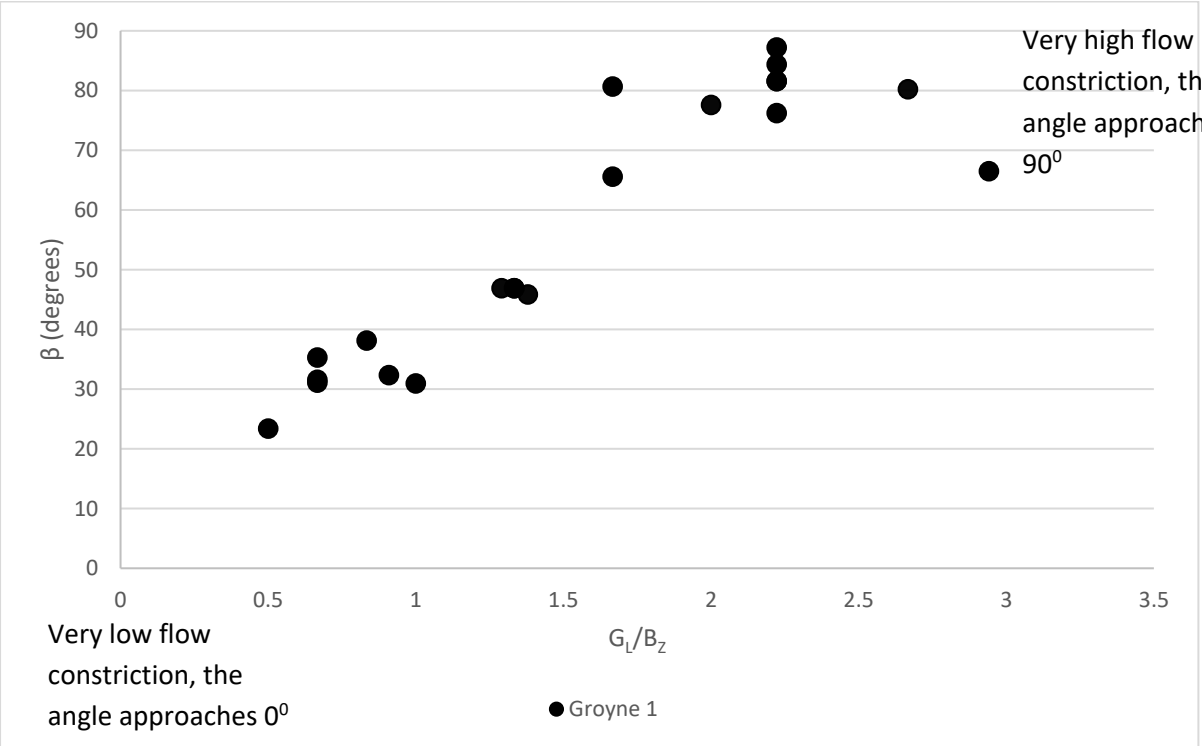

Figure 4-14: Flow constriction effect (G_L/B_Z) on the groyne tip velocity angle (β) for upstream groyne 1

The plot for the upstream groyne resembles a linear relationship between the tip velocity angle and the level of flow constriction. The plot does approach 90^0 for high flow constriction. This flow patterns results in section 4.3 are consistent with the groyne 1 velocity angle direction. For high flow constriction, rip current was evident on the upstream groyne and recirculation eddies formed on downstream groynes. For very low level of flow constriction the flow angle approaches zero. Low flow constriction could be due to very small groyne length. In that scenario, the groyne would not serve its purpose for resisting alongshore current. Bosboom & Stive, (2012) discussed in detail the alongshore current velocity as being highest along the breaker line and decaying away from the breaker line towards the shoreline.

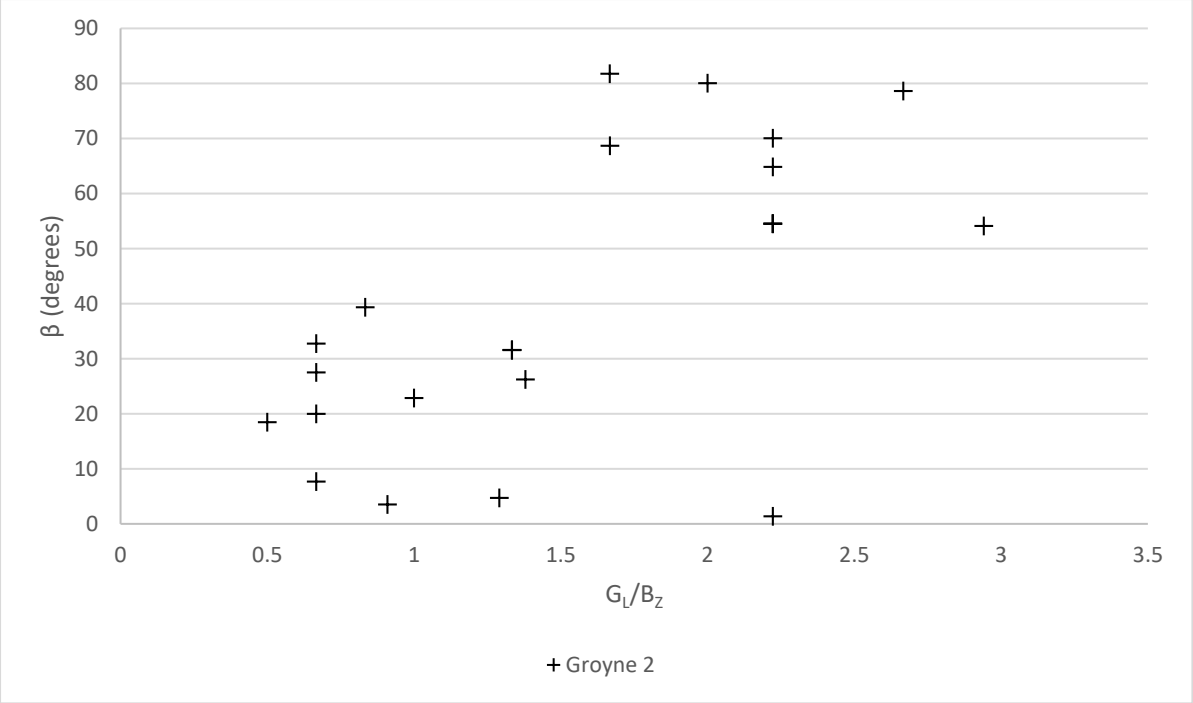

Figure 4-15: Flow constriction effect (G_L/B_Z) on the groyne tip velocity angle (β) for central groyne 2

The plot for groyne two appears dissimilar to that of groyne 1. However, the scattered data still show the above mentioned relationship between flow constriction and the tip velocity angle. G_S/G_L may be responsible for the scattering of points as it was shown previously on section 4.3.4 to affect downstream groynes in the field.

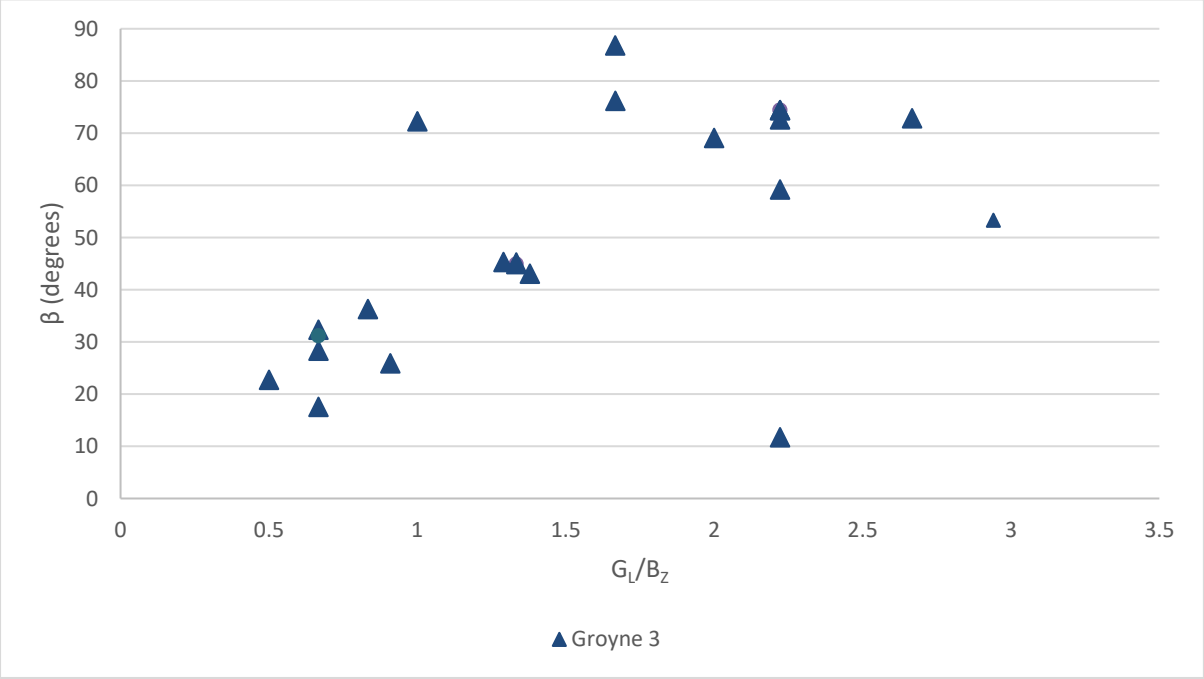

Figure 4-16: Flow constriction effect (G_L/B_Z) on the groyne tip velocity angle (β) for downstream groyne 3

The plot for groyne 3 resembled scattered data similar to groyne 2 plot. The plot shows general increases in the groyne tip velocity angle (approaching 90^0) as the flow constriction increases. This was shown to be the case for conditions where there was rip current formation and waves breaking towards the groyne midspan. The plot suggests that the groyne tip velocity is near 90^0 for $G_L/B_Z > 2$ approximately. The observation that high flow constriction results in high groyne tip velocity angle is consistent with the flow pattern presented in section 4.3. The flow pattern showed cross shore current dominating for high levels of flow constriction.

To further clarify the results, the groyne tip velocity for wave condition H_s = 1 m; T_P = 14 s; θ = $45^0/135^0$; MWL = -1 m and H_s = 2 m; T_P = 14 s; θ = $45^0/135^0$; MWL = -1 m were plotted in Figure 4-17 and Figure 4-18 respectively. The plots shown on both of the figures show groyne tip u and v velocities used to determine the groyne tip velocity magnitude and direction. The cross-shore distance (from 0 m on the groyne tip and 140 m cross shore) was non-dimensionalized using the groyne length.

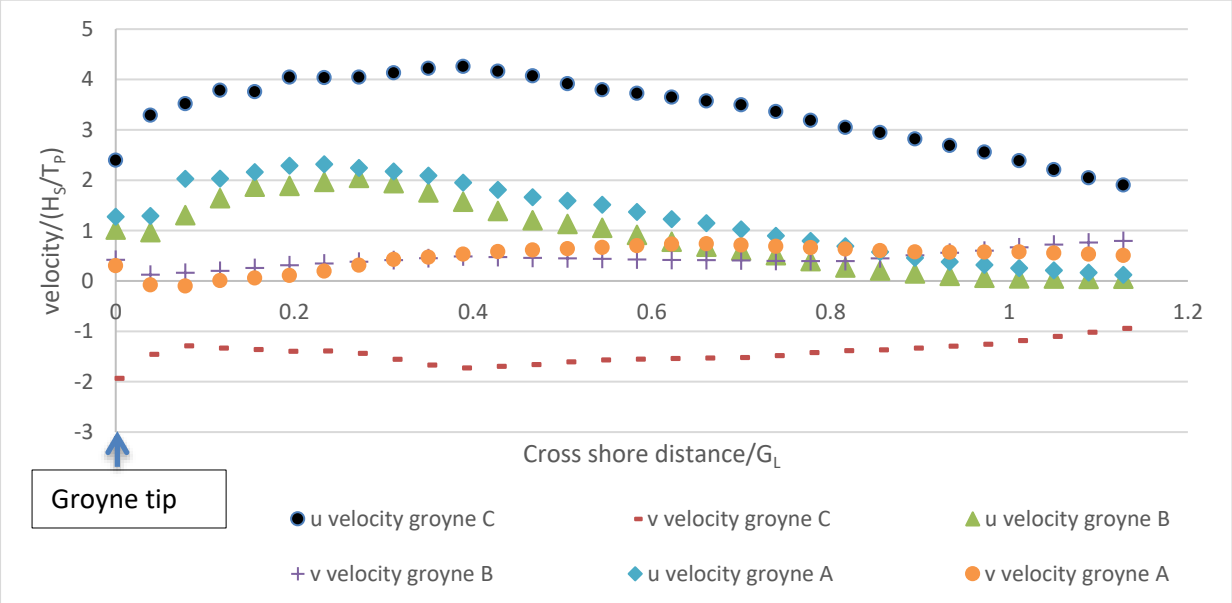

Figure 4-17: Groyne tip velocity components for wave condition H_s = 1 m; T_p = 14 s; θ = $45^0/135^0$; MWL = -1 m; G_L = 150m; B_Z = 90 m; G_L/B_Z = 1.667. The velocity was measured at the groyne tips.

The groyne tip velocity suggest predominantly cross shore flow for all the groynes. As a result, the trends show slow velocity decay with offshore distance. The rip current that developed on the groynes dissipates slowly. As shown in Figure 4-17, the u velocity for groyne C (upstream groyne) was observed to be higher compared to the downstream groynes. The figure is typical of high levels of flow constriction which often results in rip current formation. The groyne tip velocity for H_S = 2 is shown in Figure 4-18. Similar to the previous results, the velocity was plotted as a function of the cross shore distance non-dimensionalized with the groyne length.

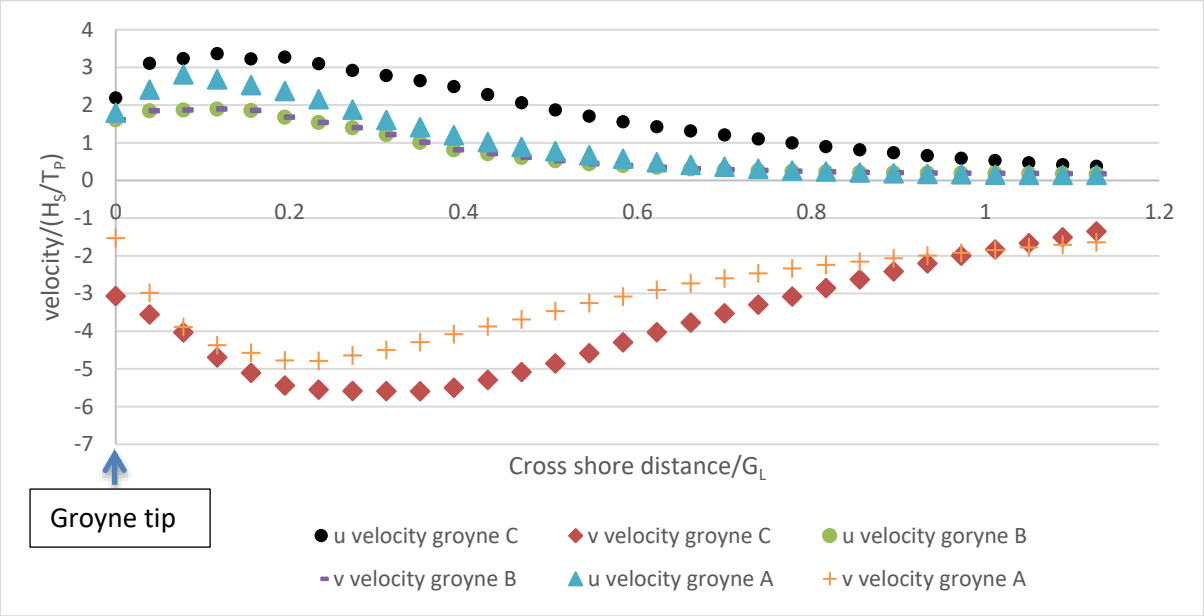

Figure 4-18: Graph showing alongshore velocity components for wave condition $\boldsymbol{H_s}$ = 2 m; $\boldsymbol{T_p}$ = 14 s; **θ** = $45^0/135^0$; *MWL* = -1; G_L = 150m; B_Z = 160 m; G_L/B_Z = 0.938. Groyne C is the upstream groyne, B central groyne and A downstream groyne.

The low flow constriction (G_L/B_Z = 0.938) for the specified wave condition suggest high groyne tip velocities. It can be seen from Figure 4-18 that the v velocity is higher than the u velocity. The higher v velocity indicates alongshore dominance which was also shown in the flow patterns depicted in Figure 4-5. Thus the velocity quickly decays.

Storm event groyne tip velocity were also plotted and is presented on Figure 4-19 for wave condition H_S = 3.5 m; T_P = 14 s; θ = $135^0/45^0$; MSL = -1 m. The u and the v velocities were obtained from the groyne tips (0 m) for groyne A (upstream groyne), B (central groyne) and C (downstream groyne) to 400 m cross shore distance.

The results for the groyne tip velocities are shown in Figure 4-19. The cross shore distance was non-dimensionalized using the groyne length.

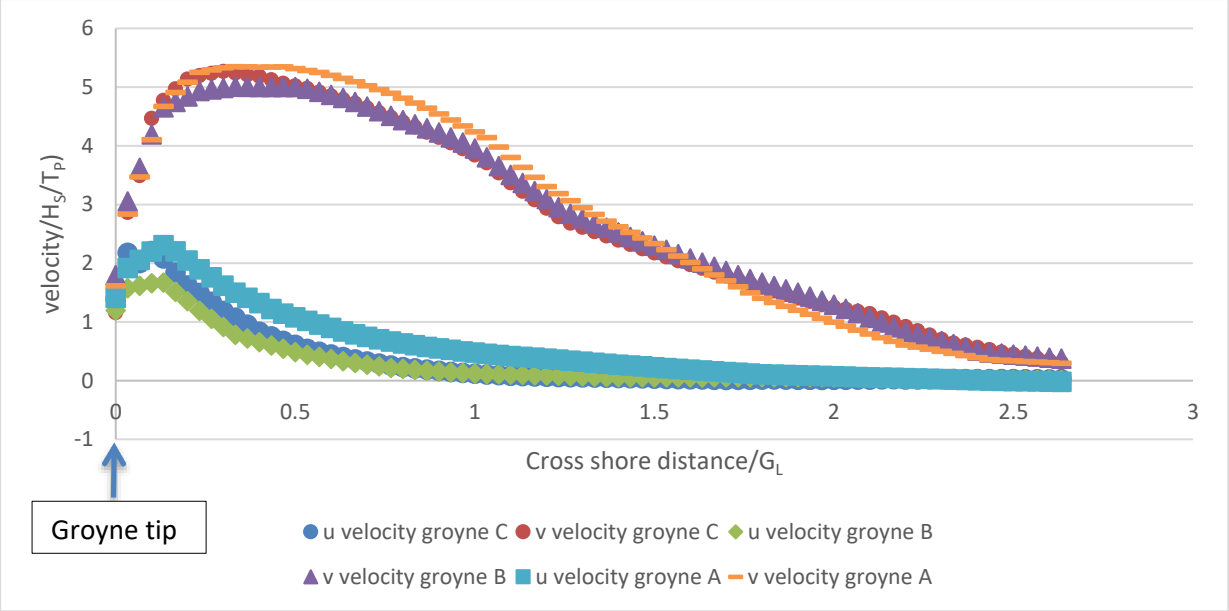

Figure 4-19: Groyne tip u and v velocity components for wave condition (H_s = 3.5 m; T_p = 14 s; θ = $135^0/45^0$; G_L = 150m; MWL = -1 m; G_L/B_Z = 0.5). Groyne A is the upstream groyne, B central groyne and C downstream groyne.

The v velocity component was higher (highest 1.335m/s) compared to the u velocity component (highest 0.577 m/s). This was due to the predominant along shore current that is shown by the flow patterns in Figure 4-9 (c). The trends show the groyne tip velocity components peak at approximately 20 to 40 m (0.133 to 0.267 m/s) from the groyne tip and a steady decay seaward away from the groyne tip. The steady decay is due the breaker line located further away from the groyne tip. As a result the peak velocity occurred away from the groyne tip.

Similar to the velocity components trends for groyne A, the v velocity component was observed to be higher compared to the u velocity component suggesting predominant alongshore current. The velocity peaked close to the groyne tip similar to groyne A (v velocity = 1.25 m/s and u velocity = 0.42 m/s).

The u, v velocity components and current speed for groyne C peaked at 1.31 m/s for v velocity and 0.59 m/s for u velocity. As previously noted, the groyne tip velocities results for the specified storm events are comparable. This strongly suggest weak current resistance by the groynes which may mean high groyne tip scouring. Furthermore, the groyne tip velocity peaked closer to the groyne tip.

4.6 Water quality implications

The flow pattern results presented in section 4.3 showed flow patterns can have different flow characteristics associated with different flow constriction and geometric parameters such as groyne spacing to groyne length ratio. It can be deduced from previous flow pattern results (section 4.3) that flow patterns and circulation zones between impermeable groynes can affect water quality. Due to the impermeability of the groynes, flushing and residence times between the groynes can be expected to be longer compared to that of permeable groynes. Eddy circulation zones found to develop between the groynes may also result in longer residence times. This implies longer time for contaminants or pollutants to be flushed out of the system.

This section aims to explore the effect of varied wave conditions, incident wave angle, water level and groyne spacing and groyne length on residence time. Residence time was determined using The residence time was computed using fresh water method described by Kenov, *et al*., (2012) for compartments between the groynes as depicted in Figure 3-3.

Table 4-15 summarizes the effect of varying the significant wave height and incident wave angle on the flow and residence time results for constant groyne spacing of 300 m

Table 4-15: The effect of varying wave conditions on the P-flux and residence time in a groyne field for constant G_S /G_L = 1.5.

H_s (m)	MWL (m)	θ Wave angle (degrees)	$\frac{G_L}{B_Z}$	$\frac{G_S}{G_L}$	Q_1 Area 1 inflow (m^3/s)	Q_2 Area 2 inflow (m^3/s)	T_{r1} Area 1 residence time (h)	T_{r2} Area 2 residence time (h)
1	0	30/150	2.667	1.500	6.807	6.772	4.897	4.922
		45/135	2.222	1.500	9.934	5.960	3.356	5.593
		60/120	2.000	1.500	10.381	8.967	3.211	3.717
2	0	30/150	1.379	1.500	15.308	15.737	2.178	2.118
		45/135	1.333	1.500	15.646	15.207	2.131	2.192
		60/120	1.290	1.500	14.171	16.427	2.352	2.029

The results show that increased low levels of flow constriction results high flow and reduction in the residence time. Higher flow rates and velocities were found to develop both on the leeward and upstream side of a groyne when significant wave heights increased from 1 m to 2 m. Section 4.2.1 showed that eddy recirculation zones develop between the groynes for $G_L/B_Z > 1.4$. The eddy circulation zones resulted in longer residence times for significant wave height of 1 m. The results also show that for low significant wave heights more oblique wave angles can increase residence time.

Studies such as Castelle *et al*., (2006), Zanuttigh *et al*., (2005) and Trampenau *et al.*, (2004) stressed the importance of groyne spacing in a groyne field as one of the important parameters in ensuring

efficient functioning of a groyne field. Section 4.3.4 showed that closely spaced groynes ($G_S/G_L < 1$) can have detrimental effects on the hydrodynamic and morphodynamic functioning of a groyne field, thus negatively affecting water quality. Table 4-16 summarizes the residence time results in a groyne field associated with varying groyne spacing and a constant wave condition.

Table 4-16: The effect of varying G_S/G_L ratio on the P-flux and residence time in a groyne field for constant $G_L/B_Z = 2$

H_s (m)	MWL (m)	θ Wave angle (degrees)	G_S/G_L	G_L/B_Z	Q_1 Area 1 inflow (m^3/s)	Q_2 Area 2 inflow (m^3/s)	T_{r1} Area 1 residence time (h)	T_{r2} Area 2 residence time (h)
1	0	60/120	1.250	2.000	10.62	6.836	2.625	4.079
			1.500	2.000	10.38	8.967	3.211	3.717
			1.750	2.000	12.69	12.35	3.078	3.162
			2.000	2.000	14.63	17.18	3.050	2.597
			2.500	2.000	15.67	15.98	3.559	3.502
			3.000	2.000	20.32	22.99	3.294	2.911

The results show that total flux increased with the increase in the groyne spacing to groyne length ratio. However, the increase resulted in a larger water volume occupying the groyne compartments. This resulted in longer residence time. Section 4.3.4 showed that the flow patterns in a groyne field do not significantly change due to varying groyne spacing. However, the results show that the recirculation eddy grew bigger with increased groyne spacing.

Section 4.4 showed the effect of storm events on the flow structure in a groyne field. It was apparent from the results that storm events are detrimental for the stability of a groyne field. High groyne tip velocities were observe to persist posing a risk of local scour. The flow patterns also showed compact eddy formation on the leeward side of all the groynes suggesting high velocity associated with efficient water circulation. Table 4-17 summarize inflow and residence time results during storm events in a groyne field.

Table 4-17: The effect of storm events on the P-flux and residence time in a groyne field

H_s (m)	MWL (m)	θ Wave angle (degrees)	G_S/G_L	$\frac{G_L}{B_Z}$	Q_1 Area 1 inflow (m^3/s)	Q_2 Area 2 inflow (m^3/s)	T_{r1} Area 1 residence time (h)	T_{r2} Area 2 residence time (h)
3.5	1	30/150	1.600	0.833	36.71	55.15	1.892	1.259
	0	30/150	2.000	0.667	33.86	42.39	1.313	1.048
	-1	30/150	2.667	0.500	28.14	29.24	0.889	0.855
3.5	1	45/135	1.600	0.833	36.30	52.50	1.913	1.323
	0	45/135	2.000	0.667	32.83	39.70	1.354	1.119
	-1	45/135	2.667	0.500	25.10	26.45	0.996	0.945

For the storm event the flow rate within a groyne field increased more than three times and the residence time reduced by more than 50% of the initial residence time observed for H_s = 1 m. The results show that high significant wave height results in high flow rates. The residence time was found to be lower for low levels of flow constriction due to lower water levels. This may also be explained by the results presented in section 4.3.2 which discuss low water levels and corresponding flow patterns. Low levels of flow constriction are associated with high groyne tip velocity which explains the shorter flushing of the system.

The residence time results showed high flow constriction may lead to longer residence times. The incident wave angle was observed to affect the water circulation within the groyne field. More oblique wave angles lead to longer residence times. However, significant wave height showed significant effect on the residence time due to low values of the flow constriction associated with high significant wave heights. The flow patterns described in section 4.3 gives a good indication of residence time in a groyne field. The resident time and eddy circulation results suggest strong dependency on the G_L/B_Z. low flow constriction associated witht compact eddy circulation results in shorter residence time while higher flow constriction associated with elliptical and recirculation eddies results in longer resident time. Therefore it can be concluded that low flow constriction results in shorter residence times and therefore more rapid mixing and better water quality.

5. SUMMARY, CONCLUSION AND RECOMMENDATIONS

This chapter summarizes the findings discussed in the previous chapter and directly addresses their relevance to the research questions outlined in chapter one. The chapter concludes with a brief discussion of limitations and assumptions made in the current study, and makes recommendations for future studies.

5.1 Summary

The results of this study show that varying wave parameters and groyne geometry results in changing flow structure patterns. Three distinct flow pattern regimes were observed in a groyne field as a result of wave conditions, and the geometric parameters G_L/B_Z and G_S/G_L.

The effects of the groyne spacing to length ratio G_S/G_L on the flow patterns, groyne tip velocity magnitude and angle was conducted in sections 4.3.4 and 4.4.1. As noted in there, an increase in the G_S/G_L ratio resulted in an increase in the groyne tip velocity magnitude and direction. The plots did show conditions where G_L/B_Z remained unchanged while the G_S was varied. For such conditions, the correlation between the G_S/G_L and the tip velocity could be established successfully. For conditions where the variation in G_S/G_L was due to G_L, it was not easy to delineate the correlation due to G_L/B_Z also being affected.

The three flow pattern regimes showed strong dependency on flow constriction. Using the Durban wave rose to gather significant wave heights data, H_S distribution and direction could be used to establish the G_L/B_Z which can then be used to ascertain occurrence frequency of the flow patterns. Durban wave data covering all four seasons is shown in Figure 1-4. The figure shows percentage distribution for various significant wave heights. The G_L was fixed at 200 m. The significant wave height was split into three ranges as shown in the Table 5-11. Using average incident wave angle of 135^0 the wave rose showed approximately 74% of the significant wave heights propagate from the south western direction (θ ~ 135^0). The results for G_L/B_Z and for a distribution of significant wave height are shown in Table 5-1.

Table 5-1: Durban wave rose data summary for H_S and associated G_L/B_Z

H_S (m)	G_L (m)	B_Z (m)	G_L/B_Z	Distribution %
0 – 1.5	200	0 -112	$G_L/B_Z \geq 1.79$	52
1.5 - 2.5	200	112 – 187	$1.79 \geq G_L/B_Z \geq 1.09$	42
>2.5	200	>187	$1.09 \geq G_L/B_Z$	6

The results in the table were linked to the flow patterns and the distribution percentage for each significant wave range. The G_L/B_Z for each H_S range was associated with the flow pattern regimes to establish the occurrence frequency.

a) Flow pattern structure 1 ($G_L/B_Z \geq 1.4$)

Flow pattern structure 1 was observed to develop within the groyne field when the flow constriction is high ($G_L/B_Z \geq 1.4$). The pattern was apparent when the breaker zone width was shorter than the groyne length and the breaker zone located towards the midspan of the groyne. The flow structure was found to be typical for wave conditions where the significant wave height was small (i.e. H_S = 1 m). It was observed that the eddy recirculation tended to shrink in size when the G_S/G_L ratio decreased and grew bigger with the increase in the ratio. A schematic for the flow pattern structure is depicted in Figure 5-1.

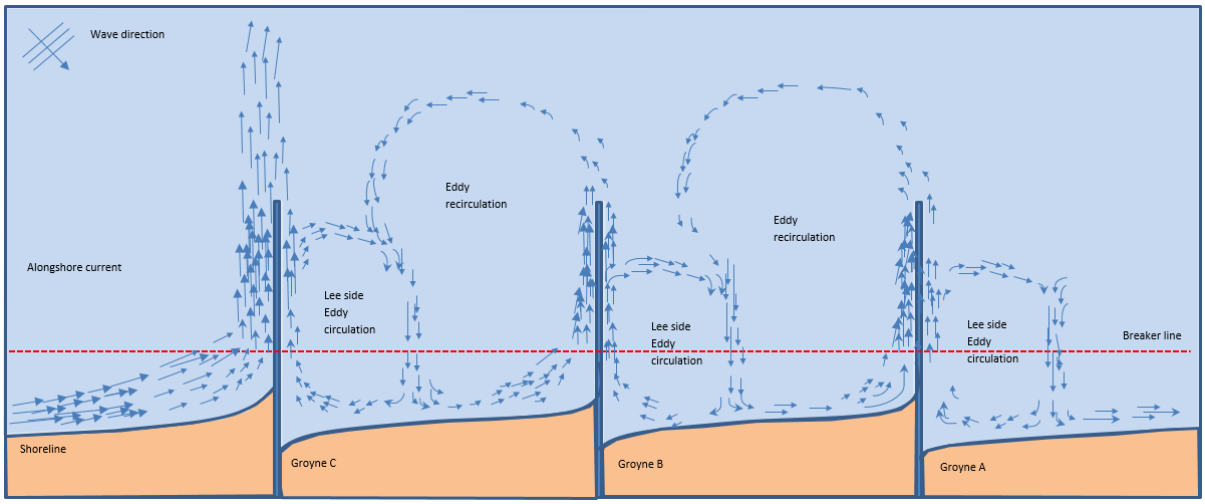

Figure 5-1: Schematic flow pattern structure 1 for an impermeable groyne field. The wave direction is depicted on the figure. For simplicity, the red dotted line indicates the breaker line where majority of the waves would break. The groynes in the field experienced rip current on both sides due to the diversion of the alongshore current seaward and the eddy circulation formation on the leeward side. Peak rip current was typically observed to occur on the upstream of the first groyne in the field and the downstream groynes experienced lower velocity. Eddy circulation zones were observed to develop between the groynes.

The upstream groyne in the system (Groyne C) was found to develop high cross shore current speeds (rip current) on the upstream side. The variation in G_L/B_Z and G_S/G_L affected downstream groynes

greatly compared to Groyne C. The increase in G_L/B_Z values resulted in groyne tip velocity increase and diminished the recirculation eddies when the ratio was less than 1.4. The current cross shore speed was found to be between 0.2 – 0.5 m/s and the peak current speed was observed on the updrift side of the groyne C. The rip current observed on the first groyne was consistent with the findings of Lucca, (2013) and Pattiaratchi *et al.*, (2009) for similar wave conditions. The groyne tip velocity showed cross shore dominant direction (β approaching 90^0). The wave angle ranged from 53^0 - 82^0. This was the case for all the groynes in the field. The increase in G_L/B_Z resulted in reduction in the β. The first groyne was also observed to shelter the downstream groynes particularly for low G_S/G_L conditions (< 1.2). Low G_S/G_L conditions also showed high groyne tip velocity for upstream groyne (groyne C) and low groyne tip velocity for downstream groynes. Furthermore, the flow patterns depicted circulation zones and confinement between the groynes. This showed high residence time suggesting poor flow circulation between the groynes. The circulation zones were found to adversely affect water quality. Sediment is thus likely to be retained within the groyne compartment and only escape from the system through the rip current. The long term effect may be negative morphological evolution of the near shore zone, accretion upstream and erosion of beaches downstream. Furthermore, the first groyne may experience local scour due to it being the mainly effective groyne. The flow structure 1 is associated with $G_L/B_Z \geq 1.79$ from Table 5-1 and occurrence frequency percentage of 52. The results suggest that flow structure 1 is more expected for the Durban coast compared to the other flow structure patterns.

b) Flow pattern structure 2 ($1 \leq G_L/B_Z \leq 1.4$)

Flow pattern structure 2 was found to develop for $1 \leq G_L/B_Z \leq 1.4$. The increase in the significant wave height affected the breaker zone width; the breaker line moved seaward towards the groyne tip. The flow constriction reduced and the flow pattern of Figure 5-2 was observed. The flow pattern consisted of lee side eddy formation on all the groynes.

Figure 5-2 depicts flow pattern structure 2 and the position of the breaker line.

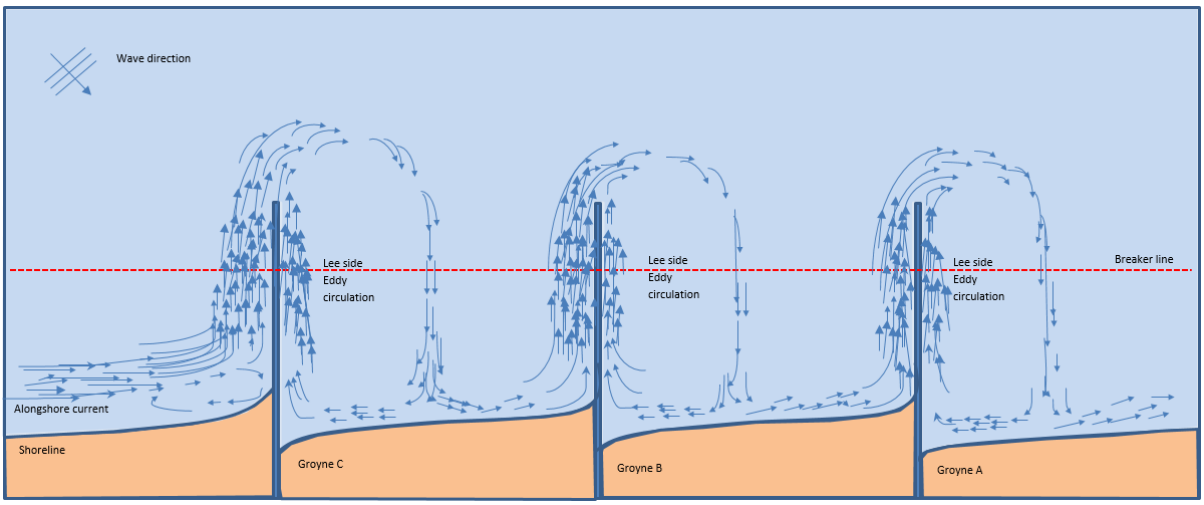

Figure 5-2: Schematic flow pattern structure 2 for an impermeable groyne field. The wave direction is depicted on the figure. For simplicity, the red dotted line indicates the breaker line where majority of the waves would break. Bigger and more circular eddies were observed to form on the leeward side of all the groynes. However, the first groyne (groyne C) in the field typically experienced the biggest eddy circulation compared to the rest of the groynes.

The lee side eddies were observed to be elliptical in shape. The breaker line moved offshore within the groyne length as a results of G_L /B_Z reduction. The peak current moved accordingly and was found to be high on both sides of the groynes; between 0.5 - 1 m/s, and often peaked on the leeward side towards the tip of the groyne. The groyne tip velocity magnitude increased and the flow formed an eddy. As a result, the velocity angle ranged from 23^0 - 47^0 suggesting a predominant alongshore current. Similarly to the previous flow structure 1, the low G_S/G_L resulted in low tip velocity for downstream groynes and confined flow between the groynes. High G_S/G_L showed high tip velocity. The increase evident throughout the groynes and was comparable on all the groynes for G_S/G_L = 3. This suggests groyne isolation reinforcing the importance of optimum groyne spacing. The eddy circulations reduced in size for downstream groynes. The flow pattern was less constricted than for flow structure 1 and the circulation zones disappeared. The flow structure 2 experienced shorter residence time compared to flow structure 1 due the absence of recirculation patterns. Due to increased groyne tip velocity, the specified flow pattern may be prone to groyne tip local scour for all the groynes compared to the previous flow structure 1. Flow structure 2 may be associated with significant wave height distribution of 42% from Table 5-1. Therefore also showing high percentage of occurrence.

c) Flow pattern structure 3 (G_L /$B_Z \leq 1$)

Flow pattern structure 3 was observed to develop for low levels of flow constriction associated with high significant wave heights (G_L /$B_Z \leq 1$). This was the case for high significant wave height ($H_S \leq 3$ m. The structure developed due to the position of the breaker line at the groyne tip and at times beyond the groyne length. Figure 5-3 depicts flow pattern structure 3

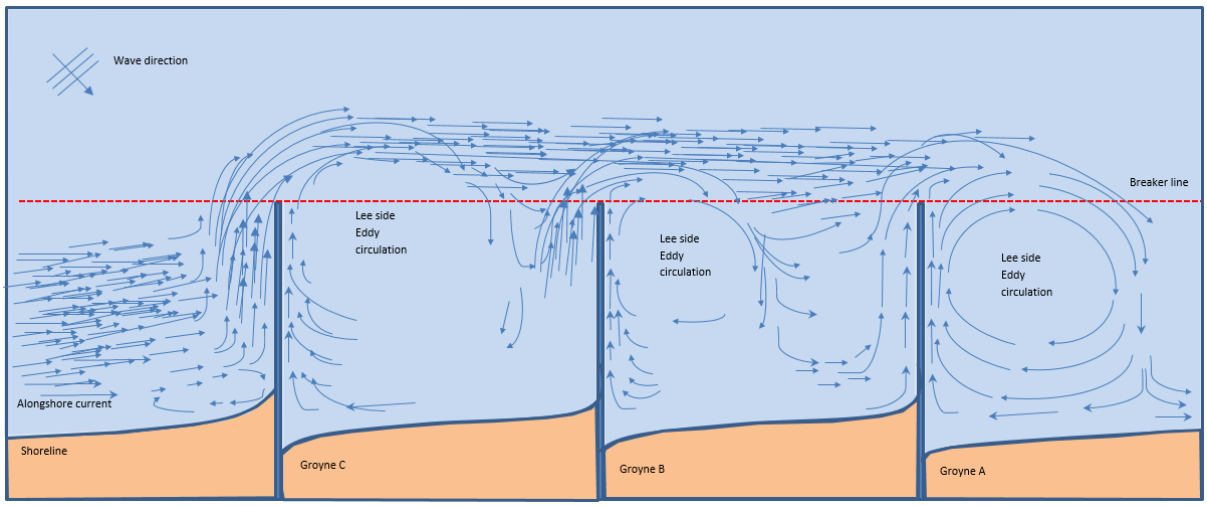

Figure 5-3: Schematic flow pattern structure 3 in an impermeable groyne field. The wave direction is depicted on the figure. For simplicity, the red dotted line indicates the breaker line where majority of the waves would break. Bigger and more circular eddies were observed to form on the leeward side of all the groynes. However, the first groyne on the field typically experienced the biggest eddy circulation compared to the rest of the groynes.

The eddy circulations on the lee side of all three groynes were found to be compact, consisting of high current speeds (0.8 - 1.4 m/s). The low flow constriction resulted in increase in the groyne tip velocity The velocity direction was found to range from 4^0 - 35^0 suggesting predominant alongshore current. The current speed was found to peak towards the groyne tip and mainly alongshore. The flow mostly bypassed the groyne compartments particularly for low G_S/G_L. The higher the ratio, the more the groyne were isolated. Upstream groyne was mostly exposed due to the alongshore diversion. Residence time was found to be shorter for flow structure 3 due to high flow rate and velocity. The current speed within the eddy may result in erosion on the lee side of the groyne and accretion upstream. Due to the resulting modelled high velocities, it is surmised that this flow structure may be associated with high rates of beach erosion and local scouring within the groyne structure. The flow structure was infrequent (a distribution of 6%) compared to other flow pattern regimes. This is due to the flow pattern associated with low G_L/B_Z of less than 1. The low flow constriction is associated with high tip velocities and storm events.

The local scouring on the groyne tips is shown on Figure 5-4 and discussed in the context of the results.

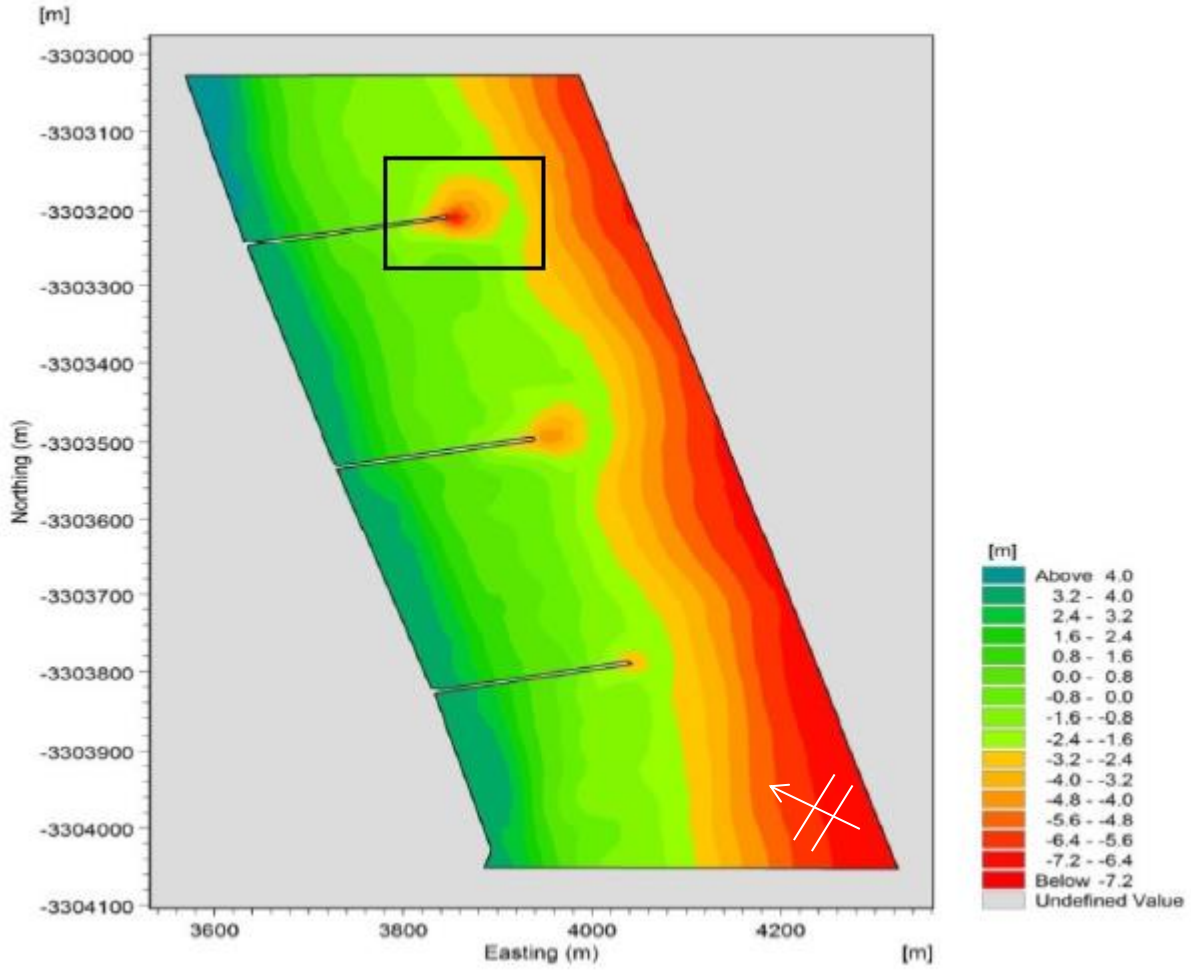

Figure 5-4: beach contours and scouring bathymetry for Durban groynes adapted from Lucca (2013) Figure 1.4. The bathymetry was developed on MIKE 21 Mesh generator. The highlighted area show Bay of Plenty groyne tip where scouring appear to be worse compared to the other groynes upstream.

The local scouring on the groyne tips is worse for the downstream groynes and better for upstream. Results in section 4 showed that the upstream groyne is more likely to experience local scour failure due to it venerability as it is first groyne to resist the alongshore current. However as it is shown in Figure 5-4 from field data, this is not the case. The harbor break water may be sheltering the upstream groynes, leaving the downstream groyne exposed. Literature (i.e. Trampenau *et al.*, 20004) noted that upstream groyne in a field typical gets exposed to higher current velocity compared to downstream groynes due to alongshore current diversion particularly for impermeable groynes. The results in section 4 are in agreement with this notion. The upstream groyne in the field experienced highest current velocity compared to the downstream groynes.

Data plotted in chapter 4 was consolidated using dimensional analysis and is presented here as plots of tip velocity against flow constriction, and flow constriction against tip velocity angle. These plots are shown in Figure 5-5 and Figure 5-6.

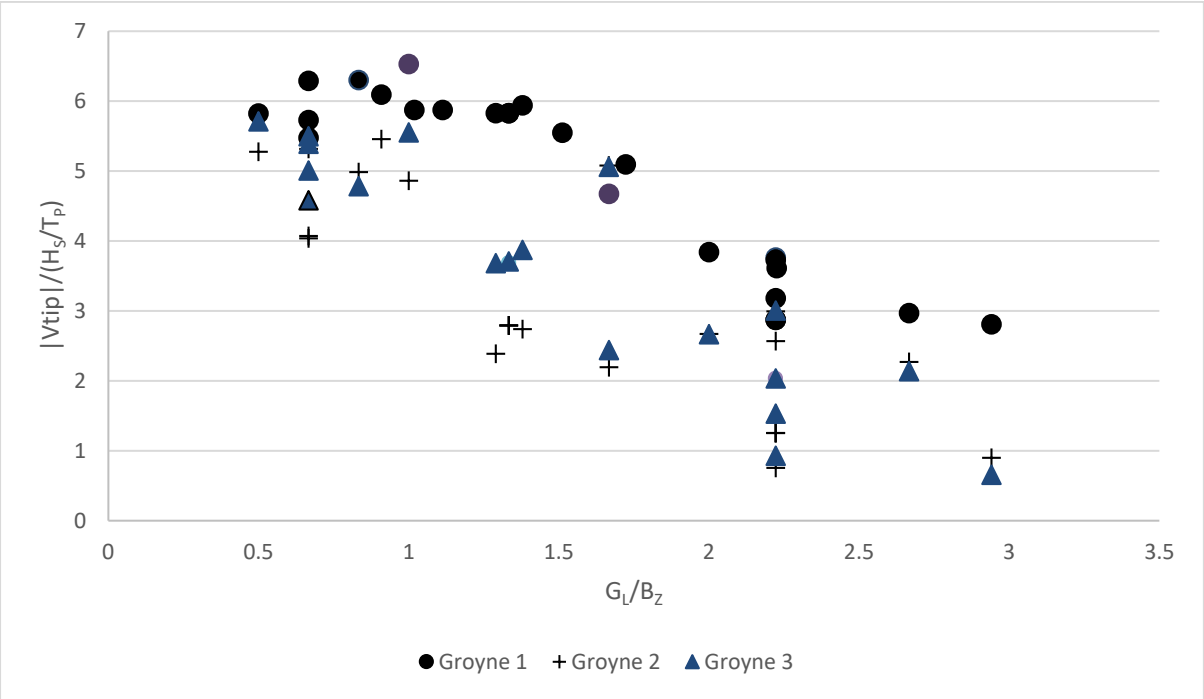

Figure 5-5: Flow constriction effect (G_L/B_Z) on the groyne tip velocity angle (β) for groynes in a field. Upstream groyne 1 (solid circle), central groyne 2 (cross) and downstream groyne 3 (triangle)

The consolidated plot strongly suggests a correlation between the tip velocity and the flow constriction. The plot decline with the increase in the flow constriction may be associated with dissipation effect due to long term flow paths associated with eddy recirculation and momentum as a result of slow moving flow shown to exist for elliptical eddy circulation. Recirculation eddies and recirculation zones were shown in section 4.3 to exist. Friction losses were considered but deemed minimal for such tip current variation.

Presenting the data in the non-dimensional format universal consolidated the data and gave a comprehensive perspective on groyne tip velocity for groynes in a field. Thus making it applicable plot for groynes tip velocity plotted against flow constriction. However, there are limitation noted by Bosboom & Stive (2012) in the equation 3-5 used for velocity scaling. The limitations included the constant beach slope and constant wave period.

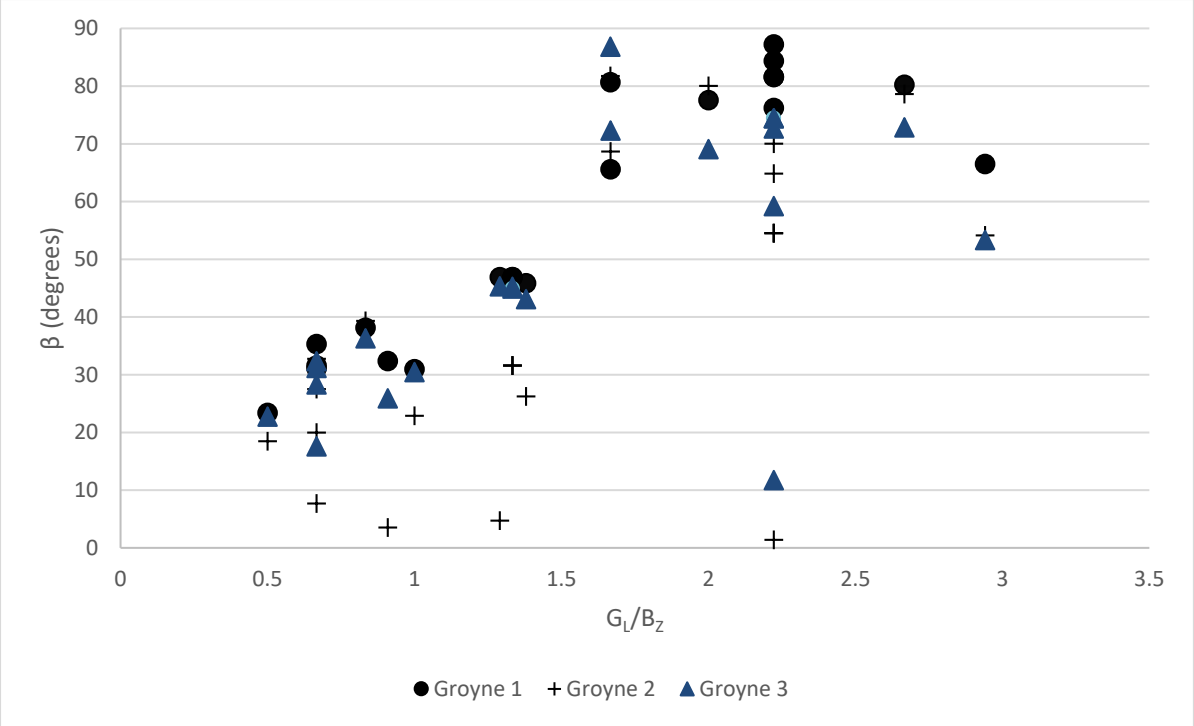

Figure 5-6: Flow constriction effect (G_L/B_Z) on the groyne tip velocity angle (β) for groynes in a field. Upstream groyne 1 (solid circle), central groyne 2 (cross) and downstream groyne 3 (triangle)

The dimensional analysis of Figure 5-5 showed high G_L /B_Z to result in low scaled groyne tip velocity and low G_L /B_Z results in high tip velocity. As previously stated, this is consistent with Trampaneu *et al.*'s (2004) findings. The groyne tip velocity angle in Figure 5-6 increased with the increase in the flow constriction. This was expected since previous studies such as Trampenau *et al*., (2004), Lucca, (2013) and Walker *et al*., (1991) alluded to high levels of flow constriction associated with rip current or cross shore current. The flow constriction showed stronger effect on the flow structure throughout the groyne field. Scaling the results more clearly delineated geometric effect on the field and their effect. G_S/G_L showed the effect on the groyne tip velocities. This was evident when the G_S was increased. Although not possible to quantify accurately, it is the author's opinion that flow constriction was the principle contributor. The overall results clarify some of the challenges associated with impermeable groynes. Challenges such as local scouring, groyne spacing and groyne length effect on the function of a groyne field. The findings are now consolidated to address the research questions

5.2 Research questions

How are the flow patterns around impermeable groynes affected by wave conditions and groyne spacing?

The results from this study's numerical model show that wave conditions significantly affect flow patterns that develop within a groyne field. This was found to be the case for a single groyne in previous studies such as Lucca (2013) and Pattiaratchi *et al*., (2009). High, storm event significant wave heights

can cause strong alongshore currents to develop around the groyne tip and an overall increase in velocities within a groyne field. The flow constriction ratio G_L/B_Z developed by Tarnowska (1985) can be used to classify flow patterns and delineate three distinct flow structures observed within a groyne field. Trampenau *et al*., (2004) found similar flow patterns to those shown in Figure 5-2 and Figure 5-3 to develop within a groyne field. However, his study did not describe flow pattern structure 1 depicted by Figure 5-1. Lucca, (2013) only modeled a single impermeable groyne thus would not have been able to ascertain the circulation zones that develop within a groyne field. Due to waves breaking more shoreward for $G_L/B_Z \geq 1.4$, recirculation patterns were found to develop within the groyne field. The flow was predominantly cross shore resulting in rip current formation on both sides of each groyne. Eddy circulation zones were found to be associated with longer residence time and reverse flow for downstream groynes. For similar waves condition acting on a single impermeable groyne, the alongshore current is able to re-establish downstream of the lee side eddy, thus no recirculation pattern was observed in previous studies such as Lucca (2013) and Pattiaratchi *et al*., (2009). There was little effect on the flow pattern induced by varying groyne spacing within a groyne field. However, the groyne tip velocities was significantly affected by the groyne spacing variation although some of the variation can be associated with the G_L/B_Z ratio. It was observed that the flow pattern consisted of a groyne leeside eddy and eddy recirculation which was bigger than the lee side eddy circulation for wave conditions where eddy recirculation developed. The recirculation eddy did not disappear due to an increase in inter-groyne spacing increase, however groyne tip velocities increased on both sides of the groyne. Increasing inter-groyne spacing showed shorter residence time, indicating good flushing. However, this did show higher current speeds for downstream groynes. This was due to groynes starting to perform in isolation.

What are the possible implications on sediment transport, erosion and accretion?

Significant erosion and accretion can occur for high wave conditions such as storm events. High significant wave heights increase velocities within the groyne field, together with the overall alongshore current. These high velocities can pose a risk to the structural stability of the groynes and to their efficiency in retaining sediments. This study found that for all types of flow patterns that can develop within a groyne field, a saw-tooth shoreline may occur within a groyne field. Flow pattern structure 1 showed strong rip current to develop on the first groyne on the field. This may result in sediment lost out to sea due to rip current, therefore creating sediment deficit downstream. This could lead to both scouring on the first groyne and erosion of beaches downstream. Flow pattern structure 2 showed alongshore current dominant system with leeside eddy circulation formation. The eddy circulation does create high velocities on the groyne tip and along the groyne which may be associated with erosion and scouring. The groyne upstream showed high water surface elevation and low velocities which may be associated with sediment accretion. Also showed continuous flow which minimize sediment lost out to sea. Flow pattern structure 3 showed very high velocities across the groyne field. Some of the flow

bypassed the groyne compartment, creating a high velocities flow path along the groyne tips. This flow pattern structure was found to be critical for groyne structural integrity reduction due to high velocities.

This study's findings and existing literature strongly suggest that impermeable groynes face a greater risk of local scouring, erosion and accretion compared to their permeable (or semipermeable) counterparts.

5.3 Recommendations

The limited availability of field data on the Durban groyne field was a major limitation for this study. The field investigation conducted by Lucca, (2013) focused on the Bay of Plenty groyne, limiting perspective of the flow patterns and velocities that can develop within the groyne field. However, the field study did show strong rip current developing around the groyne for both high and low tide conditions. This suggested that the groynes have low permeability especially for low water level, thus performing more like impermeable groynes. This might be due to the rock infill between the reinforced concrete piles. One of the advantages of rock infill within the piles is for high water level and significant wave height, the permeability in the groyne is effectively increased, thus reducing the risk of accretion and erosion. Field studies that extend current measurements across the whole groyne field would validate flow patterns and eddy recirculation within a groyne field, it is therefore recommended for further study to have current meters across the entire groyne field. The use of Lagrangian measurements (e.g. tracking floats) is further recommended in conjunction with current meters. Such a study would conclusively determine the flow patterns, velocity components and residence times within the groyne field. Field study conducted by Lucca, (2013) did include the effect of the harbor breakwater effect, however does not show the full perspective of the entire groyne field as a result of the sheltering effect provided by the breakwater. The sheltering effect is evident on Figure 5-4 as upstream groynes experience worse deterioration compared to downstream groyne (Bay of Plenty). As previously stated on section 5.1, the pattern of deterioration is in contrast to Trampenau's *et al*. (2004) and the modelled result findings. Therefore it is strongly recommended for future models to comprehensively encompass the breakwater effect on the overall efficiency of the groyne field. The results would assist in efficiently nourishing the beaches and further assist with calibration of future models.

The present study has shown that in an impermeable groyne field, the first groyne in the field is exposed to high velocities particularly at the tip compared to the remaining downstream groynes. Local scouring may therefore be greater on the first groyne compared to the rest of the groynes in the field. This finding further affirms literature recommendation of the use of permeable groynes compared to impermeable groynes. Varying the groyne permeability within a field and along the groyne may alleviate local scouring challenges. Storm conditions showed high velocities path can develop across the groyne tips which may result in severe scouring at the groyne tips. It is therefore recommended for future studies explore ways to better protect the groynes from scouring during storm conditions. This could include

the use of well-established scour protection methods such as rock infill used for breakwater heads. Such methods may prove beneficial to preserve structural integrity during storm conditions. However they could also adversely affect the normal flow around the groyne.

Bibliography

Andrew, M., Suzana, I., Mike R, J. & Duncan, W., 2013. MORPHOLOGICAL EVOLUTION AROUND A GROYNE STRUCTURE AT CLEVELEYS BEACH, NORTHWEST ENGLAND, DURING A RANGE OF WAVE CONDITIONS. *Proceedings of Coastal Dynamics 2013,* pp. 1195-1206.

Bakker, W. et al., 1984. *Permeable groynes: Experiments and practice in the Netherlands.* Texas, Proceedings, Nineteenth International Conference on Coastal Engineering.

Ballard, C., 1991. *Guidelines for stabilising waterways.* Australia: The standing committee on rivers and catchments.

Barnett, K. A., 1999. *The Management of Durban's beaches: an historical perspective. Proceedings, 5th International Conference on Coastal and Port Engineering in Developing Countries.* DURBAN, COPEDEC V.

Barnett, K. A., 2011. *THE IMPACT OF THE DURBAN HARBOUR ENTRANCE ON THE DURBAN SHORELINE.* STELLENBOSCH, BARNETT POZNANSKI & ASSOCIATES CC.

Battjes, J., 1972. Set-up due to irregular waves, in Proceedings of the 13th International Conference on Coastal Engineering. *American Society of Civil Engineers,* pp. 1993-2004.

Battjes, J. & Janssen, J., 1978. Energy Loss and Set-up due to Breaking of Random Waves. *Coastal Engineering,* pp. 569-587.

Battjes, J. & Stive, M., 1985. Calibration and Verification of a Dissipation Model for Random Breaking Waves. *Journal Of Geophysical Research,* 90(C5), pp. 9159-9167.

Bing-chen, L., Hua-jun, L. & Jing, Z., 2010. Study of wave induced radiation stress and vertical mixing. *Science direct,* 22(5), pp. 97-100.

Bosboom, J. & Stive, M. J., 2012. *Costal Dynamics 1 lecture notes CIE 4305.* Netherlands: VSSD.

Broker, I. et al., 2003. MORPHOLOGICAL MODELLING: A TOOL FOR OPTIMISATION OF COASTAL STRUCTURE. *Coastal Engineering Today.*

Castelle, B. et al., 2006. Dynamics of wave-induced currents over an alongshore non-uniform multiple-barred sandy beach on the Aquitanian Coast, France. *Continental Shelf Research,* Volume 26, pp. 113-131.

Chen, Y.-Y. & Li, M.-S., 2015. Evolution of breaking waves on sloping beaches. *Coastal Engineering,* Volume 95, p. 51–65.

Corbella, S. & Stretch, D. D., 2012a. Predicting coastal erosion trends using non-stationary statistics and process-based models. *Coastal Engineering,* Volume 70, pp. 40-49.

Corbella, S. & Stretch, D. D., 2012b. The wave climate on the KwaZulu-Nata lcoast of South Africa. *JOURNAL OF THE SOUTH AFRICAN INSTITUTION OF CIVIL ENGINEERING,* 54(2), pp. 45-54.

Corbella, S. & Stretch, D. D., 2012c. Decadal trends in beach morphology on the east coast of South Africa and likely causative factors. *Natural Hazards and Earth System Sciences,* Volume 12, pp. 2515-2527.

Corbella, S. & Stretch, D. D., 2014. Directional wave spectra on the east coast of South Africa. *Journal of the South African Institution of Civil Engineering,* 56(3), pp. 53-64.

de Brauwere, A., de Brye, B., Blaise, S. & Deleersnijder, E., 2011. Residence time, exposure time and connectivity in the Scheldt Estuary. *Journal of Marine Systems,* Volume 84, pp. 85-95.

Dean, R. G. & Dalrymple, R. A., 2004. *Coastal Processes With Engineering Applications.* University of Cambridge ed. Cambridge: University of Cambridge.

DHI, 2012a. *MIKE 21 FLOW MODEL FM Hydrodynamic Module,* Denmark: DHI.

DHI, 2012b. *MIKE 21 SW: SPECTRAL WAVES FM MODULE,* Denmark: DHI.

DHI, 2012c. *MIKE ZERO: Creating 2D Bathymetries,* Netherlands: DHI.

Duan, J. G. & Nanda, S., 2006. Two-Dimensional Depth-Averaged Model Simulation of Suspended Sediment Concentration Distribution in a Groyne Field. *Joarnal Of Hydrology,* Volume 327, pp. 426-437.

EMS, 2016. *Environmental Mapping and Surveying.* [Online]
Available at: http://www.enviromap.co.za/
[Accessed 16 October 2016].

Fleming, C. & Hunt, J., 1976. Application of a sediment transport model. *Proceedings of 15th Coastal Engineering Conference,* pp. 1184-1202.

Goda, Y., 1975. Irregular wave deformation in the surf zone. *Coastal Engineering in Japan,* Volume 18, pp. 13-26.

Guza, R. T., 1983. Transformation of Wave Height Distribution. *JOURNAL OF GEOPHYSICAL RESEARCH,* 88(10), pp. 5925-5938.

Hawkins, S. J., H.F, B., Barbara, Z. & Alberto, L., 2007. *Environmental Design Guidelines for Low Crested Coastal Structures.* 1st ed. United kindom: Elsevier's Science & Techncology Oxford.

Holthuijsen, J., Booij, N. & Herbers, T., 1989. A prediction model for stationary, short-crested waves in shallow water with ambient currents. *Coastal Engineering,* Volume 13, pp. 23-54.

Huayong, X., Zongwan, X. & Liangsheng, Z., 2004. Vertical variation in radiation stress and wave-induced current. *Coastal Engineering,* Volume 51, p. 309–321.

Jing-xin, Z. & Hua, L., 2010. Currents induced by waves in the surf zone and the pollutant transport analysis. *Journal of Hydrodynamics,* 22(5), pp. 1033-1038.

Johnson, H. K. et al., 2005. Modelling of waves and currents around submerged breakwaters. *Coastal Engineering,* Volume 52, pp. 949-969.

Kenov, I. A., Garcia, A. C. & Neves, R., 2012. Residence time of water in the Mondego estuary (Portugal). *Estuarine, Coastal and Shelf Science,* Volume 106, pp. 13-22.

Komen, G. et al., 1994. *Dynamics and Modelling of Ocean Waves.* Cambridge: Cambridge University Press.

Kumar, N., Voulgaris, G. & Warner, J., 2011. Implementation and modification of a three-dimensional radiation stress formulation for surf zone and rip-current applications. *Coastal engineering,* Volume 58, pp. 1097-1117.

Lee, J.-T.et al., 2011. A depth-averaged two-dimensional model for flow around permeable pile groins. *International Journal of Physical Sciences,* 6(6), pp. 1379-1387.

Longuet-Higgins, M., 1970. Longshore Currents Generate By Obliquely Incident Sea Waves. *JOURNAL OF GEOPHYSICAL RESEARCH,* 75(33), pp. 6778-6789.

Longuet-Higgins, M. & Stewart, R., 1964. Radiation stresse in water waves; a physical discusion with applications. *Pergamon Press Ltd,* Volume 11, pp. 529-562.

Lucca, P. A., 2013. *FLOW PATTERNS AROUND GROYNES IN THE COASTAL ZONE,* Durban: University of KwaZulu-Natal.

Mingxiao, X., 2011. Establishiment, validation and discussions os a three dimensional wave-induced current model. *Ocean modelling,* Volume 38, pp. 230-243.

Muir Wood, A. & Fleming, C., 1981. *Coastal Hydraulics.* 2nd ed. Hong Kong: The Macmilan Press LTD.

Olij, D. J., 2015. *Wave climate reduction for medium term process based morphodynamic simulations with application to the Durban coast,* Netherlands: s.n.

Ouillon, S. & Dartus, D., 1997. THREE-DIMENSIONAL COMPUTATION OF FLOW AROUND GROYNE. *Journal of hydraulic engineering,* 123(11), pp. 962-970.

Pattiaratchi, C., Olsson, D., Hetzel, Y. & Lowe, R., 2009. WAVE-DRIVEN CIRCULATION PATTERNS IN THE LEE OF GROYNES. *Continental Shelf Research,* Volume 29, pp. 1961-1974.

Poff, M. T., Stephen, M. F., Dean, R. G. & Mulcahy, S., 2004. Permeable Wood Groins: Case Study on their Impact on the Coastal System. *Coastal Education & Research Foundation, Inc.,* Volume 33, pp. 131-144.

Pringle, J., 2015. *ON WEATHER AND WAVES: APPLICATIONS TO COASTAL ENGINEERING,* Durban: University of KwaZulu Natal.

Reeve, D., Chadwick, A. & Fleming, C. A., 2004. *Coastal Engineering - Processes, Theory and Design Practice.* New York: Spon Press.

Ric, R. C., Holthuijsen, L. H. & Booij, L., 1994. A SPECTRAL MODEL FOR WAVES IN THE NEAR SHORE ZONE. *24th International Conference on Coastal Engineering ,* Volume 1, pp. 68-77.

Sabatier, F., 2006. *U.S. Army Corps of Engineers, Coastal Engineering Manual (CEM), Engineer Manual 1110-2-1100.* Washington, D.C.: U.S. Army Corps of Engineers.

Schooness, J. S., 2000. Annual variation in the net longshore sediment transport rate. *Coastal Engineering,* Volume 40, pp. 141-160.

Sirois, F. & Grilli, F., 2015. Potential and limits of numerical modelling for supporting the development of HTS devices. pp. 1-29.

Sumer, B. & Fredsoe, J., 1996. Scour at the head of a vertical-wall breakwater. *COASTAL ENGINEERING,* pp. 201-230.

Tarnowska, M., Zeidler, R. B., Pruszak, Z. & Basinski, 1992. *Effectiveness of Coastal Defence Measures Near-field and Far-field Factors in Overall Geometrical and Structural Factors.* 1st ed. Netherlands: Rijkswaterstaat and Delft Hydraulics.

Trampenau, T., Oumeraci, H. & Dette, H. H., 2004. HYDRAULIC FUNCTIONING OF PERMEABLE PILE GROINS. *Journal of Coastal Research,* Volume 33, pp. 160-187.

van Rijn, L., 2011. Coastal erosion and control. *Ocean and Coastal Management,* Volume 54, pp. 867-887.

Visser, R., 2002. *Morphological Modelling in the Vicinity of Groynes,* Netherlands: Delft University of Technology.

Walker, D., Dong, P. & Anastasiou, K., 1991. Sediment Transport Near Groynes in the Nearshore Zone. *Journal of Coastal Research,* 7(4), pp. 1003-1011.

Wang, C.-F., Hsu, M.-H. & Kuo, A. Y., 2004. Residence time of the Danshuei River estuary, Taiwan. *ESTUARINE COASTAL AND SHELF SCIENCE,* Volume 60, pp. 381-393.

Wenneker, I. et al., 2011. A Boussinesq-type wave driver for a morphodynamical model to predict short-term morphology. *Coastal Engineering,* Volume 58, pp. 66-84.

Young, C. K., 2010. *HANDBOOK OF COASTAL AND OCEAN ENGINEERING.* Los Angeles: World Scientific Publishing Co. Pte. Ltd..

Zanuttigh, B. et al., 2005. ENVIRONMENTAL DESIGN OF COASTAL DEFENCE IN LIDO DI DANTE, ITALY. *COASTAL ENGINEERING,* Volume 52, pp. 1089-1125.

Zhang, J., Liang, B.-c. & Li, H.-j., 2009. Numerical simulation of wave induced current with vertically varied radiation stress. *Science direct,* 22(2), pp. 254-259.

APPENDIX A
IMPERMEABLE GROYNE FIELD

Model run results

Table A-1: Results summary for Bay of Plenty

Groyne spacing = 300 m										
Model run		H_S (m)	Wave angle (Θ)	T_p Wave period (s)	Water level (m)	B_Z (m)	G_L (m)	G_S (m)	G_L/B_Z	G_S/G_L
A	1	1.4	116	9.09	0.9	93	245	300	2.634	1.224
	2			9.09	1.5	90	275	300	3.056	1.091

Table A-2: Results summary for 200 m groyne spacing

Groyne spacing = 200 m										
Model run		H_S (m)	Wave angle (Θ)	T_p Wave period (s)	Water level (m)	B_Z (m)	G_L (m)	G_S (m)	G_L/B_Z	G_S/G_L
B	1	1	120	14	1	93	250	200	2.688	0.800
	2				0	90	200	200	2.222	1.000
	3				-1	100	150	200	1.500	1.333
	4	2	120	14	1	170	250	200	1.471	0.800
	5				0	164	200	200	1.220	1.000
	6				-1	193	150	200	0.777	1.333
	7	1	135	14	1	95	250	200	2.632	0.800
	8	2	135	14	1	168	250	200	1.488	0.800
	9				0	170	200	200	1.176	1.000
	10				-1	193	150	200	0.777	1.333
	11	1	150	14	1	80	250	200	3.125	0.800
	12				0	80	200	200	2.500	1.000
	13				-1	82	150	200	1.829	1.333
	14	2	150	14	1	160	250	200	1.563	0.800
	15				0	160	200	200	1.250	1.000
	16				-1	160	150	200	0.938	1.333

Table A-3: Result summary for 250 m groyne spacing

Groyne spacing = 250 m										
Model run		H_S (m)	Wave angle (Θ)	T_p Wave period (s)	Water level (m)	B_Z (m)	G_L (m)	G_S (m)	G_L/B_Z	G_S/G_L
C	1	1	120	14	1	86	250	250	2.907	1.000
	2				0	86	200	250	2.326	1.250
	3				-1	86	150	250	1.744	1.667
	4	2	120	14	1	160	250	250	1.563	1.000
	5				0	160	200	250	1.250	1.250
	6				-1	160	150	250	0.938	1.667
	7	3	120	14	0	234	200	250	0.855	1.250
Cs*	8	3.5	120	14	1	306	250	250	0.817	1.000
	9				0	300	200	250	0.667	1.250
	10				-1	300	150	250	0.500	1.667
	11	3.5	135	14	1	300	250	250	0.833	1.000
	12				0	300	200	250	0.667	1.250
	13				-1	300	150	250	0.500	1.667
	14	3.5	150	14	1	250	250	250	1.000	1.000

	15			0	250	200	250	0.800	1.250
	16			-1	250	150	250	0.600	1.667

* Storm conditions

Table A-4: Result summary for 300 m groyne spacing

	Groyne spacing = 300 m								
	Model run	H_S (m)	Wave angle (Θ)	T_p Wave period (s)	Water level (m)	B_Z (m)	G_L (m)	G_S (m)	G_L/B_Z	G_S/G_L
D	1	1	120	14	1	90	250	300	2.778	1.200
	2				0	100	200	300	2.000	1.500
	3				-1	90	150	300	1.667	2.000
	4	2	120	14	1	150	250	300	1.667	1.200
	5				0	155	200	300	1.290	1.500
	6				-1	180	150	300	0.833	2.000
	7	3	120	14	0	250	200	300	0.800	1.500
	8	1	45	14	1	85	250	300	2.941	1.200
	9				0	90	200	300	2.222	1.500
	10				-1	90	150	300	1.667	2.000
	11	2	45	14	1	150	250	300	1.667	1.200
	12				0	150	200	300	1.333	1.500
	13				-1	160	150	300	0.938	2.000
	14	3	45	14	0	220	200	300	0.909	1.500
	15	1	150	14	1	75	250	300	3.333	1.200
	16				0	75	200	300	2.667	1.500
	17				-1	76	150	300	1.974	2.000
	18	2	150	14	1	125	250	300	2.000	1.200
	19				0	145	200	300	1.379	1.500
	20				-1	140	150	300	1.071	2.000

Table A-5: Result summary for 350 m groyne spacing

	Groyne spacing = 350 m								
	Model run	H_S (m)	Wave angle (Θ)	T_p Wave period (s)	Water level (m)	B_Z (m)	G_L (m)	G_S (m)	G_L/B_Z	G_S/G_L
E	1	1	120	14	1	82	250	350	3.049	1.400
	2				0	90	200	350	2.222	1.750
	3				-1	90	150	350	1.667	2.333
	4	2	120	14	1	150	250	350	1.667	1.400
	5				0	150	200	350	1.333	1.750
	6				-1	165	150	350	0.909	2.333
	7	3	120	14	0	220	200	350	0.909	1.750
	8	1	45	14	1	80	250	350	3.125	1.400
	9				0	85	200	350	2.353	1.750
	10				-1	84	150	350	1.786	2.333
	11	2	45	14	1	150	250	350	1.667	1.400

	12				0	150	200	350	1.333	1.750
	13				-1	160	150	350	0.938	2.333
	14	3	45	14	0	220	200	350	0.909	1.750
	15				1	70	250	350	3.571	1.400
	16	1	150	14	0	70	200	350	2.857	1.750
	17				-1	75	150	350	2.000	2.333
	18				1	150	250	350	1.667	1.400
	19	2	150	14	0	155	200	350	1.290	1.750
	20				-1	160	150	350	0.938	2.333

Table A-6: Result summary for 400 m groyne spacing

	Groyne spacing = 400 m									
Model run		H_S (m)	Wave angle (Θ)	T_p Wave period (s)	Water level (m)	B_Z (m)	G_L (m)	G_S (m)	G_L/B_Z	G_S/G_L
	1				1	83	250	400	3.012	1.600
	2	1	120	14	0	90	200	400	2.222	2.000
	3				-1	90	150	400	1.667	2.667
	4	2	120	14	1	150	250	400	1.667	1.600
	5				0	150	200	400	1.333	2.000
	6				-1	163	150	400	0.920	2.667
	7	3	120	14	0	218	200	400	0.917	2.000
	8	1	45	14	1	80	250	400	3.125	1.600
	9				0	85	200	400	2.353	2.000
F	10				-1	84	150	400	1.786	2.667
	11	2	45	14	1	150	250	400	1.667	1.600
	12				0	150	200	400	1.333	2.000
	13				-1	160	150	400	0.938	2.667
	14	3	45	14	0	220	200	400	0.909	2.000
	15	1	150	14	1	70	250	400	3.571	1.600
	16				0	70	200	400	2.857	2.000
	17				-1	75	150	400	2.000	2.667
	18	2	150	14	1	135	250	400	1.852	1.600
	19				0	141	200	400	1.418	2.000
	20				-1	143	150	400	1.049	2.667
	21	3.5	120	14	1	300	250	400	0.833	1.600
	22				0	300	200	400	0.667	2.000
	23				-1	300	150	400	0.500	2.667
	24	3.5	135	14	1	300	250	400	0.833	1.600
Fs*	25				0	300	200	400	0.667	2.000
	26				-1	300	150	400	0.500	2.667
	27	3.5	150	14	1	250	250	400	1.000	1.600
	28				0	268	200	400	0.746	2.000
	29				-1	250	150	400	0.600	2.667

Table A-7: Result summary for 450 m groyne spacing

	Groyne spacing = 450 m									
Model run		H_S (m)	Wave angle (Θ)	T_p Wave period (s)	Water level (m)	B_Z (m)	G_L (m)	G_S (m)	G_L/B_Z	G_S/G_L
	1	1	120	14	1	81	250	450	3.086	1.800
G	2				0	90	200	450	2.222	2.250
	3				-1	90	150	450	1.667	3.000

	4	2	120	14	1	150	250	450	1.667	1.800
	5				0	150	200	450	1.333	2.250
	6				-1	160	150	450	0.938	3.000

Table A-8: Result summary for 500 m groyne spacing

Groyne spacing = 500 m										
Model run		H_S (m)	Wave angle (Θ)	T_p Wave period (s)	Water level (m)	B_Z (m)	G_L (m)	G_S (m)	G_L/B_Z	G_S/G_L
H	1	1	120	14	0	90	200	500	2.222	2.500
	2				-1	82	150	500	1.829	3.333

Table A-9: Result summary for 600 m groyne spacing

Groyne spacing = 600 m										
Model run		H_S (m)	Wave angle (Θ)	T_p Wave period (s)	Water level (m)	B_Z (m)	G_L (m)	G_S (m)	G_L/B_Z	G_S/G_L
I	1	1	120	14	1	80	250	500	3.125	2.000
	2				0	80	200	500	2.500	3.000
	3				-1	85	150	500	1.765	3.333
	4	2	120	14	1	150	250	500	1.667	2.000
	5				0	150	200	500	1.333	2.500
	6				-1	165	150	500	0.909	3.333
Is*	7	3.5	120	14	1	310	250	600	0.806	2.400
	8				0	300	200	600	0.667	3.000
	9				-1	305	150	600	0.492	4.000
	10	3.5	135	14	1	304	250	600	0.822	2.400
	11				0	300	200	600	0.667	3.000
	12				-1	300	150	600	0.500	4.000
	13	3.5	150	14	1	250	250	600	1.000	2.400
	14				0	268	200	600	0.746	3.000
	15				-1	250	150	600	0.600	4.000

APPENDIX B

RESIDENCE TIME RESULTS

Residence time results

Table B-1: Residence time results for 200 m groyne spacing

H_s (m)	MWL (m)	G_L/B_Z	G_S/G_L	θ Wave angle (degrees)	Q_1 Area 1 inflow (m^3/s)	Q_2 Area 2 inflow (m^3/s)	T_{r1} Area 1 residence time (h)	T_{r2} Area 2 residence time (h)
1	0	2.500	1.000	150	9.142	7.82	2.440	2.852
	-1	1.829	1.333		15.313	14.65	0.820	0.858
1	1	2.632	0.800	135	17.171	5.70	2.028	6.106
2	1	1.488	0.800	135	41.806	21.46	0.833	1.623
1	1	2.688	0.800	120	17.233	5.90	2.021	5.907
	0	2.222	1.000		16.944	11.13	1.316	2.004
	-1	1.500	1.333		28.596	22.40	0.439	0.561
2	0	1.220	1.000	120	29.673	36.46	0.752	0.612
	-1	0.777	1.333		37.048	18.65	0.339	0.673

Table B-2: Residence time results for 250 m groyne spacing

H_s (m)	MWL (m)	G_L/B_Z	G_S/G_L	θ Wave angle (degrees)	Q_1 Area 1 inflow (m^3/s)	Q_2 Area 2 inflow (m3/s)	T_{r1} Area 1 residence time (h)	T_{r2} Area 2 residence time (h)
1	0	2.326	1.250	120	10.62	6.84	2.625	4.079
	-1	1.744	1.667		8.37	5.79	1.876	2.714
3.5	1	0.817	1.000	120	34.64	26.14	1.253	1.660
	0	0.667	1.250		21.75	15.05	1.282	1.852
	-1	0.500	1.667		8.97	7.65	1.741	2.042
3.5	1	0.833	1.000	135	37.61	28.36	1.154	1.531
	0	0.667	1.250		23.75	16.62	1.169	1.671
	-1	0.500	1.667		12.58	11.85	1.242	1.318

Table B-3: Residence time results for 300 m groyne spacing

H_s (m)	MWL (m)	G_L/B_Z	G_S/G_L	θ Wave angle (degrees)	Q_1 Area 1 inflow (m^3/s)	Q_2 Area 2 inflow (m3/s)	T_{r1} Area 1 residence time (h)	T_{r2} Area 2 residence time (h)
1	1	3.333	1.200	150	8.495	8.830	6.131	5.899
	0	2.667	1.500		6.807	6.772	4.897	4.922
	-1	1.974	2.000		7.587	5.208	2.471	3.600
2	1	2.000	1.200	150	20.221	28.314	2.576	1.839
	0	1.379	1.500		15.308	15.737	2.178	2.118
	-1	1.071	2.000		13.404	13.237	1.399	1.417
1	1	2.941	1.200	45	10.576	5.425	4.925	9.601
	0	2.222	1.500		9.934	5.960	3.356	5.593

	-1	1.667	2.000		10.085	5.686	1.859	3.297
2	1	1.667	1.200	45	28.314	20.221	1.839	2.576
	0	1.333	1.500		15.646	15.207	2.131	2.192
	-1	0.938	2.000		14.123	13.254	1.328	1.415
3	0	0.909	1.500	45	17.783	16.804	1.874	1.984
1	1	2.778	1.200	120	14.853	12.333	2.244	2.703
	0	2.000	1.500		10.381	8.967	3.211	3.717
	-1	1.667	2.000		8.330	6.570	2.251	2.854
2	1	1.667	1.200	120	11.762	25.640	4.428	2.031
	0	1.290	1.500		14.171	16.427	2.352	2.029
	-1	0.833	2.000		11.762	11.646	1.594	1.610

Table B-4: Residence time results for 350 m groyne spacing

H_s (m)	MWL (m)	G_L/B_Z	G_S/G_L	θ Wave angle (degrees)	Q_1 Area 1 inflow (m^3/s)	Q_2 Area 2 inflow (m3/s)	T_{r1} Area 1 residence time (h)	T_{r2} Area 2 residence time (h)
1	1	3.125	1.400	45	36.716	26.527	1.660	2.297
	0	2.353	1.750		12.618	8.452	3.094	4.619
	-1	1.786	2.333		10.462	8.245	2.101	2.666
2	1	1.667	1.400	45	36.716	26.527	1.655	2.291
	0	1.333	1.750		19.034	24.013	2.043	1.619
	-1	0.938	2.333		13.388	8.498	1.634	2.574
3	0	0.909	1.750	45	25.672	28.472	1.515	1.366
1	1	3.049	1.400	120	2.153	3.509	11.125	18.132
	0	2.222	1.750		12.683	12.347	3.078	3.162
	-1	1.667	2.333		9.475	9.358	2.349	2.320

Table B-5: Residence time results for 400 m groyne spacing

H_s (m)	MWL (m)	G_L/B_Z	G_S/G_L	θ Wave angle (degrees)	Q_1 Area 1 inflow (m^3/s)	Q_2 Area 2 inflow (m3/s)	T_{r1} Area 1 residence time (h)	T_{r2} Area 2 residence time (h)
3.5	1	1.000	1.600	150	36.711	55.147	1.892	1.259
	0	0.746	2.000		33.859	42.389	1.313	1.048
	-1	0.600	2.667		28.136	29.242	0.889	0.855
3.5	1	0.833	1.600	135	36.293	52.502	1.913	1.323
	0	0.667	2.000		32.826	39.701	1.354	1.119
	-1	0.500	2.667		25.103	26.449	0.996	0.945
3.5	1	0.833	1.600	120	35.184	43.333	1.263	1.026
	-1	0.500	2.667		20.124	19.678	1.242	1.270
1	0	2.222	2.000	120	14.628	17.177	3.050	2.597

Table B-6: Residence time results for 450 m groyne spacing

H_s (m)	MWL (m)	θ Wave angle (degrees)	G_L/B_Z	G_S/G_L	Q_1 Area 1 inflow (m^3/s)	Q_2 Area 2 inflow (m3/s)	T_{r1} Area 1 residence time (h)	T_{r2} Area 2 residence time (h)
1	0	120	1.333	2.250	6.89	6.56	7.287	7.646
	-1		0.938	3.000	5.31	5.15	5.321	5.488

Table B-7: Residence time results for 500 m groyne spacing

H_s (m)	MWL (m)	θ Wave angle (degrees)	G_L/B_Z	G_S/G_L	Q_1 Area 1 inflow (m^3/s)	Q_2 Area 2 inflow (m3/s)	T_{r1} Area 1 residence time (h)	T_{r2} Area 2 residence time (h)
1	0	120	2.222	2.250	15.667	15.92	3.559	3.502
	-1		1.829	3.000	11.480	14.39	2.736	2.182

Table B-8: Residence time results for 600 m groyne spacing

H_s (m)	MWL (m)	θ Wave angle (degrees)	G_L/B_Z	G_S/G_L	Q_1 Area 1 inflow (m^3/s)	Q_2 Area 2 inflow (m3/s)	T_{r1} Area 1 residence time (h)	T_{r2} Area 2 residence time (h)
1	0	135	2.500	3.000	23.57	24.69	2.839	2.710
1	0	120	2.500	3.000	20.316	22.989	3.294	2.911
3.5	1	120	0.822	2.400	80.71	102.06	1.291	1.021
	0		0.667	3.000	64.50	67.38	1.034	0.989
	-1		0.500	4.000	80.71	102.06	1.086	1.048

APPENDIX C

CURRENT SPEED VECTOR PLOT

Predicted current speed vector plot

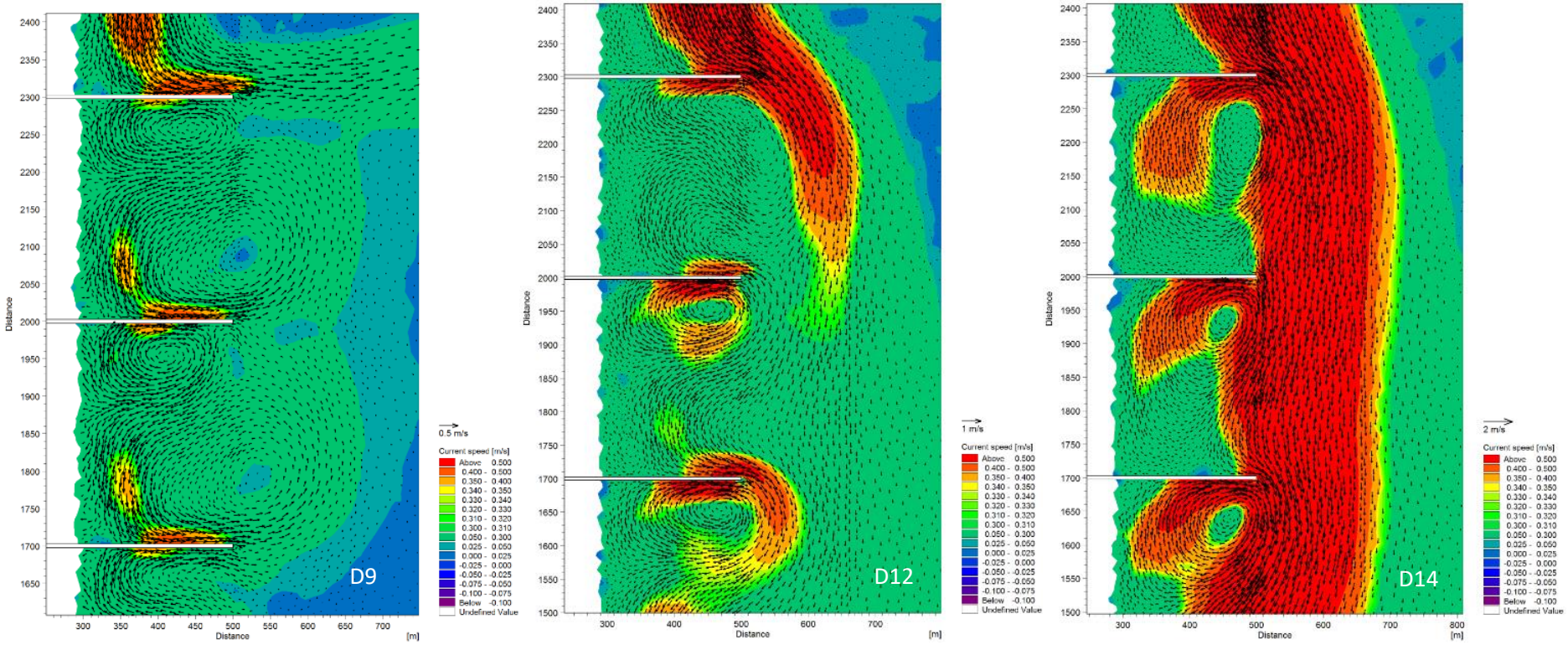

Figure C-1: Predicted current speed vector plot for (H_s = 1 m; T_p = 14 s; $\theta = 45^0$; MWL = 0) and G_S = 300 m (Model run D9)

Figure C-2: Predicted current speed vector plot for (H_s = 2 m; T_p = 14 s; $\theta = 45^0$; MWL = 0) and G_S = 300 m (Model run D12)

Figure C-3: Predicted current speed vector plot for (H_s = 3 m; T_p = 14 s; $\theta = 45^0$; MWL = 0) and G_S = 300 m (Model run D14)

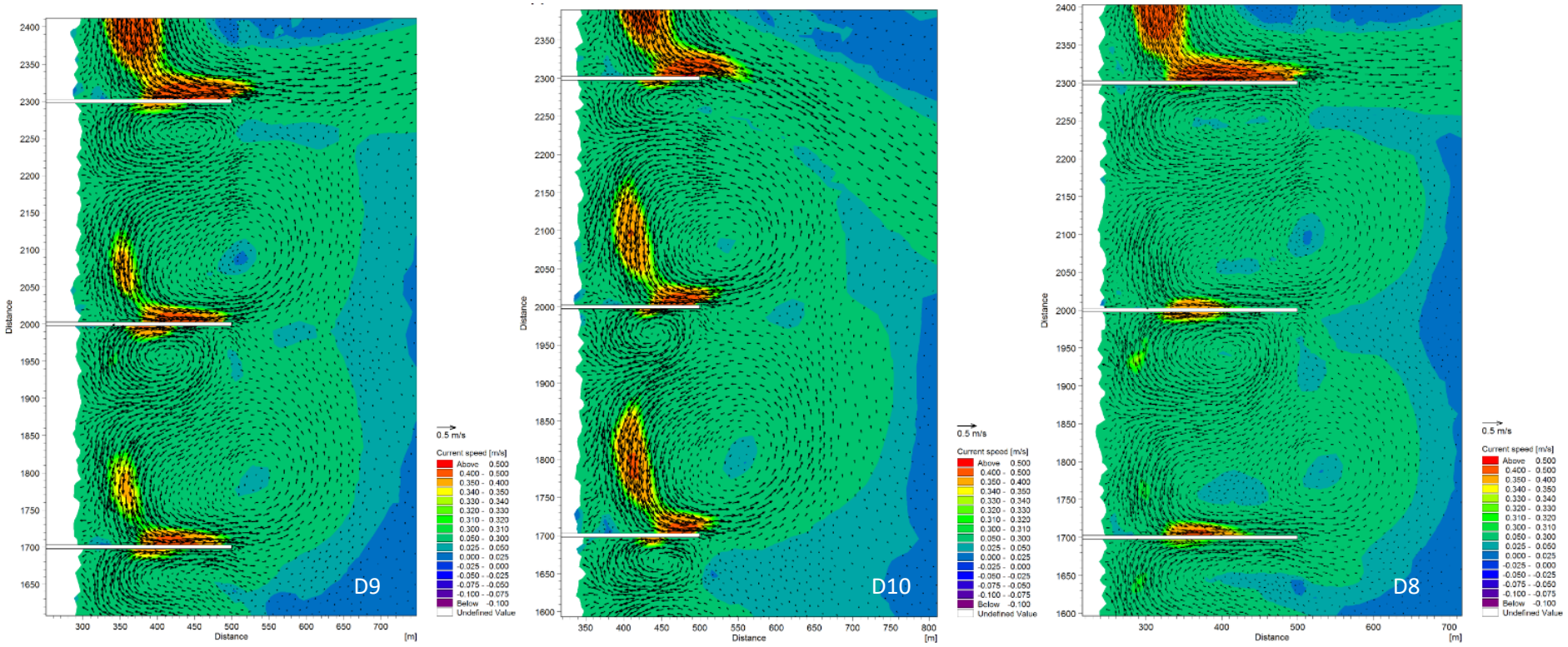

Figure C-4: Predicted current speed vector plot for (H_s = 1 m; T_p = 14 s; θ = 45^0; MWL = 0) and G_S = 300 m (Model run D9)

Figure C-5: Predicted current speed vector plot for (H_s = 1 m; T_p = 14 s; θ = 45^0; MWL = -1) and G_S = 300 m (Model run D10)

Figure C-6: Predicted current speed vector plot for (H_s = 1 m; T_p = 14 s; θ = 45^0; MWL = 1) and G_S = 300 m (Model run D8)

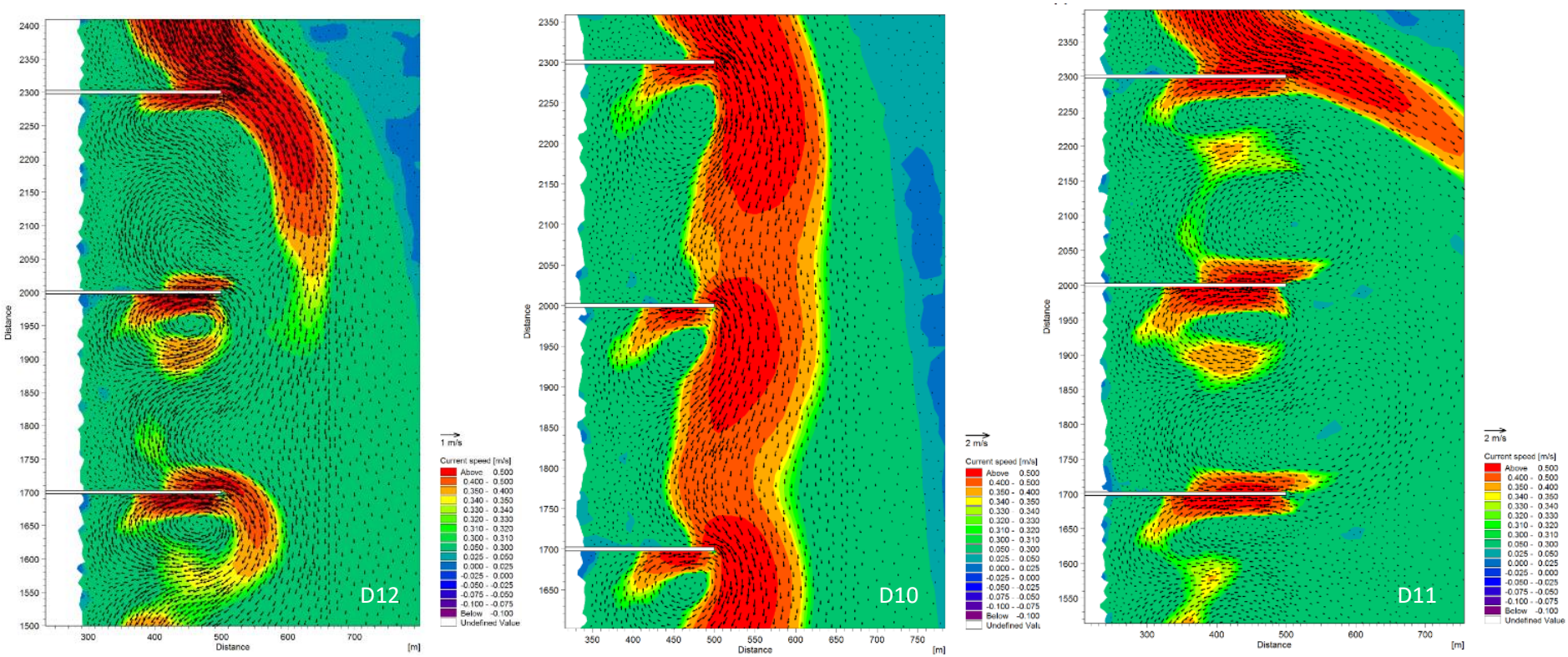

Figure C-7: Current speed vector plot for wave condition (H_s = 2 m; T_p = 14 s; $\theta = 45^0$; MWL = 0) and G_s = 300 m (Model run D12)

Figure C-8: Current speed vector plot for wave condition (H_s = 2 m; T_p = 14 s; $\theta = 45^0$; MWL = -1) and G_s = 300 m (Model run D10)

Figure C-9: Current speed vector plot for wave condition (H_s = 2 m; T_p = 14 s; $\theta = 45^0$; MWL = 1) and G_s = 300 m (Model run D11)

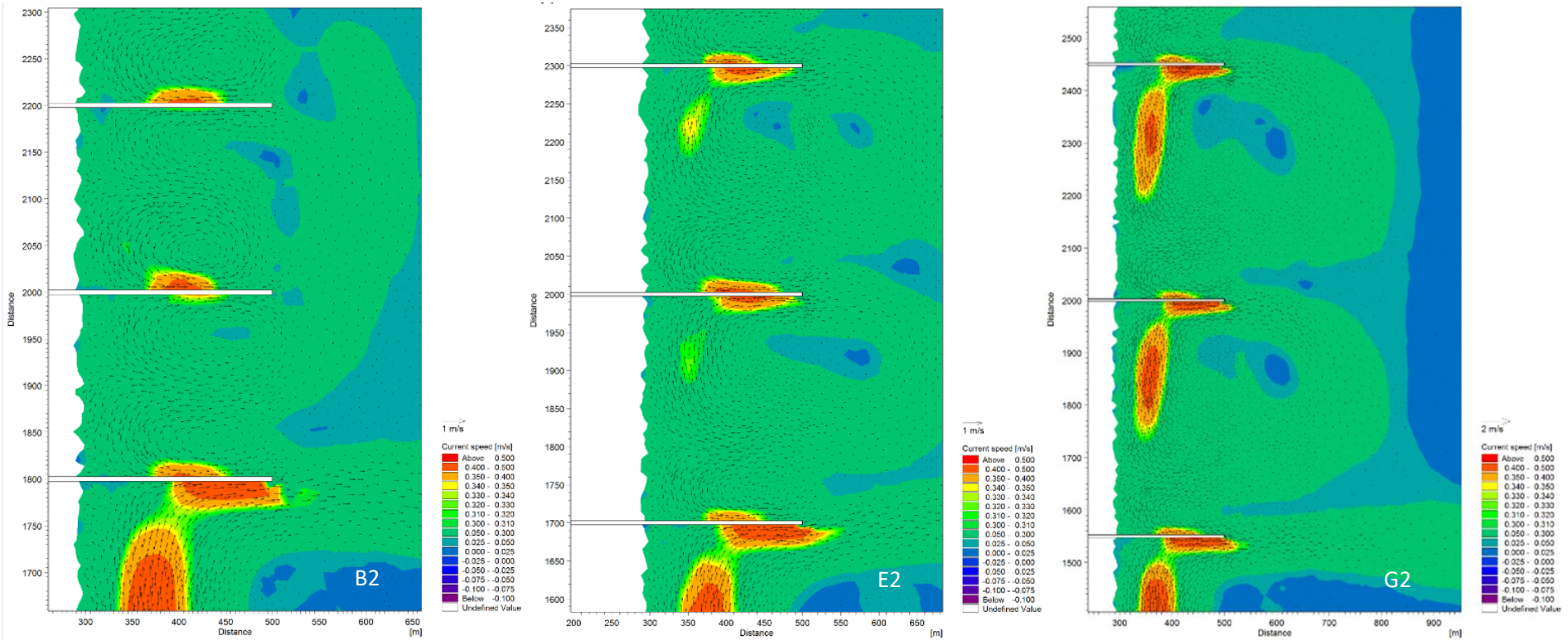

Figure C-10: Predicted current speed vector plot for wave condition (H_s = 1 m; T_p = 14 s; θ = 120^0; MWL = 0) G_S/G_L=1 (Model run B2)

Figure C-11: Predicted current speed vector plot for wave condition (H_s = 1 m; T_p = 14 s; θ = 120^0; MWL = 0) G_S/G_L=1.75 (Model run E2)

Figure C-12: Predicted current speed vector plot for wave condition (H_s = 1 m; T_p = 14 s; θ = 120^0; MWL = 0) G_S/G_L =2.25 (Model run G2)